State of Charge Estimation for Advanced Batteries: Reduced Order Electrochemical Modeling with Error Compensation

by

Kyle David Malinowski

A thesis submitted to the Graduate Faculty of
Auburn University
in partial fulfillment of the
requirements for the Degree of
Master of Science

Auburn, Alabama
December 12, 2011

Keywords: state of charge, Li-polymer, coulomb counting,
equivalent circuit model, reduced order electrochemical model

Approved by

Song-yul Choe, Chair, Associate Professor of Mechanical Engineering
Jeffrey W. Fergus, Professor of Materials Engineering
David G. Beale, Professor of Mechanical Engineering

Abstract

Advanced battery management systems are essential for efficient electrification of vehicles. Correct state of charge (SOC) estimates will maintain a battery within its charge limits and extend its usable life. Existing SOC algorithms for high-power Li-polymer batteries are not capable of accuracies greater than 95% in realistic operating conditions. This thesis proposes the use of a reduced order electrochemical model with error correction to achieve that accuracy target in the current range of 1-5C with various load profiles and ambient temperature (T_{amb}) range of 0-40°C. Hybrid electric vehicle (HEV) and electric vehicle (EV) drivers deserve to precisely know their remaining driving range and should not have to worry about premature battery pack exhaustion or failure.

Coulomb counting, equivalent circuit model, and electrochemical model approaches are evaluated based on their deviation from a standard open circuit voltage curve. The equivalent circuit is a 2^{nd} order Randle circuit and the electrochemical model is a single particle model. Order reduction was accomplished by assuming that reaction current is not influenced by the electrolyte concentration, the Butler-Volmer equation may be linearized, and ion conductivity is constant.

Two methods are proposed; one based on empirical data and one based on a closed-loop feedback system. In the first method, error rates are calculated depending on operating current rate and ambient temperature and are then applied to the reduced order electrochemical model SOC estimates during constant current and pulse loading. In the second method, model SOC estimates are updated continuously by comparing the model terminal voltage estimate to battery terminal voltage measurements with a variable gain. Performance during charge-depleting and charge-sustaining modes is investigated.

This thesis is the first to document SOC estimation performance of an equivalent circuit model and electrochemical model at ambient temperatures other than 25°C or room temperature. Also pioneered is the exploration of high current rates, charging efficiency computations as a function of temperature, and use of an open circuit voltage curve as a comparison tool rather than coulomb counting. The model error characterization and minimization techniques employed are novel as is the ROM feedback error compensation technique.

Acknowledgments

I would like to express my gratitude to my advisor, Dr. Song-yul Choe, for generously offering me this research opportunity. Under his guidance I was able to develop a strong problem solving skill set that will serve me well the rest of my life. I would also like to acknowledge committee member Dr. Jeffrey W. Fergus for providing interdisciplinary insight. Special thanks to John Marcell for always providing assistance with a smile on his face and Steven Moore for maintaining our experimental equipment.

Many thanks to my colleagues Xueyan Li, Rujian Fu, Victor Agubra, Meng Xiao, Trey Zarecor, Farzana Rahman, and Yinyin Zhao. They taught me more than any textbook or journal article ever could. Additional thanks to Xueyan Li for brainstorming with me on a daily basis. I hope to meet with them each again in the professional world.

Finally, I would like to convey my deep appreciation to my parents, David and Patricia Malinowski, for their unwavering support.

Table of Contents

List of Tables

List of Figures

List of Abbreviations

a	Activity of species (units: $mol \cdot cm^{-3}$)
a_s	Interfacial surface area (units: cm^{-1})
A	Electrode cross-sectional area (units: cm^2)
C	Reactant surface concentration (units: $mol \cdot cm^{-2}$)
C_p	Specific heat capacity (units: $J \cdot kg^{-1} \cdot K^{-1}$)
c_e	Electrolyte concentration (units: $mol \cdot cm^{-3}$); Electron concentration (units: $mol \cdot cm^{-3}$)
c_i	Ion concentration (units: $mol \cdot cm^{-3}$)
c_s	Solid phase concentration (units: $mol \cdot cm^{-3}$)
$c_{s,ave}$	Volume-averaged solid phase concentration (units: $mol \cdot cm^{-3}$)
$c_{s,max}$	Maximum solid phase concentration (units: $mol \cdot cm^{-3}$)
$c_{s,surf}$	Solid phase surface concentration (units: $mol \cdot cm^{-3}$)
d	Depth of battery (units: m)
D_e^{eff}	Effective diffusion coefficient (units: $cm^2 \cdot s^{-1}$)
D_i	Ion diffusion coefficient (units: $cm^2 \cdot s^{-1}$)
D_s	Solid phase diffusion coefficient (units: $cm^2 \cdot s^{-1}$)
e or Q_0	Elementary charge ($\pm 1.6022 \times 10^{-19}$ C)
E_{cell}	Cell potential (units: V)
$E^{\circ}_{\mathrm{cell}}$	Standard cell potential (units: V)
E_{eq}	Equilibrium potential (units: V)

E_n	Potential without current (units: V)
F	Faraday constant (96485 $C \cdot mol^{-1}$)
h	Planck constant (6.626×10^{-34} $J \cdot s$); Heat transfer coefficient (units: $W \cdot m^{-2} \cdot K^{-1}$)
i	Current density (units: $A \cdot cm^{-2}$)
I_{cutoff}	Full charge cutoff current, specified by manufacturer (units: A)
i_κ	Side reaction current (units: A)
I_n	Exchange current (units: A)
i_0	Exchange current density (units: $A \cdot cm^{-2}$)
j	Reactant flux (units: $mol \cdot cm^{-2} \cdot s^{-1}$)
j_i	Flux density (units: $mol \cdot cm^{-2} \cdot s^{-1}$)
j^{Li}	Lithium-ion current density (units: $A \cdot cm^{-3}$)
k	Reaction rate coefficient (units: s^{-1}); Thermal conductivity (units: $W \cdot m^{-1} \cdot K^{-1}$)
k_B	Boltzmann constant (1.381×10^{-23} $J \cdot K^{-1}$)
K_{eq}	Reaction quotient (dimensionless)
L^-	Thickness of negative electrode (units: cm)
n	Number of electrons transferred (dimensionless)
N_i	Ion flux density (units: $mol \cdot cm^{-2} \cdot s^{-1}$)
p	Bruggeman porosity exponent (dimensionless)
q	Heat transfer rate between the cell and its surroundings (units: $W \cdot m^{-3}$)
q_{ave}	Volume-averaged concentration flux (units: $mol \cdot cm^{-2} \cdot s^{-1}$)
Q_{charge}	Amount of charge input to battery during a full charge (units: Ah)
$Q_{discharge}$	Amount of charge output from battery during a full discharge (units: Ah)
Q_{gen}	Heat generation rate per unit volume (units: $W \cdot m^{-3}$)

Q_{max}	Maximum charge capacity of a battery (units: Ah)
Q_{rated}	Rated charge capacity of a battery as defined by manufacturer (units: Ah)
$Q_{releasable}$	Amount of charge remaining in a battery that may be discharged until V_{min} is reached (units: Ah)
r	Radius of electrode particle (units: cm)
R_s	Maximum radius of electrode particle (units: cm)
S_0	Stoichiometry values at 0% SOC (dimensionless)
S_{100}	Stoichiometry values at 100% SOC (dimensionless)
SOC_{CC}	SOC estimate from coulomb counting (units: %)
SOC_{ROM}	SOC estimate from the ROM (units: %)
SOC_{OCV}	SOC estimate from OCV curve (units: %)
t_+^0	Li^+ transference number (dimensionless)
T_{amb}	Ambient temperature (units: °C)
t_i	Transference number (dimensionless)
t_{total}	Total time of a full discharge at a specified current and ambient temperature (units: s)
U	Equilibrium potential (units: V)
u_i	Ion mobility (units: $cm^2 \cdot s^{-1} \cdot V^{-1}$)
v	Stoichiometric coefficient (dimensionless)
V	Bulk fluid velocity (units: $cm \cdot s^{-1}$)
v_e	Electron velocity (units: $cm \cdot s^{-1}$)
V_{max}	Maximum terminal voltage of battery, specified by manufacturer (units: V)
V_{min}	Minimum terminal voltage of battery, specified by manufacturer (units: V)
V_T	Terminal voltage (units: V)

z_e	Electron count (dimensionless)
z_i	Ion charge number (dimensionless)
α	Transfer coefficient (dimensionless)
α_a	Anodic transfer coefficient (dimensionless)
α_c	Cathodic transfer coefficient (dimensionless)
δ	Electrode width (units: cm); SEI film thickness (units: cm)
ε	Permittivity (units: F·cm^{-1})
ε_e	Electrolyte phase volume fraction (dimensionless); Active material volume fraction (dimensionless); Porosity (dimensionless)
ε_f	Conductive filler volume fraction (dimensionless)
ε_p	Polymer phase volume fraction (dimensionless)
η	Total overpotential (units: V); Efficiency coefficient (dimensionless)
η_{act}	Activation overpotential (units: V)
η_{conc}	Concentration overpotential (units: V)
η_{ohm}	Ohmic overpotential (units: V)
κ^{eff}	Effective ionic conductivity (units: S·cm^{-1})
ρ	*R*esistivity (units: Ω·cm); Density (units: kg·m^{-3})
σ	*C*onductivity (units: S·cm^{-1})
σ^2	SOC estimation variance (units: %^{2})
σ^2_{ave}	Average SOC estimation variance (units: %^{2})
σ^{eff}	Effective solid conductivity (units: S·cm^{-1})
σ_{cc}	Coulomb counting SOC estimation error (units: %)
σ_{ECM}	ECM SOC estimation error (units: %)

σ_{ROM}	ROM SOC estimation error (units: %)
$\dot{\sigma}_{ROM}$	Coulomb counting SOC estimation error rate (units: %/hr)
ϕ_{e}	Electrolyte potential (units: V)
ϕ_{s}	Solid phase potential (units: V)
ϕ_{se}	Phase potential difference (units: V)

Chapter 1: Introduction

The electrification of automobiles is becoming a popular field of study as consumer demand increases for vehicle efficiency and manufacturers face strict emission and fuel economy requirements. Batteries provide safe, durable, and efficient electrical energy storage, some types more than others. Lithium-ion polymer cells have highest energy density of any battery on the market today, provide the greatest electrochemical potential, are relatively light in weight, require no maintenance, exhibit negligible hysteresis, have long cycle lives, demonstrate little self-discharge, and are environmentally safe to dispose. All these factors make them desirable to OEMs and explain their relatively recent implementation in hybrid electric vehicles (HEV) and electric vehicles (EV). This thesis will focus on a fundamental issue common to all high-power batteries.

1.1 Problem Statement

Accurately predicting the remaining driving range in a hybrid electric or full electric vehicle is essential. As HEVs/EVs grow in popularity and complexity, new monitoring methods are needed to better track performance. Drivers need to know how much further they can travel before their vehicle batteries require a recharge. The state of charge (SOC) of a battery or pack of batteries is analogous to a fuel gauge in an internal combustion vehicle. The remaining charge calculation must be correct in order to utilize a battery's full capability. This must be accomplished within charge limitations of the battery so as to not cause unwanted degradation in the form of permanent charge capacity loss. Precision of SOC evaluation is instrumental in alleviating EV range anxiety. Most OEMs have a SOC estimation error target of ≤ 5 % under all realistic driving conditions, yet no existing estimation techniques are capable of this. The objective of this research is to devise a new method to meet the target of ≥ 95% accuracy in the current range of 1-5C with various load profiles and T_{amb} range of 0-40°C. The selected investigation range covers the vast majority of realistic HEV/EV battery pack operating conditions.

1.2 Definition of SOC

SOC is defined as ratio of the charge capacity in a cell ($Q_{releasable}$) to the maximum charge capacity at full charge (Q_{max}). The preferred SOC reference should be Q_{max} rather than the rated charge capacity of a new cell (Q_{rated}) because Q_{max} decreases as the cell ages. With this approach, the SOC range will always be 0-100%. The equation for SOC may be generalized as

$$SOC = \frac{Q_{releasable}}{Q_{\max}} \times 100\%$$

where Q has units of ampere-hours (Ah). Units of charge capacity in high-power batteries are typically Ah. $Q_{releasable}$ and Q_{max} are a measure of electrons flowing from a battery, therefore it does not represent battery internal dynamics. The standard T_{amb} and C-rate that these variables are evaluated at is 25°C and 1C, respectively.

A more precise definition considers the components that contribute to charge capacity, which are the lithium-ions inside a battery. SOC is an average of the ratio of the concentration of lithium-ions in the negative electrode to the maximum concentration in the negative electrode, exemplified by

$$SOC = \frac{1}{\delta^{-}} \int_{0}^{\delta^{-}} \frac{\left(c_{s,ave} - c_{s,\max} \cdot S_0\right)}{c_{s,\max} \cdot (S_{100} - S_0)} dx$$

where δ is the width of the negative electrode (cm), $c_{s,ave}$ is the volume-averaged solid phase concentration (mol·cm^{-3}), $c_{s,max}$ is the maximum solid phase concentration (mol·cm^{-3}), and S_0 and S_{100} are the lithium stoichiometry values at 0% and 100% SOC, respectively. This definition accounts for physical electrode limitations; therefore, it will be adopted as the formal SOC definition.

Chapter 2: Battery Fundamentals

Batteries are electrochemical energy storage devices. They are categorized into two groups, primary and secondary. Primary batteries are those that may only be discharged once and do not possess the ability to be charged. Charge is permanently depleted during use, such as with most small portable electronics. Secondary batteries are those that may be discharged and charged multiple times. Charge may be replenished, such as with most batteries found in laptops and automobiles. A power conversion cycle exists whereby chemical potential is converted to electric power during discharge and electric power is converted back to chemical potential during charge.

A few key electrochemical terms are integral for complete understanding of a battery. The terms battery and cell are used interchangeably. The amount of energy stored in a battery is known as charge (Q). It is defined as the quantity of electricity and has units of coulombs (C). Charge can be positive or negative depending on whether the matter exhibits attraction or repulsion in the presence of other matter. The elementary charge (e or Q_0) is defined to be the electric charge carried by a single proton or electron and is equal to $\pm 1.6022\times 10^{-19}$ C; positive for a proton and negative for an electron. Within matter, there exist two types of charge, fixed and mobile. Mobile charges consist of ions and electrons found in conductors while fixed charges are those found in insulative matter. Mobile charge material is the foundation for battery internal construction. Examples of electronic conductors include copper and carbon, and an example of an ionic conductor is battery electrolyte.

Batteries are manufactured with multiple layers of electrodes, each consisting of a combination of electronic and ionic conductors. Desired performance may be enhanced by altering the electrode chemistry, which determines the amount of lithium-ions initially intercalated, or bound between the electrode compounds. Ions are conserved during operation, meaning that the amount is the same whether it has been cycled zero times or one thousand.

Lithium-ion (Li^+) polymer intercalation-type batteries are made of many layers of microcells. A typical microcell diagram is shown in Figure 1.

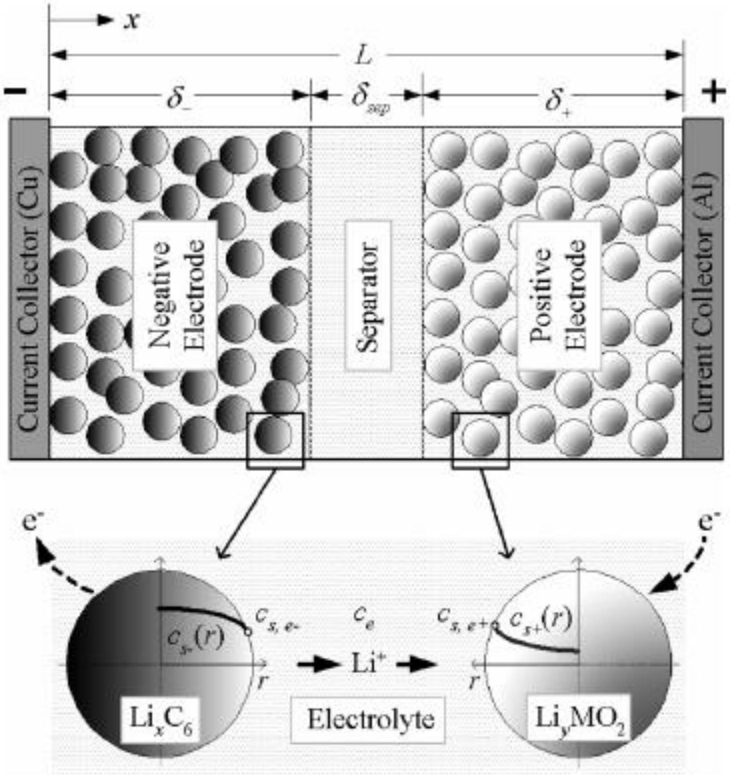

Figure 1: Microcell diagram [47]

The term intercalation-type implies that the electrodes have a lattice structure. Charging/discharging the cell causes the Li-ions to leave the positive/negative electrode and enter the lattice structure of the negative/positive electrode, respectively. Discharge kinetics are shown in Figure 2.

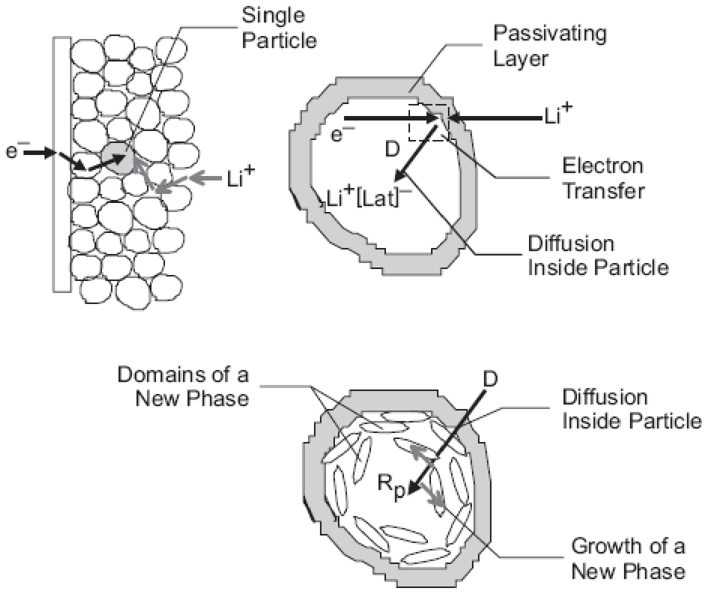

Figure 2: Discharge kinetics [61]

This process of ions being moved in and out of an interstitial site in the lattice is called intercalation. Li-polymer batteries evolved from lithium-ion batteries with the difference being that the electrolyte is held in a solid polymer composite rather than an organic solvent [71]. The electrolyte consists of lithium salts such as $LiPF_6$, $LiBF_4$, or $LiClO_4$ [33],[36],[59]. One microcell has five components including a negative current collector, negative electrode, separator with infused electrolyte, positive electrode, and positive current collector. Both electrodes are also infused with electrolyte. A binder material, such as polyvinylidene fluoride (PVDF), appends the separator to the electrode. The typical main ingredient of a negative electrode is carbon while the typical for the positive electrode is a metal oxide consisting of manganese, nickel, and cobalt. The voltage of a lithium-ion polymer cells typically varies from 2.5 to 4.2 V.

The microcell layer order is crucial to battery operation. During discharge, Li^+ ions diffuse to the surface of carbon particles in the negative electrode where they deintercalate and transfer to an electrolyte solution. The positively charged ions travel via diffusion and migration through the electrolyte solution, where they again react and diffuse into metal oxide active material particles [8],[33],[36],[39],[40],[41],[47],[54],[55],[59],[68],[80],[90]. Electrons, produced in the negative electrode reaction and consumed in the positive electrode reaction, are blocked by the electronically insulating separator and instead must travel through an external circuit. During discharge, these electrons provide power to an external load. A battery is considered fully charged/discharged when the Li-ion concentration in the negative electrode reaches a maximum/minimum, respectively. The manufacturer determines these limits so as not to damage a battery.

Ions migrate through channels in the separator material between the electrodes. These active molecules attract Li^+ ions. Driven by the electromotive force, the Li^+ ions bond with active molecules in succession until they reach the opposite electrode. Also, the concentration gradient will drive Li^+ ions to disperse evenly in the electrolyte when there is no load on the battery. Transport modes will be discussed in detail later on.

Ion and electron transport may be inhibited by temperature or resistive layer growth. High temperature may cause the electrolytic polymer to decompose resulting in active material becoming inactive. Low temperature may cause the Li^+ ions to plate out in solid metal form. This results in a loss of Li^+ ions which decreases the electrolyte conductivity since it is a function of Li^+ ion concentration. The resistive layer between the anode particles and surrounding electrolyte is known as the solid electrolyte interface (SEI), formed initially by the decomposition of organic solvents in the electrolyte upon primary charging. It is deliberately formed by the manufacturer in order to provide a barrier that restricts reactions between the carbon anode and the electrolyte. Figure 3 shows the SEI layer structure.

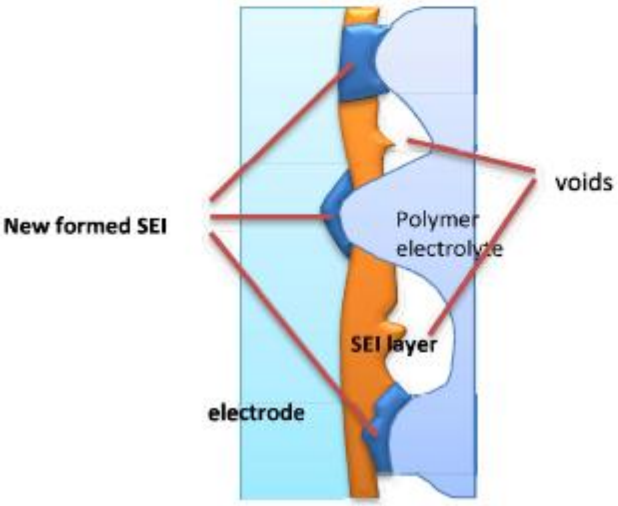

Figure 3: SEI layer structure [24]

During the first activation cycles, a part of Li^+ ions will remain in the negative electrode and another part will be consumed in the SEI, which is an irreversible process [54]. This layer grows with cycling as organic solvents and Li^+ ions continue to plate the anode surface [58]. Significantly more cathode material than anode material, electrode overlap and subsequent shorting during manufacturing, and local non-uniformities in polarization augment the probability of Li metal plating. In addition, transition metals from the cathode may dissolve and become part of the SEI [60]. The growth of the SEI is related to the rate of the side reactions by

$$\frac{\partial \delta}{\partial t} = \frac{i_\kappa M}{L \alpha \rho F}$$

where δ is the film thickness (cm) composed of lithium products and i_κ is the rate of the side reaction (A). The other parameters are all constants for a given reaction and a given battery chemistry [55],[56].

Many researchers consider SEI growth to be the major source of battery aging. Other contributors may be seen in Figure 4, with high and low temperatures being detrimental for different reasons.

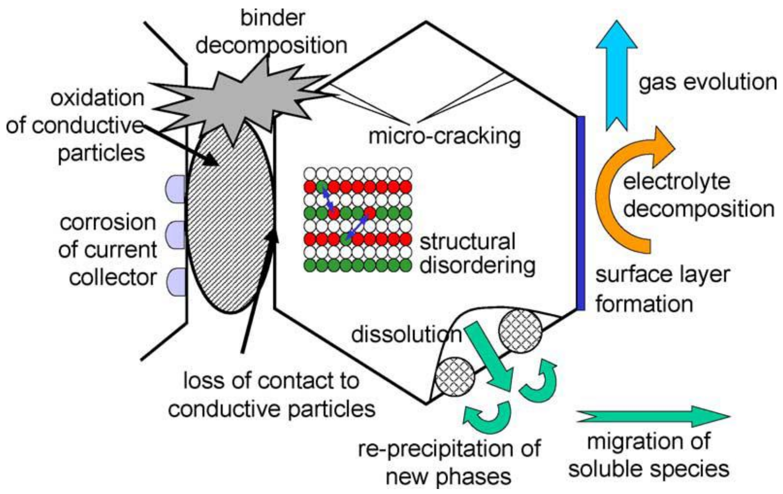

Figure 4: Sources of battery aging [60]

The fundamentals of electrochemistry will now be discussed. Current (I) is defined as the rate of flow of electric charge. It is the measure of flow of coulombs per second, with units of amperes (A). Current flows in the opposite direction of electron flow. When considering current to or from a battery, the current direction during discharge is defined as positive. It may be written mathematically as a function of the Faraday constant F (96485 C·mol^{-1}), the cross-sectional area A (cm^2), the electron velocity v_e (cm·s^{-1}), and the electron concentration c_e (mol·cm^{-3}) in the form of

$$I = \frac{dQ}{dt} = -FAv_e c_e$$

where F, defined as the magnitude of electric charge per mole of electrons, equals Avogadro's number N_{Av}, times the elementary charge Q_0, is calculated to be

$$F = N_{Av} Q_0 = (6.0221 \times 10^{23} mol^{-1})(1.6022 \times 10^{-19} C) = 96485 C \cdot mol^{-1}$$

Current density (i) is the measure of the density of flow of charge. It is defined as the current per unit area with units of amperes per square centimeter (A·cm^{-2}), and calculated as

$$i = \frac{I}{A}$$

Current, however, is defined with different variable values for electrons and ions. For electrons,

$$I = z_e F A v_e c_e$$

where z_e is the number of electrons.

For ions,

$$I = FA\sum_i z_i v_i c_i$$

where z_i is the charge number of the ion.

Flux density, j_i, is defined as the moles per area per second ($\mathrm{mol \cdot cm^{-2} \cdot s^{-1}}$) and calculated as

$$j_i = v_i c_i$$

$$\therefore i = F\sum_i z_i j_i$$

Electric potential (ϕ) is defined as the electric potential energy divided by the charge. It is a scalar quantity measured in volts (V) or joules per coulomb (J/C). Within a battery, voltage is equal to the difference in electrical potential between two materials. There will be zero voltage between identical electrodes since they share the same potential. Lithium has different potentials when placed in an interstitial lattice site of the solid active materials of the anode or cathode [15].

Standard potential is calculated as the difference between the potential of a material and that of a standard hydrogen electrode. Hydrogen gas at one bar pressure and 25°C is bubbled over an inert platinum electrode in an aqueous solution of 1M concentration of $H^+(aq)$. The standard cell potential ($E°_\mathrm{cell}$) is the difference between the cathode and anode potentials at standard conditions, measured in volts. There is a tendency for reduction to occur at one of the electrodes. $E°_\mathrm{cell}$ may be positive or negative depending on the reduction half-reaction. Tables have been created that document the standard electrode potentials of many known solutions. Li^+ ions have one of the greatest negative standard electrode potentials, -3.04 V.

Electrical conductivity (σ or κ) is the measure of a material's ability to conduct current. It is defined as the ratio of current density (j_i) to the magnitude of the electric field (E). It is the inverse of resistivity and has the units of siemens per centimeter ($S \cdot cm^{-1}$), with one Siemen equal to one ampere per volt. Materials with higher electron conductivity, such as copper, allow for easier current flow while electron insulating materials, such as water, are much more resistive to flow. Different materials have different charge carriers which might include electrons or specified anions or cations.

Electrical resistivity (ρ) is the measure of a material's ability to oppose electric current. According to Ohm's law, it is defined as the ratio of voltage to the current and has units of ohm-centimeters ($\Omega \cdot cm$). Ohmic resistance is due to the current flow through the various metallic components while ionic resistance is due to voltage drop resulting from the flow of ions across the separator [19]. Capacitance (C) is the ability of a body to hold an electrical charge. It is defined as the ratio of charge to the voltage and has the units of farads (F). Charge can be written as

$$Q = -C\Delta E_{source} = -\left(\frac{\varepsilon A}{L}\right)\Delta E$$

where C is capacitance, ε is permittivity ($F \cdot cm^{-1}$), and E is the potential.

There are three modes of ion transport within most batteries, which includes migration, diffusion, and convection. Convection does not occur in lithium-ion polymer batteries due to their solid electrolyte. Migration is potential-driven. It is directly related to the solid phase surface concentration gradient [58]. An electric field across a solution creates a driving force. Double layer capacity is a buildup of charge just outside of the two electrodes due to polarized molecules attracted to either electrode. This charge separation creates a voltage drop that drives lithium-ion transfer [19]. It follows the equation

$$N_{i,migration} = -z_i u_i F c_i \nabla \phi$$

where u_i is the ion mobility (cm^2·s^{-1}·V^{-1}) and c_i is ion concentration (mol·cm^{-3}). In each of the three ion transport equations, N_i is the flux density (mol·cm^{-2}·s^{-1}).

Diffusion is concentration-driven. Ions diffuse from a higher concentration to a lower concentration. It follows the equation

$$N_{i,diffusion} = -D_i \nabla c_i$$

where D_i is the ion diffusion coefficient (cm^2·s^{-1}).

Convection is velocity-driven. Ions are carried along with the bulk movement of a fluid. This does not affect lithium-ion polymer batteries since the electrolyte is solid. It follows the equation

$$N_{i,convection} = -c_i V$$

where V is the bulk fluid velocity (cm·s^{-1}).

Since batteries are electrochemical devices, both electrical and chemical terminology must be understood. Current requires the transfer of electrons or ions. Chemical reactions known as oxidation and reduction make this possible. Oxidation occurs when a material releases electrons, thereby releasing cations or accepting anions, while reduction is the acceptance of electrons, thereby reducing the number of cations or increasing the number of anions. In any oxidation-reduction (redox) reaction, there are two half-reactions. One species undergoes oxidation and another undergoes reduction. Basically, electrons are transfers from one to the other.

A standard change in Gibbs free energy, ΔG°, is proportional to the standard potential, E°, as

$$\Delta G^\circ = -nFE^\circ$$

Using the Gibbs function,

$$\Delta G = \Delta H - T\Delta S$$

the free energy change for the reaction can be calculated where the change in entropy of a battery is calculated as

$$\Delta S = nF\frac{\partial E}{\partial T}$$

where n is the number of electrons transferred in the reaction, F is the Faraday constant, and E is the cell potential.

Redox chemical equations must be balanced with respect to mass and charge. In an oxidation half-reaction equation, a number of neutral-charged molecules will be split into a number of ions plus a number of electrons. Likewise, in a reduction half-reaction equation, a number of ions and a number of electrons combine to form a number of neutral-charged molecules. The same number of electrons should appear in each half-reaction equation, in order to follow conservation of charge laws.

The two half-reaction equations may be combined to obtain an overall reaction equation. Typical cathode materials used in lithium-ion polymer batteries are manganese, nickel, and cobalt. The following chemical equations show the discharge reactions with a manganese-based cathode [55]

$$Li_{1-x}MnO_2 + xLi^+ + xe^- \rightarrow LiMnO_2 \qquad \text{(Reduction in cathode)}$$

$$C_6Li_x \rightarrow xLi^+ + xe^- + 6C \qquad \text{(Oxidation in anode)}$$

$$Li_{1-x}MnO_2 + C_6Li_x \rightarrow LiMnO_2 + 6C \qquad \text{(Net balanced equation)}$$

A half-cell consists of an electrode immersed in a solution of ions. Two of these joined by a salt bridge form a voltaic (galvanic) cell. The salt bridge allows for ion transport and inhibits any electron flow. It is needed however for electron flow through the outer loop from electrode to electrode. The electrons may only travel between electrodes through an external load while the ions may only travel from half-cell solution to the other. The electrode at which oxidation occurs is referred to as the anode and the electrode at which reduction occurs is referred to as the cathode. The cell potential (E_{cell}) is the driving force that moves electrons from the anode to the cathode. The electrons flow in this direction during discharging of a battery. When electrons move in the opposite direction it is called charging. A simplified voltaic cell diagram may be written with the anode half-cell reaction on the left, the cathode half-cell reaction on the right, and a double vertical line in between indicating the salt bridge. It would look like

$$Li(s) \mid Li^{+}(aq) \parallel Mn^{2+}(aq) \mid Mn(s)$$

As mentioned before, standard electrode potentials ($E°$) are derived in comparison to a hydrogen electrode under standard conditions. E_{cell} is equal to the electric potential of the cathode minus the electric potential of the anode. If this is a positive value, then the reaction from the left side of the voltaic cell representation shown above is considered to be spontaneous (galvanic cell). If negative, it is non-spontaneous (electrolyte cell). The system is considered to be at equilibrium when E_{cell} is equal to zero, which means that the battery is dead. Electricity may only be produced when the cell reaction is not at equilibrium.

The reaction quotient (K_{eq}) is a function of the concentrations of chemical species involved in the chemical reaction. Standard Gibbs free energy change and standard cell potential may be written as

$$\Delta G^{\circ} = -RT \ln K_{eq} \text{ and } E^{\circ}_{cell} = \frac{RT}{nF} \ln K_{eq}$$

The Nernst equation relates the nonstandard cell potential to the standard cell potential. The concentrations of species in a cell change with current and will continue to change until equilibrium is reached. The concentration of species may be determined by measuring the nonstandard cell potential by using

$$E_{cell} = E^{\circ}_{cell} + 2.303 \frac{RT}{nF} \log_{10}(a)$$

where a is the activity of species (mol·cm^{-3}), related to K_{eq} by

$$K_{eq} = \frac{\prod_{j} a_{j\{t\}}^{v_j}}{\prod_{i} a_{i\{t\}}^{v_{ij}}}$$

in which the subscript j refers to reactants, the subscript i refers to products, and v is the stoichiometric coefficient.

A battery stores electrical energy until connected to a load when it releases that energy. The anode experiences oxidation while the cathode experiences reduction. During this process, the change in Gibbs free energy is negative, which means that the battery has less free energy after releasing the energy than it did at the beginning.

Overpotentials are a source of voltage drop and power loss. There are three types including ohmic, activation, and concentration. They increase with current and temperature [45]. They may be added together to calculate the total overpotential (η) as a function of applied current. This represents the change in potential that a charged species would go through as it passes through the spherical particle into the electrolyte [15]. At each electrode,

$$\eta = \phi_s - \phi_e - U$$

where ϕ_s is the solid phase potential, ϕ_e is the electrolyte potential, and U is the equilibrium potential.

Ohmic overpotential (η_{ohm}) also known as resistance polarization, is equal to the difference in potential across a length of solution. It is linked to the finite conductivity of the non-electroactive cell constituents. It is a function of current and resistance, considered as a voltage drop, and may be calculated as [55]

$$\eta_{ohm} = \phi(0) - \phi(L) = -\int_0^L d\phi = \int_0^L \frac{i \cdot dx}{\kappa} = \frac{I}{\kappa}\int_0^L \frac{dx}{A} = \frac{IL}{\kappa A} = IR$$

Electrical work (W_{el}) can be calculated in numerous ways including

$$W_{el} = QE = nFE = -\Delta G$$

$$\therefore E = \frac{-\Delta G}{nF} = \frac{-(\Delta H - T\Delta S)}{nF}$$

where Q is charge, E is potential, n is the number of electrons, and F is the Faraday constant.

Current density, from Faraday's law, is

$$i = nFj = nF(j_{ox} - j_{rd}) = nF(k_{ox}C_{ox} - k_{rd}C_{rd})$$

where $k = \frac{k_B T}{h}\exp\left(\frac{-\Delta G}{RT}\right)$,

j is the reactant flux ($\mathrm{mol \cdot cm^{-2} \cdot s^{-1}}$), k is the reaction rate coefficient ($\mathrm{s^{-1}}$) as a function of Gibbs free energy, C is the reactant surface concentration ($\mathrm{mol \cdot cm^{-2}}$), k_B is the Boltzmann constant (1.381×10^{-23} $\mathrm{J \cdot K^{-1}}$), and h is the Planck constant (6.626×10^{-34} $\mathrm{J \cdot s}$).

The change in Gibbs free energy may also be written as a function of chemical and electrical terms. In general,

$$\Delta G = \Delta G_{activation} + \alpha FE$$

where α is the transfer coefficient, defined as the number of electrons transferred during multistep reactions.

The reaction rate coefficients for reduction and oxidation may now be written in terms of α and ΔG as

$$k_{rd} = k_{0,rd} \cdot \exp\left(\frac{-\alpha_{rd} FE}{RT}\right)$$

$$k_{ox} = k_{0,ox} \cdot \exp\left(\frac{-\alpha_{ox} FE}{RT}\right)$$

where $k_0 = \frac{k_B T}{h} \cdot \exp\left(\frac{-\Delta G_{activation}}{RT}\right)$.

If the reaction rate coefficients are then plugged back into the current density equations, the net current density becomes

$$i = nF\left\{k_{0,ox} \cdot \exp\left(\frac{-\alpha_{ox} FE}{RT}\right) C_{ox} - k_{0,rd} \cdot \exp\left(\frac{-\alpha_{rd} FE}{RT}\right) C_{rd}\right\}$$

Exchange current density (i_0) is a measure of how active an electrode surface is. The higher it is, the easier it is for charge to flow. When the net current density is equal to zero the system is said to be in equilibrium, the term is then called exchange current density, calculated as

$$i_0 = nFk_{0,ox} \cdot \exp\left(\frac{-\alpha_{ox} FE_{eq}}{RT}\right) C_{ox} = nFk_{0,rd} \cdot \exp\left(\frac{-\alpha_{rd} FE_{eq}}{RT}\right) C_{rd}$$

where E_{eq} is the equilibrium potential.

The Butler-Volmer equation goes a step further in the net current density equation by replacing nFk_0C with i_0, so

$$i = i_0 \left\{ \exp\left(\frac{-\alpha_{ox} F\left(E - E_{eq}\right)}{RT} \right) - \exp\left(\frac{-\alpha_{rd} F\left(E - E_{eq}\right)}{RT} \right) \right\}$$

Activation overpotential refers to the potential needed to overcome the large initial potential step in a multistep reaction. It is linked to the thermodynamic irreversibility of some chemical processes. Using the Butler-Volmer and Nernst equations, the activation overpotential (η_{act}) can be derived in [55]

$$I = I_n \cdot \exp\left\{ \frac{(1-\alpha)F}{RT} \eta_{act} \right\} - I_n \cdot \exp\left\{ \frac{-\alpha F}{RT} \eta_{act} \right\} = I_{ox} + I_{rd}$$

where I_n is the exchange current. The equation presented matches that mentioned at the beginning.

Concentration overpotential refers to conditions of limits of diffusion. It is linked to the transient non-homogeneity in the spatial repartition of the electroactive species. If lithium-ion concentrations at an electrode surface are too high or too low, the mass transport of the species can affect the cell potential. When the electrode is represented as a collection of spheres, the ratio of Li^+ surface concentration over the maximum concentration represents the amount of readily available power. This is because the surface lithium is easily removed, whereas the ions near the center of the particle are limited by the rate of diffusion to reach the surface [22],[23],[33],[39]. Based on Nernst's law, the concentration overpotential (η_{conc}) can be calculated as [55]

$$\eta_{conc} = E - E_n = \frac{RT}{nF} \ln \frac{c_R^b c_O^s}{c_R^s c_O^b}$$

where E_n is the potential when no current is applied, R and O represent reduction and oxidation species, and s and b represent surface and bulk, respectively.

There are documented examples of hysteresis occurring in Li-ion batteries observed during the intercalation of lithium-ions into carbon. It is believed that the lithium atoms may bond to hydrogen-terminated edges of hexagonal carbon. The capacity for the insertion of lithium is strongly dependent on the hydrogen content of the carbon materials. If the inserted lithium bonds to a carbon atom, which also is bonded with a hydrogen atom, a corresponding change to the carbon-carbon bond from $(sp)^2$ to $(sp)^3$ may occur, contributing to a large hysteresis during lithium insertion [54]. Another possible cause for hysteresis is phase transitions in the positive electrode.

There are multiple sources of heat generation within a cell. These include Joule heating, exothermic/endothermic chemical reactions, heat of mixing, and overpotentials. Joule heating is created by the flow of electrons in the current collectors, and to a much smaller extent the flow of electrons in the electrode and flow of ions in the electrolyte, and is proportional to the square of the current. Chemical reactions which occur during intercalation and deintercalation either expel or absorb heat as new molecules are formed, proportional to charge. Heat of mixing is caused by ion flow in the electrode and is proportional to the gradient of ion concentration. Overpotential, specifically activation overpotential, causes heat generation at the interface between electrode and electrolyte. Irreversible thermodynamic processes create entropy, observed as heat, proportional to the current. As cell temperature decreases, slow kinetics require an increase in overpotentials to drive reactions. Slow diffusion results in increased solid and electrolyte phase concentration gradients and also results in decreased ionic conductivity of the electrolyte, which leads to larger electrolyte phase potential gradients [58].

There are three main types of lithium-ion polymer batteries, which are pouch, cylindrical, and prismatic. Pouch-type cells consist of multilayer microcells stacked atop one another in a rectangular shape with a soft outer shell. Cylindrical-type cells consist of one long microcell wrapped tightly into a cylinder shape with a hard shell. Prismatic-type cells are similar to cylindrical-type only they are pressed into a cubical shape. An example of a pouch-type cell with a cobalt-based cathode is shown in Figure 5.

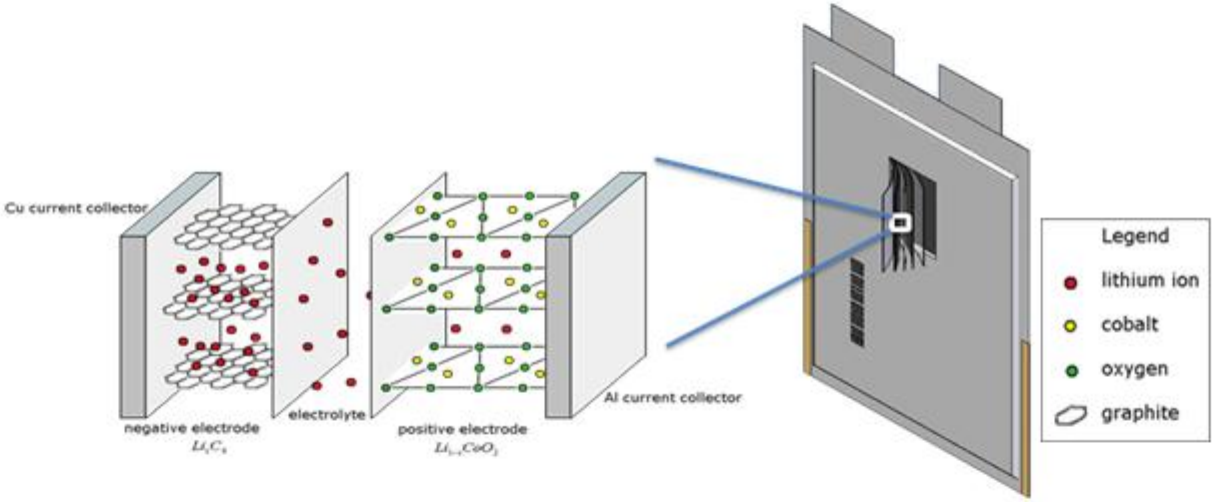

Figure 5: Pouch type Co-based cathode microcell [24]

Applications, causes of degradation, and quick charging techniques are key focuses of research presently. Various processes may contribute to battery aging such as electrolyte decomposition, the formation of surface films on both electrodes, compromised interparticle contact at the cathode, or formation of Co_3O_4 [46]. Due to this battery's inherent high energy density, it has great potential for various energy storage roles in the future.

Chapter 3: Mathematical Modeling Fundamentals

An equivalent circuit model (ECM) may represent a cell [2],[3],[4],[7],[10],[17],[19],[20],[29],[34],[37],[38],[42],[43],[48],[50],[51],[65],[67],[69],[70],[78],[97],[98]. For lithium-ion cells, a Randle or modified Thevenin circuit may be used. These are composed of resistances signifying cell internal resistances such as ohmic, charge transfer, and film. It also has capacitances signifying cell internal capacitances such as double layer and film. A second order Randle model is illustrated in Figure 6 followed by an example of a modified Thevenin circuit in Figure 7.

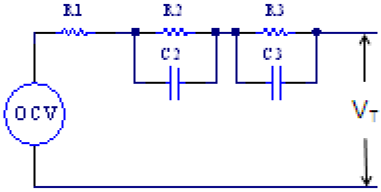

Figure 6: Second order Randle circuit [8]

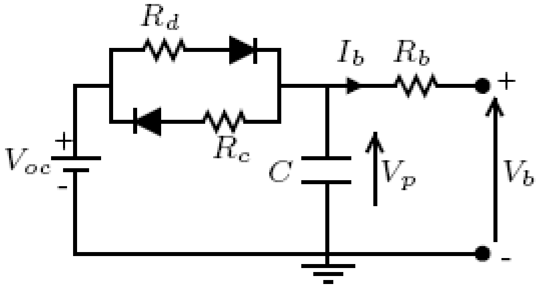

Figure 7: Modified Thevenin circuit [2]

These have been shown to represent a battery’s internal dynamics and impedance spectrum well. This model is a simplification of electrochemical processes and may not work for all cells. The validity of equivalent circuits when modeling high-energy cells remains questionable [18],[20],[56]. The parameters must be updated periodically in order to account for aging effects [48]. They are considered to be accurate in the short term [4].

An ECM may be continuous or discrete. Continuous models are based on RC circuits like the ones pictured above. They derive OCV from V_T measurements using the equation $OCV = V_T + \eta$ where η is the total cell overpotential and V_T is the terminal voltage. The discrete form, also known as state space, is a discretized version of an RC circuit. It takes the general form of

$$\begin{aligned} \dot{x}(t) &= Ax(t) + Bu(t) \\ y(t) &= Cx(t) + Du(t) \end{aligned}$$

Typical discrete time state space cell models take on the form

$$\begin{aligned} x_{k+1} &= f(x_k, u_k) + w_k \\ y_k &= g(x_k, u_k) + v_k \end{aligned}$$

where w_k is process noise and v_k is measurement noise.

Electrochemical models may also represent a cell [2],[4],[8],[13],[15],[16],[17],[18],[19],[20],[23],[25],[26],[28],[29],[32],[33],[36],[39],[40],[41], [46],[47],[49],[56],[58],[63],[100],[8],[10]; however, they are typically of greater complexity and require greater computational power. These consist of mathematical equations meant to accurately depict cell behavior. Some authors prefer an electrochemical model over an equivalent circuit model because it is able to predict physical cell limitations, such as lithium concentration depletion and saturation [23],[41],[57],[8]. Common approaches to the electrochemical model of a battery include a rigorous 2D model, a pseudo-2D model, and a single particle model. Model reduction is an important area of interest for battery management system (BMS) users. Resulting equations for solid and electrolyte concentrations (c_s and c_e) and solid and electrolyte potentials (ϕ_s and ϕ_e) are generalized below [8],[18],[23],[32],[33],[39],[40],[41],[47],[58],[82],[8].

Fick's law of diffusion:
$$\frac{\partial c_s(r,x,t)}{\partial t} = \frac{D_s}{r^2}\frac{\partial}{\partial r}\left(r^2 \frac{\partial c_s(r,x,t)}{\partial r}\right)$$

with boundary conditions:
$$\left.\frac{\partial c_s}{\partial t}\right|_{r=0} = 0 \text{ and } D_s \left.\frac{\partial c_s}{\partial t}\right|_{r=R_s} = \frac{-j^{Li}}{a_s F}$$

Electrolyte ion concentration distribution:
$$\frac{\partial \varepsilon_e c_e(x,t)}{\partial t} = \frac{\partial}{\partial x}\left(D_e^{eff}\frac{\partial}{\partial x}c_e(x,t)\right) + \frac{1-t_+^0}{F} j^{Li}(x,t)$$

with boundary conditions:
$$\left.\frac{\partial c_e}{\partial t}\right|_{x=0} = \left.\frac{\partial c_e}{\partial t}\right|_{x=L} = 0$$

Charge conservation derived from Ohm's law:
$$\frac{\partial}{\partial x}\left(\sigma^{eff}\frac{\partial}{\partial x}\phi_s(x,t)\right) - j^{Li}(x,t) = 0$$

$$\frac{\partial}{\partial x}\left(\kappa^{eff}\frac{\partial}{\partial x}\phi_e(x,t)\right) + \frac{\partial}{\partial x}\left(\kappa_D^{eff}\frac{\partial}{\partial x}\ln c_e(x,t)\right) + j^{Li}(x,t) = 0$$

with boundary conditions:
$$\left.\frac{\partial}{\partial x}\phi_e\right|_{x=0} = \left.\frac{\partial}{\partial x}\phi_e\right|_{x=L} = 0$$

Butler-Volmer equation:
$$j^{Li}(x,t) = a_s i_0(x,t)\left[\exp\left(\frac{\alpha_a F}{RT}\eta\right) - \exp\left(\frac{\alpha_c F}{RT}\eta\right)\right]$$

Overpotential:
$$\eta = \phi_s - \phi_e - U$$

where r is the radius of the electrode particle, D_s is the solid phase diffusion coefficient (cm^2·s^{-1}), ε_e is the electrolyte phase volume fraction, D_e^{eff} is the effective diffusion coefficient (cm^2·s^{-1}), t_+^0 is the transference number defined as the fraction of the current carried by that ion in a solution of uniform composition, F is Faraday's constant, j^{Li} is the lithium-ion current density (A·cm^{-3}), ϕ_s is the solid phase potential, σ^{eff} is the effective solid conductivity (S·cm^{-1}), κ^{eff} is the effective ionic conductivity (S·cm^{-1}), c_e is the lithium-ion concentration in the electrolyte phase, i_0 is the exchange current density (A·cm^{-3}), α_a is the anodic transfer coefficient, α_c is the cathodic transfer coefficient, η is the overpotential, and a_s is the interfacial surface area (cm^{-1}) calculated by [47]

$$a_s = \frac{3\varepsilon_s}{R_s}$$

where ε_e is the active material volume fraction and R_s is the maximum electrode particle radius (cm). To create a precise battery model that mimics performance in real operating conditions the underlying principles must be understood.

Different approaches to physical modeling of a battery have unique advantage and disadvantages. A single particle model represents each electrode with a single spherical particle whose surface area is equivalent to that of the active area of the solid phase in the porous electrode. Only the distance from the center of the particle to the surface, *r*, is considered. This model neglects the solution phase of the cell. A pseudo-2D model, also known as a porous electrode model, represents each electrode as multiple particles. It considers concentrations and potentials in the *r* and *y* directions. A rigorous 2D model considers solution phase concentration and potentials in the *x*, *y*, and *r* directions inside an electrode which is made up of many spheres or particles of active material.

There are different mathematical model reduction strategies such as approximating concentrations within each particle with a polynomial rather than PDEs. A polynomial is used to approximate the parabolic shape, thereby simplifying the calculation [56]. Three common assumptions made in model order reduction are 1) reaction currents are not influenced by the electrolyte concentration, 2) the Butler-Volmer equation may be linearized, and 3) ion conductivity is constant. Each have proven to significantly reduce algorithm calculation time.

All equivalent circuit or mathematical models require great computing power to reduce calculation time. Accuracy is dependent on how well the model represents the true physics. As always, algorithm robustness depends on the developer. Computational efficiency suffers as model complexity increases. Numerical stability is dependent on the type of numerical method used to solve the partial differential equations. Cost can be very high for algorithm development and hardware to run the model.

Chapter 4: Literature Review

Several SOC estimation methods have been investigated [1-70]. Each method has unique advantages and disadvantages. The evaluation criteria are based on accuracy, algorithm robustness, computational efficiency, numerical stability, and cost.

Accuracy is essential. Battery and EV/HEV manufacturers state that the SOC error target is less than or equal to 5% when compared to coulomb counting, a method that will be discussed later. It must remain accurate under varying operating conditions such as ambient temperature, current rate, vibration, humidity, and cell age. High temperatures, large SOC variance, and strenuous load profiles may accelerate battery aging, thereby changing its maximum charge capacity, Q_{max} [28]. The process must also be robust enough to handle slight variations in cell construction, attain numerical convergence, and be as inexpensive to implement and operate as possible.

SOC estimation methods can be arranged into two main categories; with or without a mathematical model. Those without are based solely on measurement. These can be arranged into three subcategories including coulomb counting, open circuit voltage (OCV), and resistance/impedance. Others, like quantum magnetism and neutron imaging, are rather new with no documented publications other than two patents. Methods with a model can be arranged into two subcategories including equivalent circuit modeling and electrochemical modeling. It is commonplace to combine SOC estimation methods with error correction techniques, such as with fuzzy logic, a Kalman filter, a state observer, or a neural network in order to increase accuracy.

4.1 Error Correction Techniques

Fuzzy logic is a many-valued logic that is fluid rather than fixed. There is a truth value that exists between 0 and 1 that corresponds to a statement being 100% false to 100% true, similar to human decision making. This allows conclusions to be drawn from ambiguous data. Information is given a subjective description, such as fast or slow. A schematic representation is shown in Figure 8.

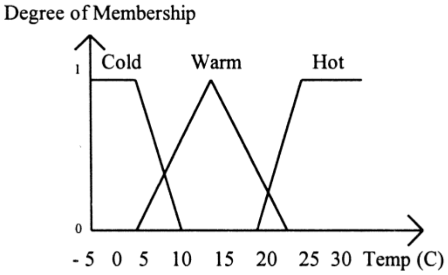

Figure 8: Fuzzy logic characterization example [70]

The input and output variables are written as “if…then” statements, also known as rules. For example, “if current is high and temperature is warm, then output is high.” Rules may be designed by an expert or inferred by previous data. A qualitative data set is collected and then mapped into a numerical range, thereby converting it to a quantitative data set that can be used to characterize a cell [10],[17],[19],[26],[34],[37],[39],[50],[51],[56],[59],[70].

In general, the fuzzy logic method is accurate if proper numerical ranges are chosen, algorithm robustness depends on the developer, computational efficiency is high since it relies on ranges of data, numerical stability is not relevant since this is not a numerical approximation, and cost is low.

Artificial neural networks act like the human brain in that they sort out patterns and assign appropriate weighting factors; essentially, they “learn.” There exists an input layer, a neutron layer, and an output layer. The neutrons accept inputs, manipulate them with weighting factors, and produce outputs, as shown in Figure 9.

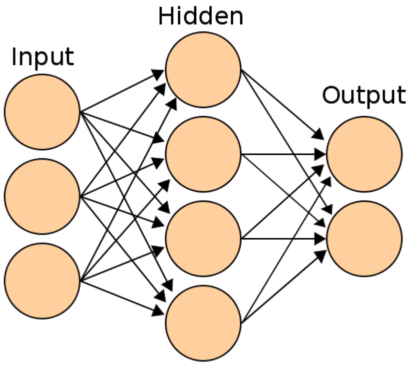

Figure 9: Artificial neural network layers [73]

It is considered a network when many neutron layers are in series. Weighting factors are continuously updated, bringing the final output closer to the true value. A key advantage to neural networks is that they can represent linear and nonlinear systems. They also can be refined with data previously gathered from a similar cell. This technique requires highly empirical components and the error may never converge to the global minimum. Training data and the training method strongly influence the error [2],[7],[10],[17],[26],[34],[37],[43],[48],[50],[51],[59],[68],[71],[73],[100].

Generally, the neural network method is accurate if weighting factors are accurate. Computational efficiency may be low if many values are sought, numerical stability if high since the weighting factors, new or from previous data, can remove any model instability, and cost may be high depending if there is a model incorporated and how complex it is.

A state observer estimates the internal states of a battery by relying on a mathematical model coupled with measurements, usually of the form shown in Figure 10.

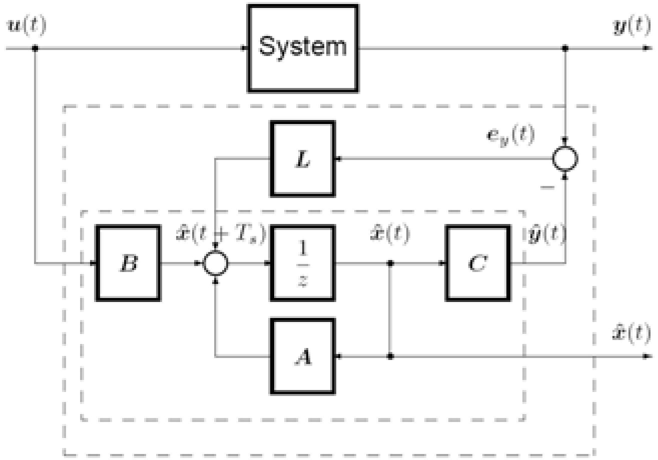

Figure 10: State observer feedback loop

with the following equations

$$\hat{x}(k+1) = A\hat{x}(k) + L[y(k) - \hat{y}(k)] + B(k)$$
$$\hat{y}(k) = C\hat{x}(k) + Du(k)$$

where, at time *k*, *x(k)* is the plant's state, *u(k)* is its inputs, *y(k)* is its outputs, and *L* is the observer gain. The hat above a variable denotes that it is an observer variable. The observer error can then be calculated as $e(k) = \hat{x}(k) - x(k) \rightarrow 0$ when $k \rightarrow \infty$. Choosing the appropriate gain is crucial.

A Kalman filter (KF) can take continuous, noisy, inaccurate data and provide data that is closer to the true values. The purpose is to remove unwanted noise. It uses input values derived from physical models and sensor measurements. First, a new state is predicted along with an associated uncertainty. Then a new measurement is taken and given an uncertainty value. A KF usually takes on the form of $x_k = F_k x_{k-1} + B_k u_k + w_k$, where F_k is the state transition model, B_k is the control-input model, and w_k is the process noise. It may take on the model form shown in Figure 11.

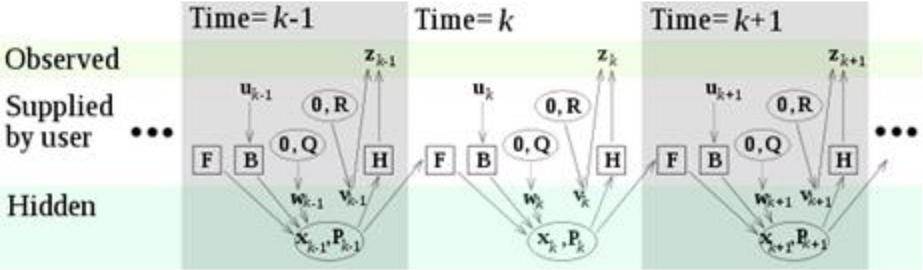

Figure 11: Kalman filter layers [72]

A weighted average scheme, where the value with the least uncertainty gets the greatest weight, produces a new state value. The estimates tend to be closer to the true values than the original measurements because the weighted average has a better estimated uncertainty than either of the values that went into the weighted average [72]. An extended Kalman filter (EKF) is a state estimator for a nonlinear system. These algorithms are often complex because there are many state variables to consider. There must be a good statistical model of the model error variance. In the flat region on the OCV curve, the SOC estimate is very sensitive to a poorly chosen model error variance. Since the model contains components that are not directly measured, selecting the error variance is difficult. If improperly chosen, the SOC variable will be noisy and may diverge. A sigma-point Kalman filter (SPKF) may correct EKF assumptions including the output random variable mean and the output random variable covariance. Rather than using Taylor-series expansions to approximate covariance matrices, a number of function evaluations are performed. Then the results are used to compute a covariance matrix. Other Kalman filter techniques include unscented (UKF), adaptive (AEKF), adaptive unscented (AUKF), and central difference (CDKF). All Kalman filters typically require significant computational power [3],[4],[7],[10],[13],[16],[17],[19],[20],[26],[33],[34],[36],[37],[38],[43],[48],[50],[51],[52],[59],[62],[63],[64],[68],[71],[72],[100].

The Kalman filter method is usually accurate if the feedback gain, physical model, and Gaussian distribution of the external noise is accurate. Computational efficiency may be low if many values are sought, numerical stability is high since the weighting factors can remove any model instability, and cost may be high depending on the complexity of the model.

4.2 SOC Estimation without a Model

Included in this section are SOC estimation methods that rely on direct measurement. There is no complex mathematical manipulation of the input or output data. Most methods presented here require a lookup table to be generated before implementation for reference purposes.

Coulomb counting calculates SOC by integrating the measured current with time, resulting in units of ampere-seconds or coulombs, which are then converted to Ah. Current sensing techniques include the use a shunt resistor, Hall effect transducer, or giant magnetoresistance (GMR) sensor. Industry favors Hall effect transducers for their reliable operation and low cost, even though they are susceptible to noise. Ah are inserted into a cell during charging and extracted during discharging. The calculation is as follows

$$SOC(t) = SOC(0) - \frac{\int_0^t \eta \cdot i \cdot dt}{Q_{\max}} \times 100\%$$

where η is the efficiency coefficient defined as

$$\eta = \frac{Q_{discharge}}{Q_{charge}}$$

where $Q_{discharge}$ and Q_{charge} are the measured charge output during a full discharge and input during a full charge, respectively.

An inherent problem is that η is different for charging and discharging. A lithium-ion polymer battery will deliver less charge than the amount input during charging. This is due to charge losses accrued from lithium-ions plating out on the anode during charging [23],[30],[45],[50]. As a result, the amount of electrochemically active Li^+ ions will be reduced [46]. Typical values for η are 1.0 during charge and 0.98-1.0 during discharge [13],[42],[50],[63],[71].

Coulomb counting has several drawbacks. It is not possible to determine the initial SOC by measurement. The initial SOC may be estimated by recalling the previous coulomb counting history, which may already have an offset error [2],[26],[61],[81]. Also, since this method is based on current measurement any sensor offset errors will accumulate and further compromise accuracy [2],[3],[7],[10],[13],[15],[16],[26],[30],[35],[37],[42],[43],[48],[49],[50],[51],[55],[59],[61],[68],[71],[74],[75],[76],[78],[79],[81],[84],[92],[98],[100],[101],[104],[105],[13],[10]. The initial SOCs are defined to be zero or one hundred percent when fully discharged or charged, respectively. Internal side reactions and self-discharging cause errors that accumulate with time [20],[56],[59],[61],[74]. Recalibration is required to remove accumulated error [2],[10],[16],[30],[34],[35],[42],[48],[51],[68],[71],[74],[75]. To obtain an exact updated charge capacity a cell would have to undergo a full charge/discharge. This requires a long time, subjects the battery to possible over/undercharge, and shortens a cell’s life each time [13],[16],[17],[23],[30],[35],[61],[63],[68],[84],[100]. Another factor to consider is that current integration in a real world application will not be continuous. This means that the sampling rate much be fast enough to capture any sudden load change [26],[41],[61],[98].

The relation between charge capacity and charge extracted is nonlinear due to the multitude of factors that may affect it. These include, but are not limited to, the cell voltage and temperature, the rate at which cells have been charged and discharged, the chemical composition of the various active chemicals and any doping which has been used, the possibility and effects of contamination, the shape and length of the physical current paths within the cell, the volume of electrolyte, the thickness of the electrolyte and the separator, the resistivity of the components, the rate of mass transfer of the ions through the electrolyte, the rate of chemical action at the surface of the electrodes or the rate of absorption of the ions into the intercalation layers, the actual surface area of the electrodes, the effective surface area of the electrodes taking into account the particle sizes of the chemicals, the effect of passivation on the electrode surface, the ambient temperature, the Joule heating effect, the self discharge rate of the cells, and the time between charges [2],[4],[13],[23],[27],[30],[31],[34],[45],[48],[50],[55],[59],[61],[65],[68],[71],[74],[84],[98],[106],[107].

Q_{max} depends on temperature and age of the battery [2],[27],[29],[35],[45],[55],[59],[61],[71],[74]. A cell loses active material and consequently full charge capacity as it experiences cycling or harsh environments [23]. Examples of degradation modes include loss of active material sites in either electrode, growth of a solid electrolyte interface (SEI) layer on the anode, and material structural changes causing increased diffusion impedance at the cathode [23]. Ohmic and transport limitations reduce available capacity at high rates [47]. The fact that temperature and battery age affect SOC is common for all methods in this study.

Coulomb counting is accurate as long as the initial SOC is known and the current sensor error is small. It is a direct measurement method so there is no need to assess algorithm robustness, computational efficiency, or numerical stability. Cost of implementation is relatively low, but may increase with the number and accuracy of sensors.

OCV is a lookup table approach. It requires an OCV curve be generated initially by charging/discharging a cell at low current for finite times with rest periods between loadings until it is fully charged/discharged [42]. The current is integrated during loading using the coulomb counting process and a corresponding SOC is linked to a measured rest period cell voltage that is considered to be the OCV [2],[13]. These values are stored in a lookup table and referenced during battery operation.

OCV is inaccurate when there is external current flowing through a cell [16],[20],[34],[38],[43],[46],[50],[54],[55],[59],[61],[63],[67],[68],[71],[74],[79],[83],[85],[88],[90],[93],[94],[96],[100],[101],[103],[13],[10]. The measured terminal voltage (V_T) differs from the OCV due to overpotentials inside the cell and any external voltage losses [16],[20],[34],[55],[61].

Overpotentials include activation, concentration, and ohmic. Lithium-ion polymer cells exhibit a nearly flat OCV-SOC relationship slope from approximately 20-80% SOC so a highly accurate voltage sensor would be needed [20],[26],[34],[50],[66],[71],[79],[80],[90],[99],[13]. Another factor is that identical batteries may have slight variations in their OCV curves [38]. A battery’s OCV curve may change nonlinearly with the ambient temperature and degradation from age [2],[7],[13],[26],[34],[45],[59],[65],[71],[77]. It has been demonstrated that the OCV-SOC relationship does not change during cycling of the battery, if SOC is expressed in relative capacity [45],[54],[59]. Multiple lookup tables would have to be generated in order to cover the range of expected temperatures. Figure 12 shows a typical lithium-ion polymer OCV-SOC curve, with the solid line representing an aged battery.

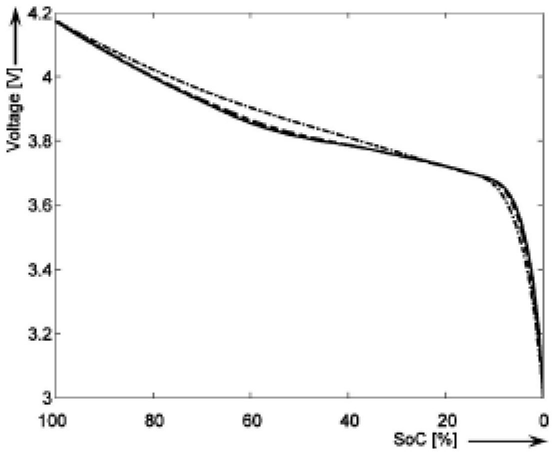

Figure 12: Typical OCV-SOC curve [46]

In general, the OCV method is accurate only when the battery has been at rest for an extended period of time. OCV without a model is a direct measurement method so there is no need to assess algorithm robustness, computational efficiency, or numerical stability. Cost is very cheap since a voltage sensor and stored lookup tables are the only components.

The resistance/impedance is another lookup table approach. Active material in the cell and corresponding resistance/impedance changes as the anode and cathode alter charge state. Resistance (*R*) is voltage divided by a DC current, written as $R = \frac{V}{I}$. Impedance (*Z*) is voltage divided by an AC current, written as $Z = \frac{V}{I}$, where $V = |V| e^{j(\omega t + \phi V)}$ and $I = |I| e^{j(\omega t + \phi I)}$. This is similar to resistance only it includes the phase angle. Impedance measurement entails imposing a frequency sweep on the battery, typically 10kHz-1mHz, offering the opportunity to reach conclusions about internal processes with unique time constraints [1],[7],[29],[34],[61],[69]. This is accomplished with the use of an electrochemical impedance spectroscopy (EIS) machine.

There are two EIS operation modes: galvanostatic and potentiostatic. The former refers to the manner of applying an AC current while measuring the cell voltage response and the latter refers to the manner of applying an AC voltage while measuring the current response. Voltage fluctuation must be kept less than or equal to 10mV in order to ensure impedance measurements are conducted under linear conditions [59]. When results are presented in the form of a Nyquist plot with the negative imaginary part on the y-axis and the positive real part on the x-axis, semicircles followed by a linear slope may be seen, as depicted in Figure 13.

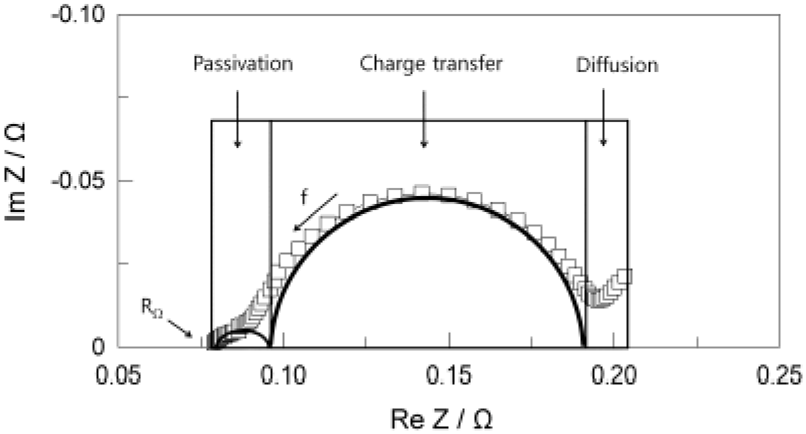

Figure 13: EIS shape analysis [7]

X-axis intersection points, maximum semicircle heights, and linear section slopes each represent a specific internal component. It has been discovered that the resistive components represent the current collectors, electrolyte, bulk of the electrode materials, and transfer reactions at the electrode surfaces. Capacitive components represent the double-layer capacitance. Inductive components represent the porous nature of the electrodes [69]. When these values are fit to a battery equivalent circuit model, particular parameters may be extracted. *R* and *Z* are measured using an ohmmeter and impedance spectroscope, respectively, and correlated to a SOC in a lookup table.

Similar to OCV, *R* is nonlinear with respect to charge/discharge rate, ambient temperature, and age [1],[27],[34],[35],[42],[59],[61],[68],[69],[71],[100]. *Z* measurements have the same disadvantages; only certain aspects of the frequency spectrum are not proportional to the available capacity of the cell [35]. An additional drawback is that the *R/Z* method requires a constant DC/AC current, respectively, making measurements inaccurate under real battery demand conditions [16],[51],[55],[63],[68],[71],[105]. Both of these methods are indicative only, meaning that a lookup table would have to be generated for various operating conditions. Also, identical batteries may have slight variations in *R/Z* [28].

Classically, the *R/Z* method is only accurate when the current and ambient temperature are constant. It is a direct method so there is no need to assess algorithm robustness, computational efficiency, or numerical stability. Cost of measuring internal resistance is very low, but cost of an impedance spectrometer can be high.

4.2.1 Literature Rundown

An enhanced coulomb counting method has been conceived in which the initial SOC is read from memory while making use of the efficiency factor η, Ah are counted during loading, and recalibration occurs every time the battery reaches 0 or 100% SOC as stated by the manufacturer, where $\eta = \frac{Q_{discharge}}{Q_{charge}} \times 100$. Also, there is a self-discharge correction for batteries being stored for extended durations. All experiments have been at room temperature. Linear equations to determine SOC are derived during charging at 1C by plotting the voltage versus SOC in constant current (CC) mode and current versus SOC in constant voltage (CV) mode. Multiple lookup tables would have to be generated at various currents, ambient temperatures, and cycle-ages. Experiments showed that batteries have a higher charging efficiency factor at lower SOC. The opposite holds true for the discharge efficiency factor. By periodically updating the efficiency factors, long-term error can be minimized [30].

A two-pulse method has been suggested by which a battery at rest is subjected to a 10 second pulse of constant load current of known magnitude. The voltage drop is recorded during the pulse. Then the battery rests for ten seconds. At the end of the rest period, the terminal voltage is measured (V_{max}). A second load current pulse, identical to the first, is applied for another ten seconds while the voltage drop is again measured (ΔV_2). V_{max} is assumed to be equal to OCV. The SOC is deduced from V_{max} by recalling an OCV curve for the battery at a specified temperature. There was proven to be a linear relationship between the C-rate used and ΔV_2. C-rate is deduced from previously generated tables. Using the equation $C_{rate} = \frac{I}{Q_{\max}}$, a new value for Q_{max} can be calculated. It has been confirmed that the second pulse gives consistent results as a battery ages. This study was conducted on valve-regulated lead-acid batteries at room temperature, so future work should expand this concept to other types and batteries and ambient temperatures [35]. The same authors previously mentioned wrote an earlier paper describing an estimation SOC method using a combination of terminal voltage, current, and impedance measurements. A complex equivalent circuit model, similar to a 6th order Randle model, was implemented. 1kHz was the frequency used for impedance measurement. The impedance was normalized and used in conjunction with the change in voltage to estimate SOC in the hyperbolic OCV-SOC regions near 0 and 100% SOC. Two equations are given; $OCV = V_T(\theta) + (C_R\beta_1)Z_{nom0}$ for the linear OCV-SOC region and $OCV = V_T(\theta) + C_R\beta_2 + (Z_{nom0} - Z_{nom1})\beta_3$ for the hyperbolic regions, where $C_{rate} = \frac{I}{Q_{\max}}$ and β_1, β_2, and β_3 are found through experimentation. The normalized impedance at fully charged or depleted SOC is periodically updated to help account for aging. Future work would be to update Q_{max} and analyze ambient temperature effects [42].

A paper has described how to model battery behavior. The OCV-SOC curve is generated by applying a small current from 100% SOC to 0% SOC. The small current is intended to remove overpotentials; however, they still exist. A better approach would be to discharge with a small current for a short amount of time, rest for at least 2 hours, then record the terminal voltage at the end of rest and consider that to be the OCV since all overpotentials will have been completely removed. The OCV-SOC shifts upward with decreasing ambient temperature, although negative temperatures have not been studied. Overpotentials increase with current rate and cell age. The overpotential model includes ohmic, kinetic, and diffusion overpotential, and considers temperature. The OCV technique is only applicable when the battery is at rest, so it was recommended to use coulomb counting with overpotential prediction [54].

It has been stated that there are three reasons why a battery's measured voltage does not equal its OCV: ohmic voltage loss, voltage loss caused by charge transfer, and voltage loss caused by diffusion. Ohmic voltage loss does not have a time delay and is constant. Voltage loss caused by charge transfer has a time delay and is then constant. Voltage loss caused by diffusion has a time delay and then increases with time. Rest time after loading before taking an EIS reading is considered arbitrary. There are five sections of the Nyquist plot: Section 1) at very high frequencies the spectrum shows inductive behavior caused by inductive reactances of metallic elements in the cell and wires, 2) ohmic resistance (R_{Ω}) of the cell at the intersection with the real axis, sum of the resistances of current collectors, active material, electrolyte, and separator, 3) first semicircle associated typically with the SEI and is formed during cycling on the surface of the anode, 4) second semicircle representing the double layer capacity and charge transfer resistance at the electrodes, and 5) linear slope represents the diffusion processes in the active material of the electrodes at very low frequencies. SEI resistance and double layer resistance increase at lower temperatures. R_Ω increases with temperature, yet does not change with SOC making it alone a poor indication of SOC for lithium-ion cells [1].

It has been stated that the first x-axis intersection point in a Nyquist plot corresponds to the R_Ω, the high frequency semicircle shows components of passivation, the large semicircle shows the charge transfer reaction, and the low frequency linear region shows diffusion. The radius of the large semicircle decreases from 20% to 80% SOC and then increases from 80% to 100% SOC. A polynomial of degree three was then curve fit to the time constant of two components of the cell at various SOCs. The time constants of those specific components, namely the left and right intercepts of the large semicircle, can be continuously monitored and compared to values in a lookup table [7].

Phase has been deemed an accurate SOC estimation indicator. A constant 40Hz AC current was applied to two different coin-type cells while they were being cycled. Both cells have exhibited phase increases while charging and phase decreases while discharging. A simple model of two resistors and a constant phase element has been proposed to describe the behavior. When the phase variance was plotted versus SOC, a near-linear trend appears [27].

AC impedance alone has been used to determine SOC of a battery. Multiple equivalent circuit models have been fitted to battery impedance data with multiple conclusions drawn as to which component of the Nyquist plot corresponded to which component of the model. Many different battery types have been examined. The resulting Nyquist plot for a lithium cell shows a high frequency inductive loop and two lower frequency capacitive semicircles. The inductive loop is attributed to the electrode porosity and the capacitive semicircles are attributed to the electrode process. The equivalent series capacitance at 25mHz varies linearly with SOC, so it was the most promising parameter to monitor [69].

Neutron radiography has been used to physically measure the lithium concentration across battery electrodes at low current rates. A neutron beam is attenuated as it passed through a cell, producing a 2D projection. The number of neutrons counted is given by a Poisson distribution and stroboscopic averaging is used to account for limitations of the imaging equipment. The change in beam intensity is proportional to the Li concentration in the solid electrodes. Observed blurring in the neutron images are attributed to in-plane roughness or curvature of the battery. The effects of high current behavior remain unknown. While this may provide accurate results in a lab setting, it is impractical for use in a HEV/EV [22].

A battery state flowchart has been produced. Five states are mentioned including initial, standby, charge, transitional, and discharge; each defined by the measured current and voltage of the battery. When there is no external current flow, OCV is used to determine SOC. When there is external current flow, coulomb counting is used. Aging is considered by updating Q_{max} using $Q_{\max} = \frac{100}{SOC_{sf} - SOC_{si}} Q_{ch}$, where SOC_{si} and SOC_{sf} denote the initial and final SOC in the standby state, respectively, and Q_{ch} denotes the amount of charge flowing into the battery during the charge state. A disadvantage to this approach is that is requires two separate rest periods to calculate SOC_{si} and SOC_{sf}. An SOC error is 1.2% was observed when compared to coulomb counting alone [31]. The same authors wrote an earlier paper describing the concept of the multiple-state model. Overpotentials are modeled as ohmic, kinetic, and diffusion resistances. The effects of aging on the total overpotential may be determined by $\eta_d^a = \eta_d^f \frac{\eta_{ch}^a}{\eta_{ch}^f}$ where *a* represents aged, *f* represents fresh, *d* represents discharge, and *ch* represents charge [45].

A battery mathematical model has been presented that predicts OCV using experimental aging data. OCV is shown to decrease at constant SOC, noticeably after hundreds of cycles. OCV and coulomb counting methods estimate SOC separately. Those estimates are given weight factors determined empirically at different current rates and ambient temperatures. The final SOC is a combination of weighted OCV and coulomb counting estimates. High current rates were not considered [55].

A method has been presented that uses OCV to determine SOC when a battery has been at rest for a while. This eliminated effects of self-discharge. Coulomb counting was then used during load operation. Impedance measurements were found to suffer from transient effects and cell aging, so it was continuously updated in order to predict cell terminal voltage [61].

Yet another lookup table approach is quantum magnetism. A cell is polarized by external means and the resultant magnetic field attractive force is measured, following the equation $F = q(V \times B)$. Intercalation/deintercalation alters an electrode's structure thereby modifying its magnetic field susceptibility [80],[90]. The resultant change in attractive force is sensed and correlated to a SOC in a lookup table. The magnetic sensor accuracy must be great since the change in attractive force is on the order of mN. This method is fairly new and has not yet had any published journal articles describing its merit. The effects of polarizing a cell remain unknown. This method also has the drawback that it might not be possible to put windings around each individual battery inside a battery pack without significant interference issues.

4.3 SOC Estimation with a Model

The methods discussed in this section all use mathematical strategies to improve SOC estimates. They may take the form of an equivalent circuit model or electrochemical model.

4.3.1 Literature Rundown

A hybrid method has been developed wherein OCV is used to estimate SOC when a battery has been at rest for an appropriate length of time and coulomb counting is used when there is ion flow. An equivalent circuit model with a reduced-order state space observer accurately predicted SOC, while considering aging effects by magnifying the battery’s nominal impedance value by 2. The observer was of the form

$$\begin{aligned}\dot{\hat{x}} &= A\hat{x} + Bu + G(C\hat{x} - y)\\ \hat{y} &= C\hat{x}\end{aligned}$$

[2].

A modified Thevenin equivalent circuit has modeled a battery. The components include ohmic resistance, electrochemical polarization resistance, concentration polarization resistance, electrochemical polarization capacitance, concentration polarization capacitance, and OCV. OCV is defined as the average of OCVs recorded during charging and discharging in order to eliminate the effect of hysteresis. The ohmic resistance is found to be independent of the load current, but rather proportional to SOC. An EKF algorithm is implemented and circuit parameters identified. Coulombic efficiency was found to decrease as current rate increases, although it was always greater for discharging. The adaptive EKF monitors changes in the dynamics of the target, treating them as noise or modifying the model parameters. The AEKF has superior accuracy when compared to an EKF [3].

A screening process combined with an extended Kalman filter has been suggested. The screening process first decides which group of cells has similar characteristics within a battery pack and selected an appropriate equivalent circuit model to represent them. Then the extended Kalman filter uses the selected model along with measurements to estimate SOC. Error of ± 5% was documented when this method was compared to coulomb counting [4].

A reduced order model has been developed based on porous electrode theory. This means that the electrodes are represented as multiple spheres spanning the thickness. The Li-ions diffuse into and out of these spheres. Multiple microcells are linked to mimic a single pouch type cell. Three main assumptions are made including the reaction current not being influenced by the electrolyte concentration, the Butler-Volmer equation may be linearized, and the ion conductivity is held constant. The nonlinear ion concentration PDEs are replaced with ODEs using a polynomial approach and the definition of SOC is altered to include electrode Li concentrations even at 0 or 100% SOC. Calculation time is drastically reduced when compared to the full order model [8]. The same authors compared terminal voltage and SOC results of the reduced order model with the full order model, equivalent circuit model, and experimental data. Two current conditions are tested, constant and pulse. The proposed ROM achieves an SOC estimation error of less than 1% during a full discharge. It also demonstrates a significant drop in calculation time; from 79 seconds with the full order model to 8.7 seconds at 1C. Ongoing research will focus on the ROM response to high current rates, up to 10C, as well as heat generation at various ambient temperatures. Implementation of a feedback control loop may further increase accuracy [8].

ECM parameters have been derived using an algebraic method. It has been proven that a 1st order Randle model poorly depicts battery dynamics, a 2nd order model improves that response, and a 3rd order model almost perfectly matches experimental data. A 2nd order model provides the greatest efficiency, calculated as a ratio of the relative accuracy to calculation time [4].

The Nernst equation has been used to relate OCV with SOC in conjunction with a first order Randle ECM. A recursive least squares method extracts parameters by weighting recent data heavier than old data. SOC estimates are used to update the model and then the model is used to update SOC. The model performs well under hybrid pulse power characterization (HPPC) and dynamics stress test (DST) simulations when compared to experimental data, with a maximum SOC error of 2.1%. The ECM parameters will need to be updated as the battery ages [4].

A paper has focused on the model order reduction process. Six techniques for converting diffusion PDEs to ODEs are investigated, including the Analytical Method (AM), Integral Method Approximation (IMA), Padé Approximation Method (PAM), Finite Element Method (FEM), Finite Difference Method (FDM), and Ritz Method (RM). The goal is to determine which method most quickly provides diffusion dynamics results within an error threshold of a porous electrode electrochemical model. The PAM proves to offer the best convergence [10].

An adaptive algorithm has been developed that identifies model parameters for a second order Randle ECM. By computing an observer gain and estimation error, new battery parameters can be extracted. SOC is calculated as a weighted average of estimates from coulomb counting and the ECM. The SOC estimation error is less than 3%. The inherent coulomb counting problem of accumulation of error remains an issue [13].

A state space model has been presented in which a nonlinear Luenberger observer with a KF is applied to an ECM. Simulations results of the ECM match an existing non-model SOC algorithm. The proposed ECM was not validated experimentally, and ambient temperature and battery age were not considered [10].

An adaptive unscented Kalman filter approach has been presented based on a zero-state hysteresis battery model. The AUKF adaptively adjusts the covariance values of the process and measurement noise based on the output voltage residual sequence. It was shown to have superior performance when compared to EKF, AEKF, and UKF. This method has a relatively low computational power requirement. Future work should be on replacing the zero-state hysteresis model with a model that more accurately predicts battery dynamics, especially during relaxation [10].

A radial basis function (RBF) neural network was used in conjunction with an extended Kalman filter to estimate SOC. The neural network is trained by using coulomb counting data from a previously cycled battery. Inputs to the neural network are the terminal voltage at the previous time step, the SOC at the present time step, and the current at the present time step. The RMS error is calculated to be 3%. The initial training of the neural network will become obsolete as the battery ages. It is suggested that lookup tables be created for range of ambient temperatures since this work focused only on room temperature [13].

A single particle model has been used to model a cell. Accuracy is lost at current rates above 1C because the model assumes spatial averages in concentration over the electrodes even though in actuality the concentration is non-uniform [15].

A discrete state space model based on an equivalent circuit has been used. The estimator is designed in such a way as to eliminate the need for a recursive gain calculation. A linear parameter varying (LPV) technique is utilized for its low computational power requirement, being at most half that needed for a Kalman filter. A RMS error of 4% is observed, yet only room temperature is considered [16].

An adaptive Luenberger observer based on an equivalent RC circuit has been used to estimate SOC of a battery pack. The gain is continuously adjusted to minimize error between the model estimated voltage and the measured terminal voltage. The Hybrid Pulse Power Characterization (HPPC) test is performed on a cell while a numerically nonlinear least squares algorithm determines the unknown model parameters. The circuit model is not capable of accounting for heat generation in a cell [17].

A reduced order partial differential algebraic equations (PDAE) mathematical model has been created with the assumptions that the lithium concentration in the electrolyte is uniform. Also, the mass transfer in the solid material is approximated in the radial direction in terms of volume averaged concentration, particle surface concentration, and averaged concentration flux. There are two observer gains since the positive electrode is made of two materials. The model has difficulty tracking true values when high current rates with subsequent high heat generation rates are experienced. Validation of the estimated overpotentials requires reliable measurements of the potential distribution across the electrodes, which is not easy to obtain [18].

A 1D electrochemical model has been developed with the assumption that the reactions occur on the surface of the electrodes. Another is that the OCV depends on the lithium concentration in the electrolyte adjacent to the electrode. An EKF is implemented using Euler's method to discretize the model. The method proves an increase in accuracy over traditional EKFs and sliding-mode observers, yet it does not account for lithium-ion concentration distribution within the electrodes [19].

A porous electrode based model including high current rate limitations has been created together with an unscented filter. These limitations include diffusion restraints in the electrolyte and solid phase transport. The unscented filter uses sigma-points chosen based on the variance of the measured variable to map the nonlinearities of the measured variables to that in the state variables. The sigma-points are the eigenvalues of the Cholesky decomposition of the covariance matrix. It does not require linearization of the system equations, thereby reducing computational power requirements. Each electrode is modeled as spherical particles arranged along the thickness. To make the model quicker, diffusion and kinetic parameters are held constant and thermal effects are assumed to be negligible. Capacity fade was not considered, but may be deduced from model parameters upon further investigation [20].

Modeling constraint management during pulse operation has been investigated. An electrochemical model with a linear filter is used; however, the linear filter performs poorly when the SOC was outside the range of 30-70%. It is stated that the ratio of Li concentration in the anode to the maximum allowable in the anode must always be between zero and one. The model order reduction procedure groups together modes that have similar eigenvalues, and are still able to reproduce varying frequency response of diffusion. A Kalman filter is added to reduce process and measurement noise. Electrode surface stoichiometries are found to change much faster than SOC since they are more closely coupled to the recent charge/discharge history. Model convergence time could be decreased with less noisy current sensors. Controls should be implemented that allow pulse charging of a battery beyond its manufacturer-specified maximum voltage without significant lithium plating side reactions on the anode surface. It has been observed that the positive electrode shows a much stronger dependency on surface stoichiometry than does the negative electrode. It is suggested that future work focus on model parameter adaptation as a battery ages [23]. The same authors' previous work was designing a linear Kalman filter based on a reduced order electrochemical model. There are six states in the state space model including five that describe positive and negative electrode solid-state concentration gradient dynamics and one that describes electrolyte concentration gradient dynamics. This is much easier to solve than the author's previous 313th order nonlinear finite-volume model. Reduction of the model from 5 to 3 states does not have much effect of SOC estimation error. The linear KF performs well only when SOC remains in the range 30-70%. Future work should focus on identifying battery degradation [40]. An earlier paper by the same authors presents a 1D electrochemical model under the assumptions of quasi-linear behavior and decouples the local reaction current from the electrolyte concentration. A detailed description is given for the electrochemical model and reduced order support vector machine (SVM) state space transfer functions. The bandwidth range is altered to be 0-10Hz. The higher the current rate, the greater the order of the model needs to be to capture electrode surface saturation/depletion nonlinearities. The electrode surface lithium concentrations are used to estimate SOC. A 313th order nonlinear CFD model is reduced to a 12th order state variable model and accuracy remains within 1%. The model still requires high computational power [47].

A thesis by K. A. Smith has incorporated a solid-state diffusion model into a 1D electrochemical model and then reduced its order. This limits the high current rate performance by protecting the electrodes from lithium saturation and depletion. Model parameters are gathered experimentally since he was not allowed to disassemble a cell. Surface concentrations are found to change much quicker than bulk concentrations. A potential difference limit, rather than a manufacturer terminal voltage limit, is introduced which allowed more efficient, faster charging of a battery. More heat is found to be generated at lower ambient temperatures. Electrode surface concentration is taken as an average and electrolyte concentration is taken on a distributed basis. A KF is implemented which demonstrated improved computational efficiency. Future work would include studying the effects of ambient temperature on the model, upgrading the KF to an EKF, further order reduction if possible, and model validation through the lifetime of a battery [58].

EIS has been combined with fuzzy logic methodology. A Sugeno fuzzy model and center-of-gravity defuzzification method are used. It has been demonstrated that the real value of resistance grows as SOC decreases. It is also shown that the resistance decreases as the DC offset current increases [25].

A mixed algorithm combining coulomb counting with a second order Randle equivalent circuit mathematical model has been presented. A low accuracy Hall effect current sensor and voltage sensor are used to better simulate realistic onboard EV/HEV systems. The model is able to compute OCV from current and voltage measurements. The coulomb counting component of the mixed algorithm captures quick changes in SOC while the model component corrects the long-term coulomb counting accumulated errors. The two components are coalesced into a single closed loop scheme, with gains chosen to minimize steady state and dynamic error. The algorithm has proven to be more stable than coulomb counting alone [26]. The same authors go into more detail of their mixed algorithm in another paper. SOC estimations based on coulomb counting using a highly accurate current sensor proves to diverge considerably from those using a standard current sensor. A close-loop controller is used. The equivalent circuit cell model represents the plant of the control system, SOC based on coulomb counting is the input variable, and voltage is the output. The reference output is the measured cell voltage. The measured current is a disturbance. An integral gain is incorporated. Future work is to test the algorithm at temperatures other than room temperature [34].

A discretized equivalent circuit model with a dual extended Kalman filter has been developed in order to estimate the battery's ohmic resistance, which is monitored experimentally for hundreds of cycles and then correlated to SOH. Ohmic resistance variation increases with the number of cycles [28].

A remapped Randle equivalent circuit has been presented. The model shows advantages for the estimation of the components associated with the electrochemical transient effects within the battery. This is due to having two states in parallel rather than in series as in the Randle model. Error is reduced when an Utkin observer and Kalman filter are applied. The main charge store capacitor (C_b) in the model is shown to vary proportionally with Q_{max}. By monitoring C_b, it is proven possible to update SOC so that its range always remains 0-100% [29].

Two reduced order particle-based models have been suggested. The electrode averaged model (EAM) assumes that the electrolyte concentration is held constant and neglects both the solid concentration distribution along the electrode and the spatial dependence of the Butler-Volmer current. A finite difference method converts the PDEs to ODEs. The state values model (SVM) divides the governing equations into submodels in order to derive analytical transfer functions. The EAM presents accurate SOC estimation but is highly sensitive to nonlinear model parameters. The SVM is stable but provides poor SOC estimation [32]. The same authors also describe an electrochemical model of a cell has been simplified by holding the electrolyte concentration constant and neglecting the solid concentration distribution along the electrode. Also, the spatial dependence of the Butler-Volmer current is ignored and is instead an average across the electrode, thereby representing the solid material as a single particle. An extended Kalman filter is applied with good results [33]. The same authors have a third paper describing the same model mentioned previously [36]. A fourth paper by the same authors describes the original electrochemical model, in which the parameters are obtained empirically. SOC is defined by the positive electrode stoichiometry as follows $SOC(t) = \frac{\theta - \theta^{0\%}}{\theta^{100\%} - \theta^{0\%}}$ [41].

An equivalent circuit model has been coupled with a sliding-mode observer. Nonlinear unknown disturbance is added to the model in order to increase accuracy. Models parameters are extracted from multiple tests using an equivalent circuit model. The results prove that the observer provides true SOC estimations even when model parameters have errors. Total SOC error is within 3% when compared to coulomb counting alone. Ambient temperatures other than 25°C and high currents have yet to be evaluated [37].

A new OCV-SOC relationship has been presented. Since similar batteries may have slight differences in their OCV curves, the curves need to be normalized in order to use the same OCV-SOC curve for each battery. Normalization is achieved by arbitrarily choosing a cutoff OCV and associated SOC. A first order Randle equivalent circuit is used to model the battery. A dual EKF is utilized, one being a state filter for SOC and the other a weight filter for capacity. A modified SOC is derived from the normalized OCV-SOC curve. The conventionally defined SOC becomes $SOC_{conventional} = \frac{SOC_{\mathrm{mod}ified}}{1 - SOC_{cutoff}}$ [38].

A porous electrode model has been provided which includes high rate limitations with an unscented filter. The unscented filter is ideal due to the nonlinearity of the physical equations at high current rates. A single particle model assumes that the concentration and potential changes in the solution phase are negligible. A porous electrode model includes the spatial distribution of concentration and potential along an electrode as well as voltage drop across the electrolyte. It is stated that an EKF does not accurately capture nonlinearities in the battery response during high currents. An unscented filter using sigma points is used instead. A single particle model is shown to only be accurate when there is little process noise. SOC estimation error with the unscented filter is < 3% while still providing physical insight of the battery [39].

A reduced order equivalent circuit model with an extended Kalman filter has been presented. The proposed model is a modified version of the first order Randle model, in which the series resistance is replaced with a parallel path of two identical resistances with diodes. It is claimed to better represent hysteresis by allowing the current direction to determine the internal resistance value. Reduction of the model comes at the cost of omitting the fast dynamics.

Measurement noise and data rejection are included in the EKF model, bringing its SOC estimation error to within 2%. Ambient temperatures other than 25°C and high currents have yet to be evaluated [43].

An EMF model has been described. Lithium-ion cell hysteresis, although small, maintains a constant form during aging. This is found to be true at all temperatures. EMF or OCV, however, changes with aging and can lead to SOC estimation errors of more than 10% if only a fresh cell SOC-OCV curve is used for measurement. The battery OCV drop is directly linked to the positive electrode decomposition. This adaptive EMF model is used in future electrochemical models to reduce SOC estimation error [46].

A combination RC and hysteresis model has been offered. Hysteresis is minimal in lithium-ion batteries so it may be neglected. The equivalent circuit model has three resistors and two capacitors, the values of which are determined empirically. SOC is determined via an EKF from terminal voltage and current measurements. Error is found to be within 2% when compared to coulomb counting. This will increase with time unless the equivalent circuit parameters are periodically updated, which would require a significant amount of time for the battery to be out of regular operation. Low temperatures and high current rates cause error to grow beyond 2% [48].

An EKF with a parameter estimator has been developed. It is designed for NiMH batteries but would also be applicable to lithium-ion. Diffusion is found to have the most profound effect on SOC. Great computational power is required to run the EKF and only room temperature was considered in the study [49].

A model-based Kalman filter SOC estimation technique has been proposed. The model is an equivalent circuit model with 3 resistors and 2 capacitors, which is said to identify cell parameters easier than previously proposed models. The KF is expanded to an EKF to account for nonlinearities in the model, with a resulting error of less than 3%. The EKF helps correct errors caused by model order reduction but it requires significant computational power [50].

A sliding-mode observer SOC estimation method has been presented for a lithium-ion polymer battery. It is chosen for its simple control structure and robust tracking performance. A first order Randle model is used to capture the battery dynamics. Model parameters are extracted experimentally; however, it is noted that resistances will change with SOC. It has been proven that they will also change with current rate and ambient temperature, making the equivalent circuit model inaccurate. The Lyapunov inequality equation prove that the observer will converge and error is found to be < 3% when compared to coulomb counting [51].

Advanced algorithms using sequential probabilistic inference or optimal estimation theory have been studied. Sigma-point Kalman filters (SPKF) have outperformed EKFs in SOC estimation. State vectors such as SOC or current changed quickly while parameter vectors such as resistance increases change over a long period of time. A discrete-time state space model is used, of the form

$$\begin{aligned} SOC_{k+1} &= e^{-\phi \cdot t_{eff}} SOC_k + w_k \\ y_k &= OCV(SOC_k) + v_k \end{aligned}$$

where model parameters are estimated in real time to account for any manufacturing differences between cells and to track the effects of aging. SOC estimation error is found to be less with the SPKF than with other types of filters [52]. The same author described a square-root SPKF in another paper and proved that it is more numerically efficient. SOC estimation errors are reduced to less than 1% [53]. An earlier paper by the same author describes several state space cell models that incorporate Kalman filters. These models are able to demonstrate the effects of cell relaxation, internal resistance, and hysteresis [66].

A review of lithium-ion battery models has been conducted. It is stated that the porous electrode approach models a battery well but is time consuming to calculate while the single particle approach requires less time but neglects solution phase diffusion limitations. Using polynomial approximations with the porous electrode approach reduces calculation time while maintaining model accuracy [56]. The same authors present an EKF model that uses terminal voltage measurements to estimate SOC. The change in Q_{max} with aging is not considered. SOC is based on the ratio of the concentration of Li-ions in the negative electrode to the maximum in the negative electrode [57].

A state space model with an EKF has been described in 3 papers. The first provides the theory of linear KFs and EKFs. The second gives the theory of battery modeling. SOC is a state in the model, which means its value is given as well as its uncertainty. Knowing the uncertainty gives a user a precise range of remaining charge. Many different models are investigated and evaluated based on RMS error under various temperatures. Adding hysteresis to the models increased accuracy at the cost of increased computational power required. The third paper outlines the primary applications of EKF to the estimation requirements for battery management. The discrete time state space model takes on the form

$$\begin{aligned} SOC_{k+1} &= e^{-\phi \cdot t_{eff}} SOC_k + w_k \\ y_k &= OCV(SOC_k) + v_k \end{aligned}$$

where t_{off} is the time that the battery is at rest. The model is tested using a pulse test and by applying the Urban Dynamometer Driving Schedule (UDDS). The EKF always demonstrates convergence. A dual EKF is introduced whereby states and parameters are estimated separately with the outcome of updating parameters as the cell ages. SOC estimation error is found to be less than or equal to 5% in the temperature range 0-50°C. Future work should include the evaluation of the dual EKF state space model at negative ambient temperatures [62],[63],[64].

An adaptive digital filter for lithium-ion battery SOC estimation has been presented. A first order Randle equivalent circuit LPV model is used. It is incorrectly assumed that age and temperature do not affect the OCV-SOC curve. A least squares algorithm recursively identifies model parameters [65].

A Thevenin equivalent circuit has been modified to estimate SOC. The input is terminal voltage, which is then transformed into state space with other parameters to account for nonlinearities. It demonstrates the ability to predict SOC but would become more inaccurate under high currents, changes in temperature, or cell degradation. The model presented is intended for lead-acid batteries and may not be appropriate for lithium-ion batteries. Also, real-time results are not attainable [67].

Impedance measurements have been combined with fuzzy logic inference. An equivalent circuit is fitted to the EIS data in order to extract parameters. Error is high at 10%, meaning that the model chosen does not appropriately demonstrate the battery dynamics. When fuzzy logic is combined with coulomb counting the error is reduced to 5%. Lithium-ion type batteries and temperatures other than room temperature are not investigated [70].

4.4 Patent Review

Several patents have been evaluated [74-109]. The majority of patents were assigned by GM Global Technologies, Inc, with Nissan Motor Co., Ltd. and Panasonic EV Energy Co., Ltd. tied for second most. The OCV method accounts for nearly two-thirds of the patent market share. Not all are written for lithium-ion polymer type batteries; however, many concepts still apply. It may be noted that many patents have basic ideas in common with only minor differentiation between documentation. For the sake of the reader, each patent was summarized separately.

A method has been presented wherein OCV is used to estimate SOC when there is no external current flow and coulomb counting is used when there is a load. This concept is similar to ordinary coulomb counting only it has many recalibration points, rather than just fully charged or fully discharged. The error depends on battery rest intervals; the longer the period of use between long rests, the greater the accumulated error. Many lookup tables to account for different ambient temperatures would have to be stored in memory. SOC determined from OVC is not calculated by linear interpolation, but rather by a curve-fit equation. Q_{max} is updated periodically by means of cycling the battery. A predictive OCV equation is discussed that determines remaining run time based on OCV and estimated overpotentials [74].

The accuracy of SOC estimation has been increased by updating Q_{max} by monitoring a battery's internal resistance during discharge. It is said to be a linear relationship [75].

It has been suggested to use OCV under no load and coulomb counting with multiple current sensors under load. Three different current sensors are averaged to provide one SOC number. Each sensor takes readings at a different frequency, with sensor accuracy decreasing as its frequency increased [76].

A concept has been introduced in which OCV is used to estimate SOC when there is no load on the battery. Multiple OCV curves are stored in lookup tables for multiple ambient temperatures. Coulomb counting is used when there was a load on the battery. An equation for Q_{max} as a function of cycle number is determined from experimental data. The updated Q_{max} is then used to update SOC during coulomb counting [77].

An equivalent circuit model has been used to extract battery parameters. Terminal voltage and current are input into model equations to determine the double layer voltage (V_{dl}), which is then correlated to OCV and consequently SOC [78].

A SOC estimation algorithm has been developed in which OCV, coulomb counting, and transient response are weighted and then averaged. Component weights are calculated as the integral of each change with SOC. The transient response, or dominant pole position, is found to change significantly with SOC when compared to OCV so it is given a relatively larger weight [79].

Magnetic response has estimated SOC. A battery is wound externally with wires in which current was passed creating a magnetic field. That magnetic field induces a second magnetic field within the battery. A resultant magnetic field is sensed as the difference between the first and the second. The resultant field, or change of attractive force, is found to be linearly proportional to the SOC in the range 10-100% [80]. The same authors have an almost identical earlier patent, only it combined magnetic response detection with coulomb counting. Weight factors are given to each based on the change in Ah [90].

SOC has been estimated by the application of a constant voltage for a specified length of time. The battery must be in equilibrium before beginning, making this concept unrealistic. The resulting current is measured and correlated to a previously generated lookup table [81].

An electrochemical model has been used to estimate lithium concentration diffusion in the electrode active material. Based on the voltage and temperature, physics-based equations express the SOC. Concentration is correlated to OCV, once all overpotentials were removed by calculation, and diffusion limitations are accounted for. The model is comprised of a few separate estimation units including diffusion, OCV, and current density. Current density relies on terminal voltage measurements while concentration distribution and OCV are purely mathematical estimates. All are generated from the mathematical equations described earlier. Great accuracy is achieved at the cost of great required computation power [82].

An OCV method has been divulged in which the relationship between voltage and current is plotted, with current as the x-axis and voltage as the y-axis. The point where the trend line crosses the voltage axis is considered to be the OCV. That value is then correlated to a stored OCV-SOC lookup table. This method does not consider different ambient temperatures or battery aging [83].

A hybrid OCV/coulomb counting method has been presented where both are used simultaneously. Rest is defined as a specified period of time where the external current equal to or less than a preset value. The SOC estimations from both methods are assigned weights depending on how well the rest condition is met. Theoretically, the OCV method should periodically recalibrate the SOC ascertained from coulomb counting, yet the drawbacks of each during loading are not eliminated [84].

A multi-step state vector approach has been developed. First, a time interval for which the battery has been at rest is determined. Previous state vectors are recalled from memory. A second state vector is predicted based on the previous history and rest time. Once the battery starts to charge/discharge a terminal voltage measurement, or first state vector, is obtained. A second terminal voltage is estimated based on the predicted second state vector. A voltage error value is calculated as the difference between the first and second terminal voltage values. Then a third state vector is estimated based on the second predicted state vector and the voltage error value [85]. The same author has an earlier patent in which an EKF is fitted to an electrochemical model with temperature taken into consideration. SOC is an internal system state so the uncertainty of estimation is an output. The work follows the author’s journal articles mentioned previously. The estimation algorithm would require significant computational power [100].

Similar to [83], a battery's *V-I* relationship has been plotted during charging and discharging. The point where the trend line crosses the voltage axis is assumed to be the OCV. That OCV is then correlated to a SOC in a previously generated lookup table [86].

An OCV method has been introduced that reduces errors from hysteresis. An SOC range is specified as the range in which corrections need to be made based on hysteresis being so influential there, such as 20-80%. A stored map of correction factors based on current and temperature is to be kept in memory. If the SOC, or corresponding OCV, range is within the range specified then a correction factor is applied in order to provide a more accurate SOC [87].

A patent has been suggested whereby terminal voltages *V1* and *V2* are measured at times *T1* and *T2*. Measurements are taken during rest periods making this method inaccurate during charging or discharging. Voltages are then plotted versus the inverses of the square roots of the times. The linear relationship is extrapolated to find the voltage axis intersection value, which is assumed to be the OCV. SOC is estimated based on the OCV. This method could be used to estimate OCV after a load has been removed but before equilibrium is reached; however, it is not applicable in dynamic loading situations [88].

A coulomb counting method has been pioneered in which there are two current sensors. The first has a measurement range that covers the expected continuous current range. It is located inside a junction box connected directly to a battery. The second is a sensor that detects motor/generator current based on a motor control signal. It is located inside a DC/DC converter. When the current range of the first sensor is exceeded, the second is used thereby increasing accuracy [89].

SOC has been estimated from temperature, current, and voltage measurements. Within the hysteresis a range of voltages and SOCs are defined. SOC is then calculated based on the average SOCs and voltages with a given equation. Lithium-ion batteries do not exhibit strong hysteresis making this method not applicable [91]. The same author holds another patent in which OCV estimated SOC. Charge/discharge swings are predefined to meet current flow and duration requirements. If a charge swing is followed by a discharge swing, or vice versa, then the measured terminal voltage is said to be equal to OCV. Also, OCV will be used when the battery has been at rest longer than a predetermined time [95].

A SOC estimation technique has been presented in which a straight-line approximation using a least squares recursive method is used to find the voltage intercept in a *V-I* plot from experimental data. Voltage and current are measured. The change in Ah is a function of the change in terminal voltage with variable associated adjustment coefficients, change in electromotive force constant, and polarization voltage generation constant based on the physical properties of the battery [92]. The same inventors have another patent that employs the OCV technique. Once a battery is disconnected from a load, terminal voltage is measured and a stored polarization voltage from a lookup table is subtracted from it. The calculation gave OCV which was then linked to a SOC. When there is external current, a no-load voltage is determined by straight-line regression analysis from terminal voltage and current measurements. Coulomb counting kept track of Ah charged or discharged. A polarization voltage is calculated based on the Ah charged or discharged. Then the polarization voltage is subtracted from the no-load voltage to obtain OCV. It is stated that this method is not practical since it takes about a month for all polarization effects to leave a cell once it is disconnected [96].

An OCV method has been adduced whereby OCV is plotted and an equation fitted to the terminal voltage measurements as it relaxes after a charge or discharge. The equation is also a function of age, temperature, and approximate SOC. Each equation is based on 20 hours of data.

Every time the external current flow to a battery is interrupted one of the predetermined equations could be used to estimate the steady-state voltage, or OCV, which is then correlated to SOC [93].

It has been alleged that coulomb counting performs more accurately under constant current conditions, so that is when it is used; otherwise OCV. An adaptive digital filter with a battery model determines OCV from terminal voltage and current measurements. Even though the current may be constant, the current sensor errors will continue to accumulate [94].

SOC has been estimated by the voltage drop measured as the difference between the terminal voltage when charging and the terminal voltage afterward at equilibrium. A plurality of these values is stored in memory. This method does not consider that impedance of a cell will change as it ages. Also, it will not be accurate under high current rates such as those seen in HEVs/EVs [97].

An equivalent circuit has been patented in which voltage, current, and temperature are continuously input. Depending on the operating point of the battery, state and parameter variables are corrected with weighting factors. The values are then used to estimate OCV, and therefore SOC. The equations basically combined OCV with coulomb counting, weighting each depending on the current load. No considerations are made for temperature or aging [98].

Pulsed loads have been applied to a battery to obtain SOC. Current is passed from the battery through a known resistive load while the terminal voltage was measured. The measured voltage is then compared to a stored lookup discharge voltage profile and a SOC is deduced. The voltage profile will change as the battery ages or under different temperatures making this technique invalid [99].

A patent has exemplified use of an EKF with a state vector model. The EKF uses the measured terminal current to predict terminal voltage. A difference is calculated between the predicted and measured terminal voltages, which are then used to correct the state variables. Ambient temperature and charging/discharging efficiency are included. The technique is very computationally intensive [101]. The same inventors have another patent that combines coulomb counting and OCV techniques. A weighted average is taken to determine the SOC. The voltage-based SOC is based on a modified Nernst equation while the Ah-based SOC is based on simple coulomb counting. The weights are derived by piecewise functions based on how the terminal voltage changes with SOC as a function of time [102].

A battery's current limits have been used to estimate SOC. Voltage and current measurements are taken at two different times while the battery is under load. A trend line is drawn between those points on a V-I plot. The minimum voltage is identified on the plot and a line drawn. The intersection of the trend line and V_{min} is noted. A line is then drawn from the intersection to the current axis depicting I_{limit}. I_{min} is specified by the battery manufacturer. Remaining charge is calculated as the difference of I_{limit} and I_{min} divided by the maximum limiting current slope. The V-I plots will change with aging and temperature [103].

A coulomb counting method with efficiency factors has been presented. The charging efficiency factor is a function of measured and maximum applied current while the discharging efficiency factor is a function of Ah removed under standard and present operation conditions. These values are stored in multiple lookup tables with different temperatures being accounted for. A user must know SOC, temperature, and current to get an appropriate efficiency factor. These tables will change as the battery ages; for example, efficiencies will drop [104].

A multi-step approach with a pseudo-SOC has been patented. Coulomb counting is used initially to give a pseudo-SOC. An OCV is estimated based on the pseudo-SOC. Terminal voltage is measured and the overpotentials are removed by physics-based equations. The estimated and calculated OCVs are compared and assigned a correction factor from previously generated lookup tables. The correction factor tables will need to be periodically updated to account for battery degradation [105]. Similarly, a patent has been presented in which coulomb counting error is reduced with a correction factor, although the deterioration in Q_{max} is periodically updated by fully cycling the battery [107].

The Peukert equation has been used to calculate Q_{max}, of the form $Q_{\max} = I^k t$ where k is the Peukert constant. Coulomb counting measures the Ah charged or discharged with the use of two current sensors. One takes samples very often while the other takes samples occasionally. A weighted average is computed and input into the coulomb counting SOC estimation equation [106].

SOC has been estimated based on internal resistance from terminal voltage measurements during a disconnected state. When current is applied, the *R* and *I* measurements are referenced to a previously generated *R-I* plot with various curves representing different SOCs. A temperature correction is applied in order to standardize the effects of temperature. Cell resistance will increase as the battery ages, so the *R-I* curves will have to be updated [108].

An OCV concept has been described wherein terminal voltage measurement values are converted to OCV values with current measurements and a stored internal resistance value, which can be decremented with cycling. Basically, ohmic overpotentials are removed from the terminal voltage measurements. It remains unclear how the internal resistance value will be accurately decremented [109].

Summary pie charts shown in Figure 14 depict the percentages of patents (2008-present) by assignee (left, blue) and by method (right, green).

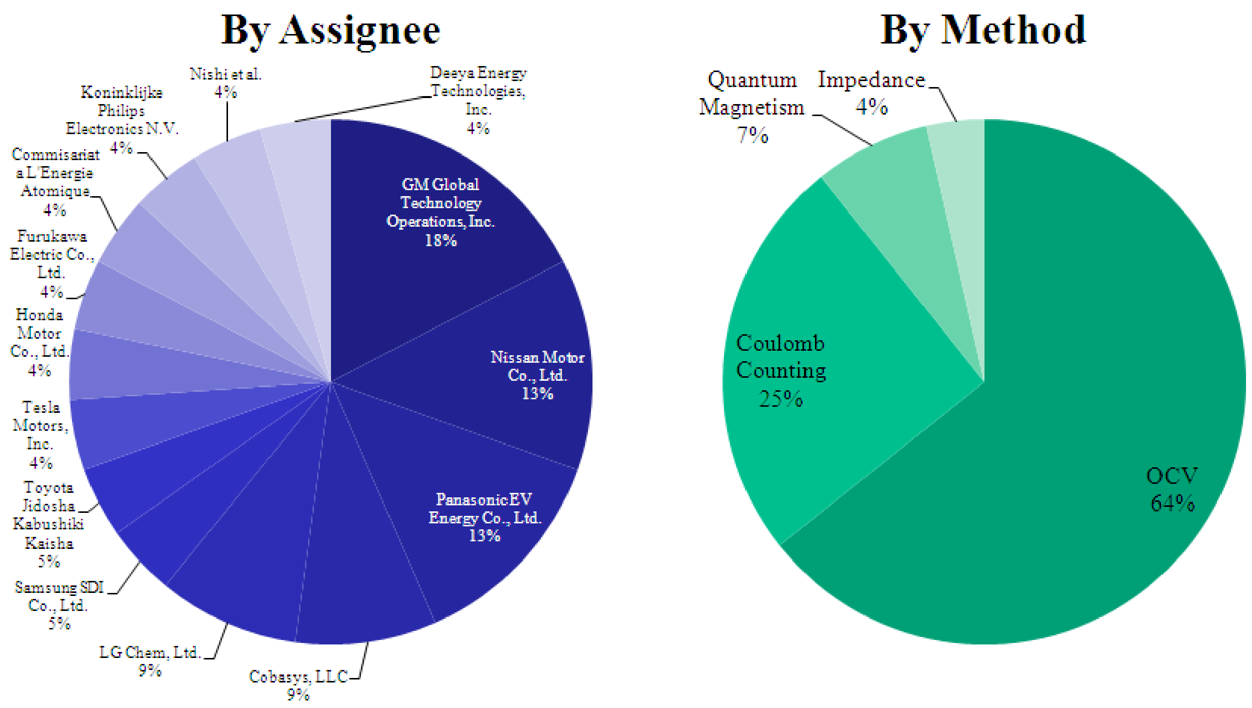

Figure 14: Patent categorization

4.5 Summary

A tree diagram may be seen in Appendix 1 that gives an overall view of all existing SOC estimation methods. The methods have dark backgrounds while the principle author(s) have white backgrounds. The diagram illustrates commonalities between literatures reviewed and categorizes all journal articles, conference papers, and patents into those with and those without a mathematical model. Then subcategories provide further categorization. The majority of literature employs a model. Table 1 provides an overview of the advantages and drawbacks to all existing SOC estimation methods.

Table 1: Advantages and drawbacks of existing SOC estimation techniques

Technique		**Advantages**	**Drawbacks**
Coulomb counting		• Easy implementation • Low cost	• Measurement errors accumulate • Requires periodic re-calibration • Unable to estimate initial SOC • Self-discharge not accounted for
OCV	No model	• Easy implementation • Low cost	• Battery must be at electrochemical equilibrium
	Equivalent circuit model	• Simple to construct RC circuit • Relatively low computational power required	• Unable to describe physical cell limitations or heat generation rate • Model parameters are temperature, current, and age dependent
	Thermal electrochemical model	• Describes physical cell limitations and heat generation rate • Order may be reduced to decrease computation time	• Relatively high computational power required
Impedance		• Provides insight into dynamics of multiple internal components	• Highly temperature, current, and age sensitive • Requires constant AC amplitude

Not a single article or patent reviewed documents ECM or ROM results at any ambient temperature other than 25°C or room temperature, nor does any reflect the effects of higher C-rates or duration of loading on SOC estimation. Also, none provide data for efficiency coefficient calculations and non have used the OCV curve as a “true” value. Rather, coulomb counting is used with a high-precision CT which maintains the flaw of error accumulation.

In fact, only one paper describes a concept of correcting coulomb counting errors with a model [34], in which the difference between an ECM terminal voltage estimate and the measured terminal voltage are multiplied by an integral gain and subtracted from the coulomb counting SOC estimate. Basically, it regulates the model output voltage at the value of the actual measured voltage. This concept must rely on coulomb counting history for initial SOC and does not account for CT measurement error accumulation. The authors assume a high-precision CT to be the “true” value. It also does not account for various ambient temperatures, various C-rates, or loading for longer than a single discharge. There exist many SOC estimation concepts, but none have proven the ability to retain great accuracy in the gamut of realistic operating conditions.

Chapter 5: Experimental Setup

The author designed and constructed several battery test stations at Auburn University capable of charging/discharging a battery with any desired current profile and ambient temperature.

5.1 Test Equipment

A LEM IT 400-S high performance current transducer (CT) was used to measure current. It has a range of 0-400A and rated accuracy of 0.0044% and is comparable to what might be found inside a HEV/EV. The CT transforms the current signal passing through it to a much smaller current at a ratio of 2000:1. A 2.5Ω precision resistor with a tolerance of 0.01% was connected across the smaller current carrying wires and a voltage was recorded across the resistor in order to determine current a battery was experiencing. The conversion factor from measured voltage to battery current remained constant, even under variations in ambient temperature of ±5°C. AC and DC signals may be recorded. The CT was calibrated through the use of an Agilent 34410A digital multimeter with an associated accuracy of 0.17mV and a Tektronix AM503B current probe with an associated error of <0.2%. A V-I characteristic plot was generated by recording voltage from the CT with the multimeter and current of the wire traveling through the CT with the current probe. The data was then input into the LabVIEW calibration software, for the voltage range -0.5 to 0.5V, where it was saved for all future measurements. The voltage range selected corresponds to approximately -130 to 130A, which covers the maximum current of 5C (78.5A). Figure 15 shows that there was negligible error between the CT manufacturer's V-I plot and the experimental V-I plot.

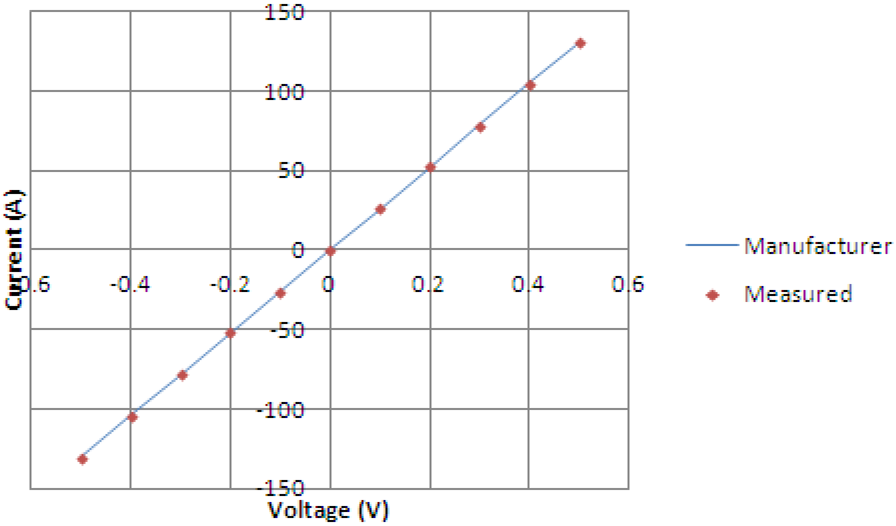

Figure 15: CT V-I calibration plot

The sample rate for single cycle tests was 10Hz while that for longer term tests was 1Hz in order to conserve computer memory. A summary of power supply and electronic load specifications is given in Table 2. All tests in this thesis were conducted with a Sorensen DCS 8-125E power supply and a Kikusui PLZ1004W electronic load.

Table 2: High-power test equipment

Type	**Model**	**Rated Voltage (V)**	**Rated Current (A)**
Power Supply	Sorensen DCS 8-125E	0-8	0-125
Electronic Load	Kikusui PLZ1004W	1.5-150	0-200

Ambient temperature was manipulated by a Thermotron 8200 with a Watlow Series 922 microprocessor-based ramping control. This unit allows experiments to be conducted in the temperature range -70°C to 150°C, which covers the realistic range a HEV/EV will experience. Ambient temperature was recorded using an Omega K-type thermocouple with an associated uncertainty of measurement of 0.1%. The thermocouple was calibrated in the temperature range of -50°C to 100°C using an Omega Ice Point Calibration Reference Chamber capable of maintaining a constant temperature of 0°C.

Terminal voltage measurements are taken directly from the battery terminal tabs using dedicated short, twisted wires so as to minimize voltage drop. Terminal voltage measurement was calibrated using an Agilent 34410A digital multimeter with an accuracy of 0.17mV.

A test station wiring diagram is shown in Figure 16. Figure 17 shows a photograph of the test station. The equipment is organized within a metal rack with one shelf for the computer, one for the electronic load, one for the power supply, and one for the data acquisition board, with the computer peripherals on top. This compact design allowed for optimum use of space within the laboratory and improved the ease of transportation.

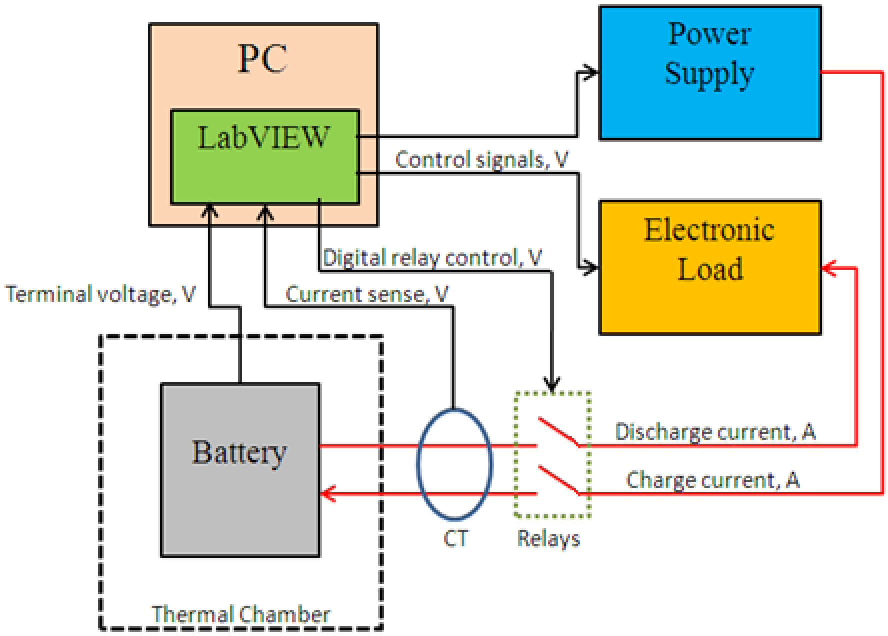

Figure 16: Test station wiring diagram

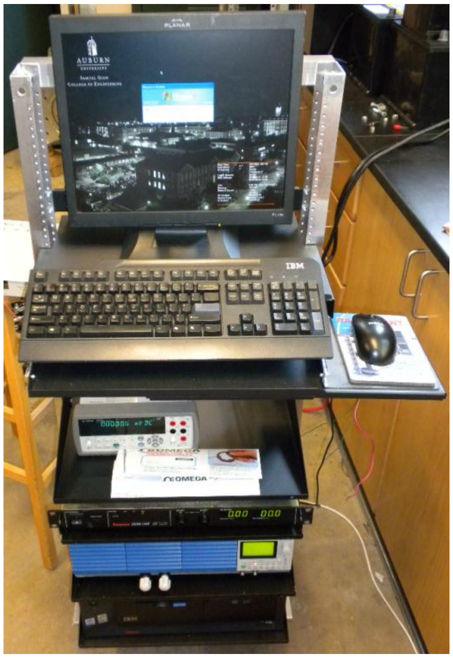

Figure 17: Test station photograph

5.2 Software Programming

National Instruments LabVIEW software allows a user to define a program. National Instruments PCI cards, connector blocks, and modules allow a user to output analog or digital voltage control signals while recording input measurement voltage signals.

A screenshot showing the front control panel of a program is shown in Figure 18, followed by a screenshot of the discharge current control section of the rear block diagram in Figure 19. The easily manipulated controls may be placed on the front panel at user’s discretion. All block diagrams have the same basic sequence structure: initialization, accept input, produce output, repeat until a stop condition is met, then clear input and close.

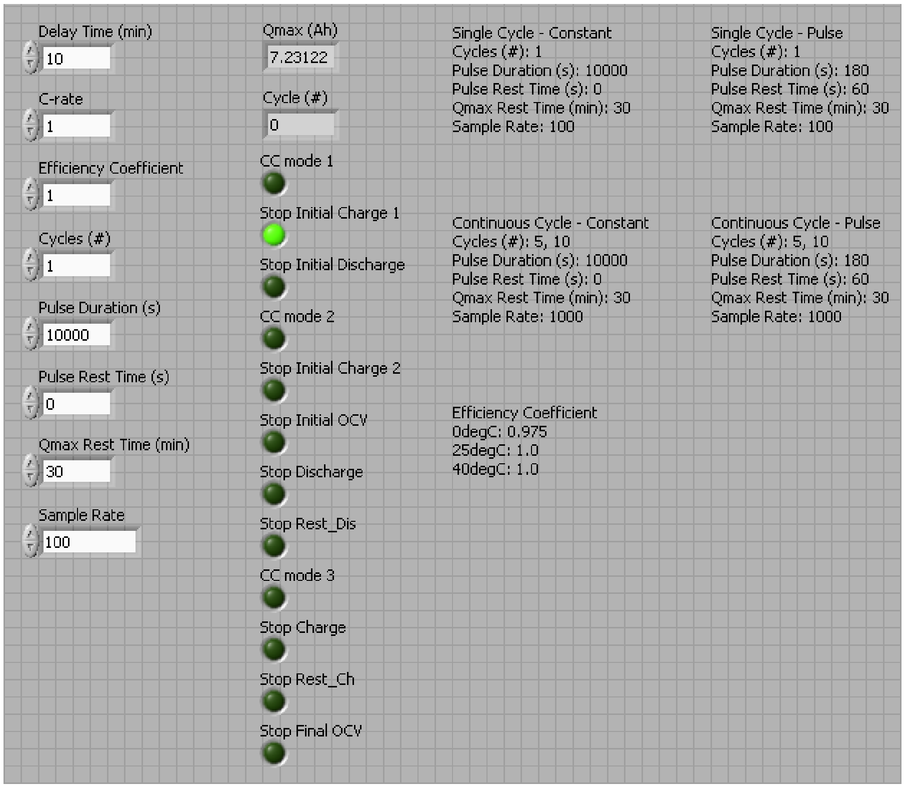

Delay Time (min)
10

C-rate
1

Efficiency Coefficient
1

Cycles (#)
1

Pulse Duration (s)
10000

Pulse Rest Time (s)
0

Qmax Rest Time (min)
30

Sample Rate
100

Qmax (Ah)
7.23122

Cycle (#)
0

Single Cycle - Constant
Cycles (#): 1
Pulse Duration (s): 10000
Pulse Rest Time (s): 0
Qmax Rest Time (min): 30
Sample Rate: 100

Single Cycle - Pulse
Cycles (#): 1
Pulse Duration (s): 180
Pulse Rest Time (s): 60
Qmax Rest Time (min): 30
Sample Rate: 100

Continuous Cycle - Constant
Cycles (#): 5, 10
Pulse Duration (s): 10000
Pulse Rest Time (s): 0
Qmax Rest Time (min): 30
Sample Rate: 1000

Continuous Cycle - Pulse
Cycles (#): 5, 10
Pulse Duration (s): 180
Pulse Rest Time (s): 60
Qmax Rest Time (min): 30
Sample Rate: 1000

Efficiency Coefficient
0degC: 0.975
25degC: 1.0
40degC: 1.0

Figure 18: LabVIEW front panel screenshot

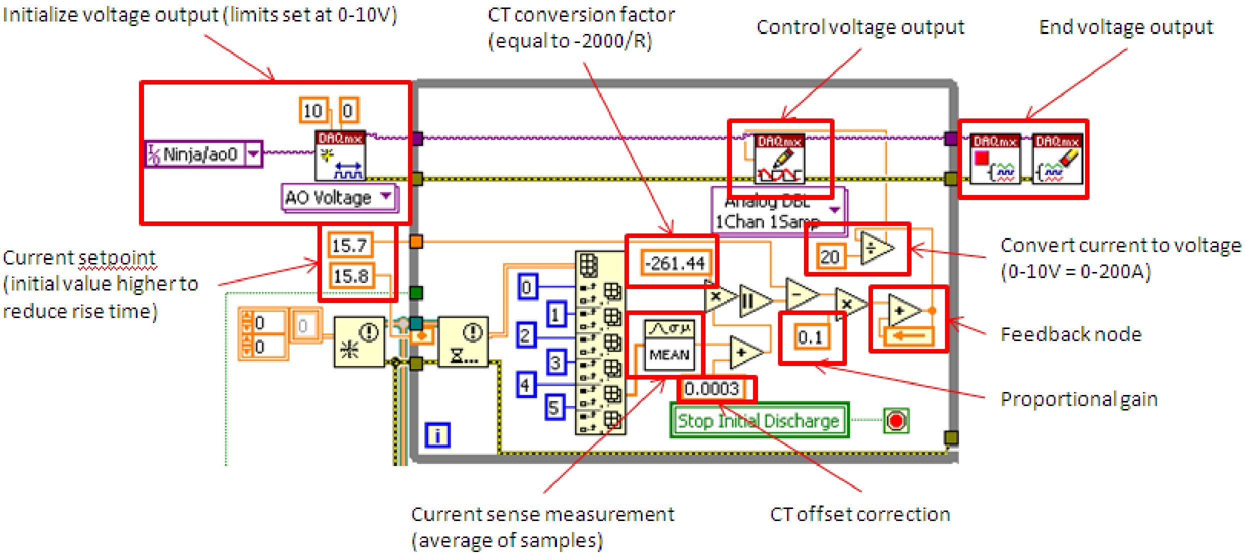

Initialize voltage output (limits set at 0-10V)

CT conversion factor (equal to -2000/R)

Control voltage output

End voltage output

Current setpoint (initial value higher to reduce rise time)

Convert current to voltage (0-10V = 0-200A)

Feedback node

Proportional gain

Current sense measurement (average of samples)

CT offset correction

Figure 19: LabVIEW current control block diagram

Feedback control of the sink current is continuously optimized based on CT readings to match the current setpoint. The loop ceased to iterate once a preset stop condition, such as V_{min}, is reached. Any desired current profile may be programmed.

Data is recorded in TDMS format which can be read in Excel after downloading a TDMS Importer add-in. Figure 20 shows a block diagram of the data recording section of a LabVIEW program.

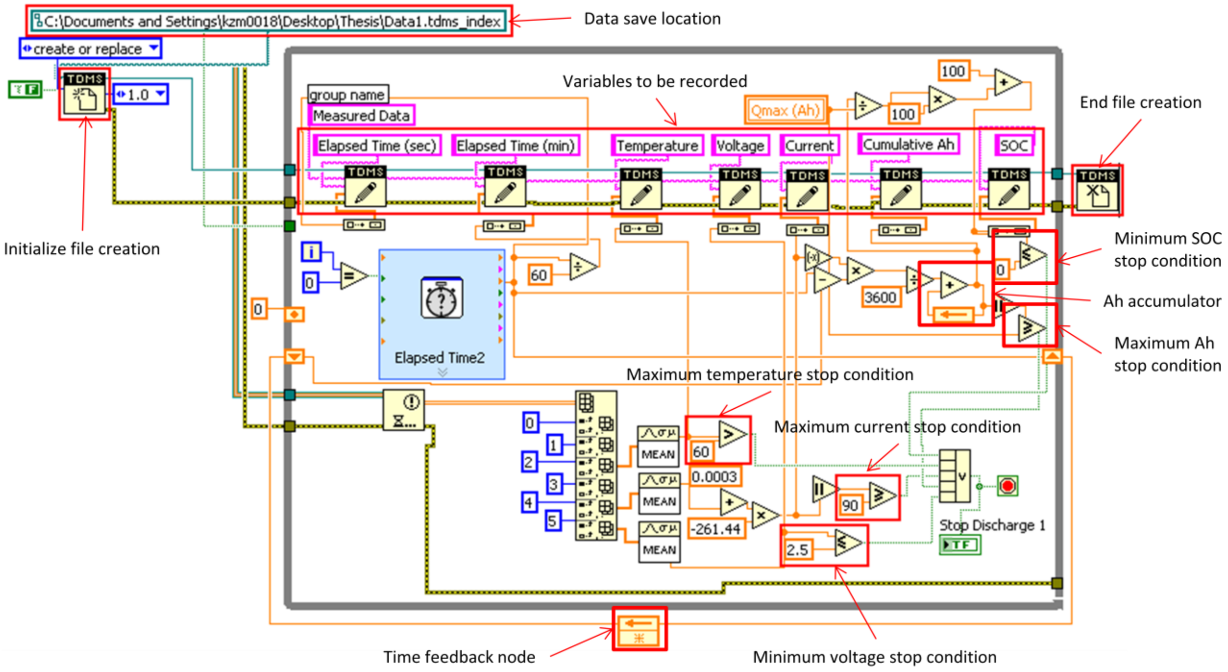

Figure 20: LabVIEW data recording block diagram

5.3 Li-Polymer Battery Specifications

The batteries being used for experimental validation are pouch type with a cathode consisting of a mixture of manganese, nickel, and cobalt oxides. Each has a nominal capacity of 15.7Ah. Their maximum temperature allowable before thermal runaway occurs is 75°C. Due to a confidentiality agreement with the supplier, no additional information will be given.

All cells are initially fully discharged and then fully charged 5 times before any testing. This is to provide adequate charge transfer for the SEI layer to stabilize. If not stable, Q_{max} may vary significantly between cycles. For the specific battery being investigated, a full charge is defined as reaching 4.15V at 1C in CC mode then reaching the cutoff current of 800mA in CV mode. A full discharge is defined as reaching 2.5V at 1C.

The fundamentals presented in Chapter 2 will now be applied. This section offers a detailed description of how the ECM, FOM, and ROM are formulated.

6.1 Minimum Rest Time

A standard rest time of 30 minutes was adapted for all experiments based on battery relaxation characteristics. Figure 21 depicts unfiltered terminal voltage relaxation after a 5 minute 1C charge at 25°C with an arbitrary initial SOC. Rest time is practically identical for other C-rates and ambient temperatures.

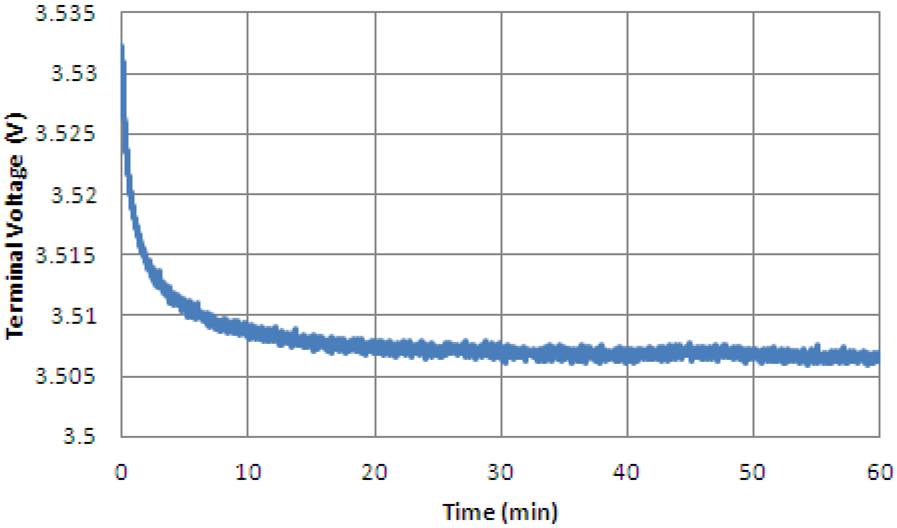

Figure 21: Terminal voltage relaxation

The OCV method remains an accurate SOC estimation technique for a battery at electrochemical equilibrium. A minimum time to reach equilibrium may be determined from studying the battery's voltage relaxation characteristics; the shorter the required rest time, the more coulomb counting re-calibration opportunities. An allowable SOC change rate may differ between OEMs, but the author might suggest a target of ≤0.01% SOC per minute. Based on the voltage relaxation plot as shown in Figure 22, terminal voltage changes by ≤0.072mV per minute, or ≤0.01% SOC per minute, after 18 minutes. Figure 22 is a zoomed-in image of Figure 21 with a low-pass filter applied. Every time a HEV or EV rests its battery pack for at least 18 minutes then the accumulated time (*t*) should be reset to zero and a terminal voltage measurement could be used to estimate SOC based on the OCV curve. The figure proves that 30 minutes per rest period is more than sufficient.

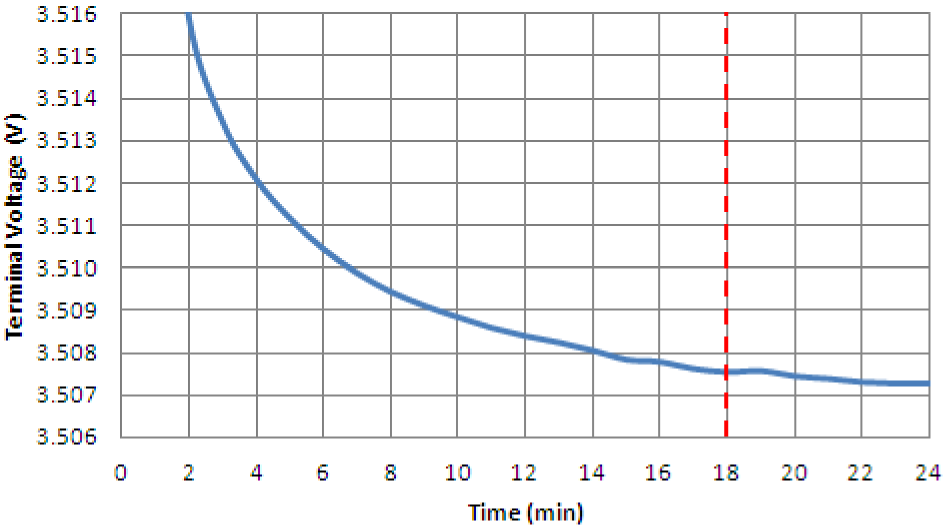

Figure 22: Minimum rest time

6.2 OCV Curve

A fully charged battery was discharged at a 1C-rate for 30 seconds and then rested for 30 minutes while T_{amb} remains a constant 25°C. This process was repeated until the terminal voltage reached the manufacturer's V_{min} of 2.5V. After 30 minutes, terminal voltage changes by less than 1mV per 10 minutes corresponding to less than 0.014% SOC per minute so it was deemed an appropriate rest time.

The discharge duration of 30 seconds was chosen in order to provide approximately 120 data points. The measured voltage at the end of a 30 minute rest, before load was applied, is considered to be equal to OCV since it is considered ample time for the cell to reach chemical equilibrium. A sample of the terminal voltage profile undergoing OCV discharge pulses is shown in Figure 23. The rest periods between pulses are not shown.

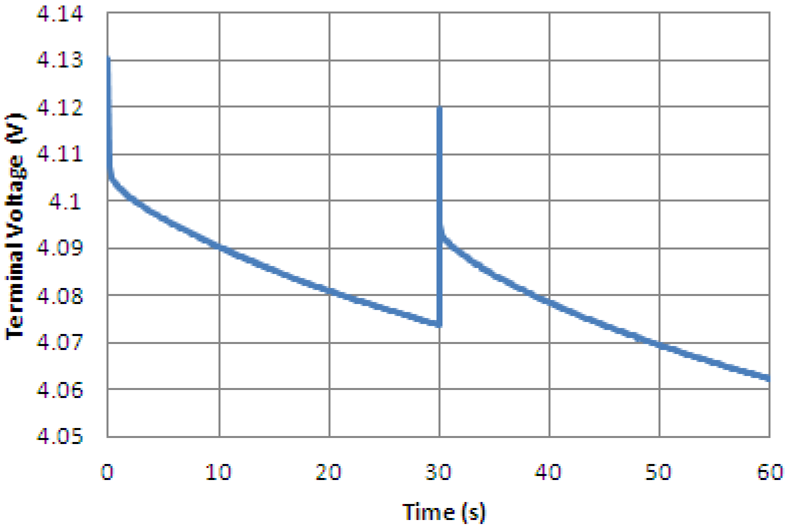

Figure 23: OCV generator pulse sample

Current was measured and integrated during the discharges. The coulomb counting method was applied with an initial SOC of 100% and a Q_{max} measured experimentally beforehand. CT measurement errors are assumed to be negligible due to the short load times and rest periods between each data point. OCVs and SOCs were then linked to generate Figure 24.

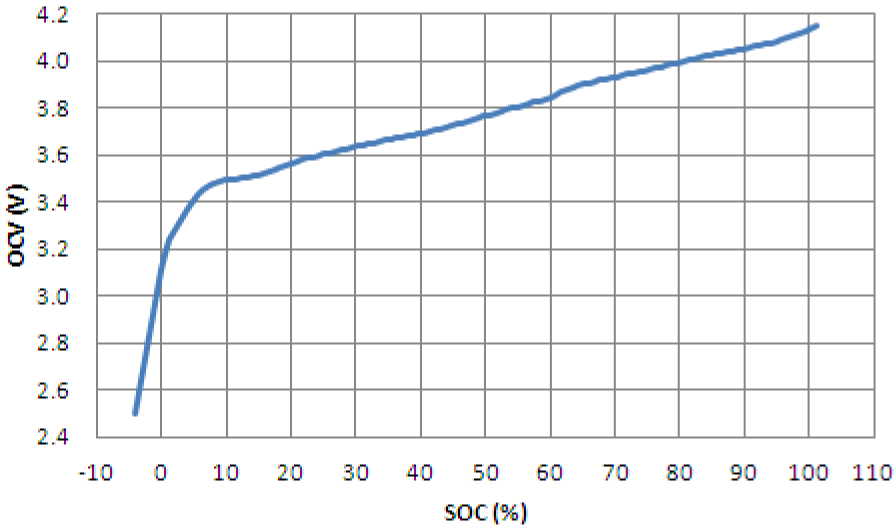

Figure 24: OCV curve

SOCs corresponding to the battery's V_{max} and V_{min} were interpolated. That is why the chart has values below 0% SOC and above 100% SOC.

The effect of T_{amb} on terminal voltage after a full discharge at 1C can be seen in Figure 25.

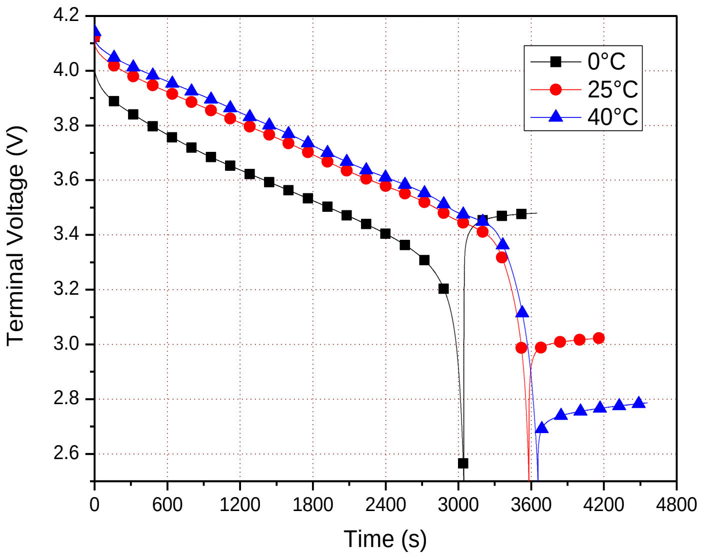

Figure 25: Effect of T_{amb} on 1C full discharge

The OCV curve standard is 25°C; therefore, if the same OCV curve is applied at 0°C the SOC will be underestimated and at 40°C overestimated. Table 3 shows the SOC correction factors at 0% SOC. These values are considered to be the “true, calibrated” values to which all calculations of error will be based.

Table 3: SOC T_{amb} correction factors

	0°C	**25°C**	**40°C**
Final terminal voltage	3.4798	3.0233	2.7864
Final SOC	7.94	-0.58	-2.08
Correction factor at 0%	+8.52	N/A	-1.50

6.3 Equivalent Circuit Model (ECM)

6.3.1 RC Circuit

A second order Randle model is the most common equivalent circuit model in literature [3],[4],[8],[13],[17], [19], [34], [43], [51],[65], [70], [98]. With its 3 resistors and 2 capacitors it is able to accurately portray battery dynamics. First and third order models were attempted, with poor results. The components include ohmic resistance (R_1), electrochemical polarization resistance (R_2), concentration polarization resistance (R_3), electrochemical polarization capacitance (C_2), and concentration polarization capacitance (C_3) [3], as can be seen in Figure 26.

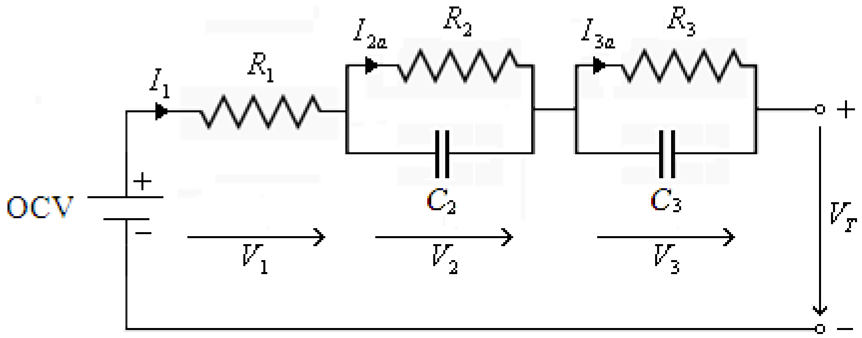

Figure 26: ECM RC circuit

OCV is equal to the sum of the other voltages, given by $OCV = I_1 R_1 + I_{2a} R_2 + I_{3a} R_3 + V_T$ where the currents are those flowing across the resistors.

$I_{2a} = \frac{V_2}{R_2}$ and the current across the capacitor *C*C_2 is given by $I_{2b} = C_2 \frac{dV_2}{dt} = I_1 - I_{2a} = I_1 - \frac{V_2}{R_2}$. This simplifies to $\frac{dV_2}{dt} + \frac{V_2}{R_2 C_2} = \frac{I_1}{C_2}$. With the boundary conditions of $V_2(0) = 0$ and $V_2(\infty) = I_1 R_2$, the solution becomes $V_2(t) = I_1 R_2 (1 - e^{\frac{-t}{R_2 C_2}})$. When the approach is applied to all components in the circuit the solution becomes $OCV = I_1 [R_1 + R_2 (1 - e^{\frac{-t}{R_2 C_2}}) + R_3 (1 - e^{\frac{-t}{R_3 C_3}})] + V_T$. The estimated OCV is then input to a lookup table to estimate SOC.

6.3.2 Parameter Extraction

To determine to correct values for R_1, R_2, R_3, C_2, and C_3 a series of pulses were applied to a battery to measure dynamic response. Current and terminal voltage are measured during 1C, 1 minute discharges with subsequent 30 minute rest periods. A single pulse depicting terminal voltage change is shown in Figure 27.

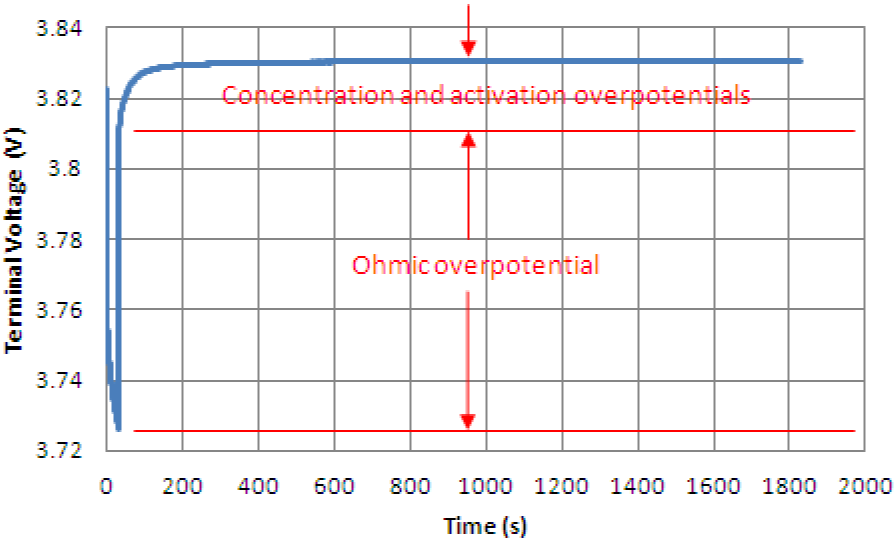

Figure 27: ECM parameter extraction pulse

The immediate voltage change after current interruption is equal to the ohmic overpotential (V_1) since it does not include a capacitor that would slow voltage relaxation. V1 is divided the current, 15.7A, to extract R_1, according to Ohm’s law. The remaining voltage change after the initial change until the end of rest is equal to the concentration and activation overpotentials ($V_2 + V_3$). The MATLAB curve fitting tool was implemented using a nonlinear least squares exponential equation of the form “a*exp(b*x)+c*exp(d*x)” since that matches the form of $V_2(t)$ and $V_3(t)$ determined previously. Figure 28 shows an example curve fitting, in which the blue dots are data points and the red line is the curve fit.

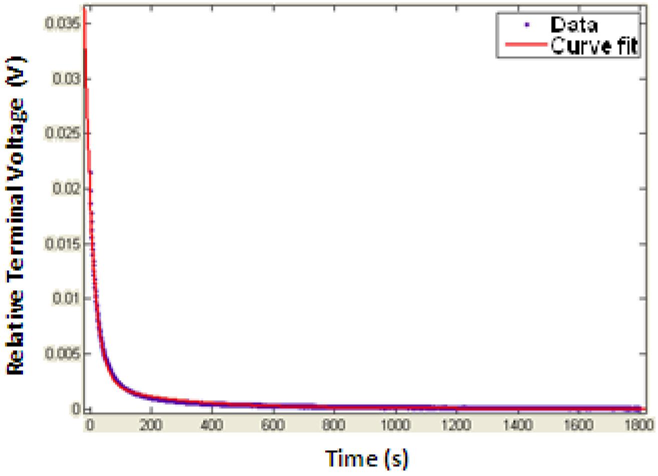

Figure 28: Curve fitting example

The data from multiple separate discharge pulses were averaged, with an average R-squared value above 0.99, to provide final values, as seen in Table 4.

Table 4: ECM extracted parameters

Parameter	**Value @ 0°C**	**Value @ 25°C**	**Value @ 40°C**
R1	0.010613	0.005752	0.002181
R2	0.001772	0.001149	0.000653
R3	0.000214	0.000154	0.000173
C2	32860.11	22777.05	71809.62
C3	4318320	2237890	8202080

The parameters vary appreciably with T_{amb}. They are also expected to vary between cells considering minute manufacturing difference as well as with age as material degradation leads to internal resistance increases.

6.4 Full Order Thermal Electrochemical Model (FOM)

The model for electrodes is built based on the theory that it consists of multiple spherical particles, as shown in Figure 29

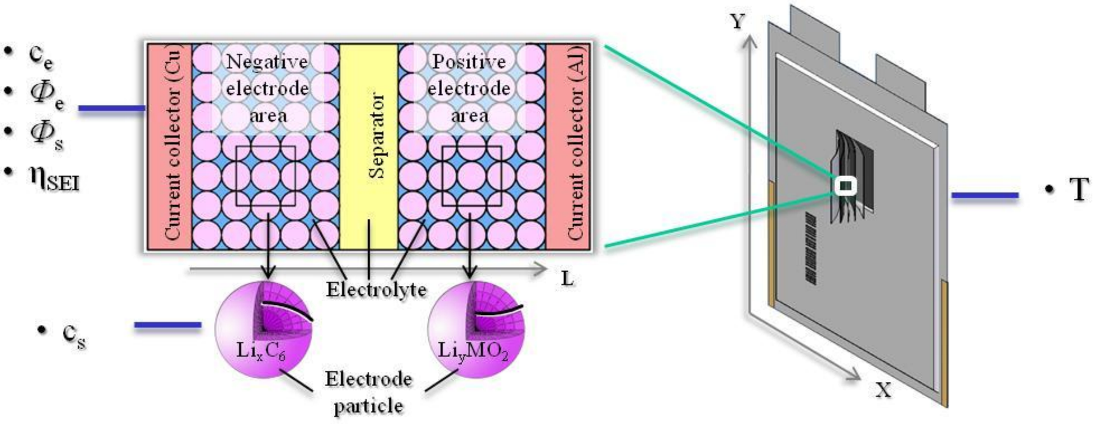

Figure 29: Electrochemical model schematic [9]

where lithium-ion concentration, c_s, in a single particle is described by Fick's law of diffusion

$$\frac{\partial c_s}{\partial t} = \frac{D_s}{r^2}\frac{\partial}{\partial r}\left(r^2\frac{\partial c_s}{\partial r}\right) \tag{1}$$

with boundary conditions

$$\left.\frac{\partial c_s}{\partial r}\right|_{r=0} = 0 \text{ and } D_s\left.\frac{\partial c_s}{\partial r}\right|_{r=R_s} = \frac{-j^{Li}}{a_s F} \tag{2}$$

where r is the radius of electrode particle, R_s is the maximum electrode particle radius, a_s is the interfacial surface area, and F is the Faraday constant.

Distribution of ion concentrations in the electrolyte can be described by

$$\frac{\partial(\varepsilon_e c_e)}{\partial t} = \frac{\partial}{\partial x}\left(D_e^{eff}\frac{\partial}{\partial x}c_e\right) + \frac{1-t_+^0}{F}j^{Li} \tag{3}$$

with boundary conditions

$$\left.\frac{\partial c_e}{\partial t}\right|_{x=0} = \left.\frac{\partial c_e}{\partial t}\right|_{x=L} = 0 \tag{4}$$

where L is the thickness of the microcell, c_e is the lithium-ion concentration in the electrolyte phase, ε_e is the porosity, $t_+{}^0$ is the transference number, and $D_e{}^{eff}$ is the effective diffusion coefficient calculated using the equation

$$D_e^{eff} = D_e \cdot \varepsilon_e^p \tag{5}$$

The governing equation of potential is based on the principle of charge conservation derived from Ohm’s law

$$\frac{\partial}{\partial x}\left(\sigma^{eff} \frac{\partial}{\partial x}\phi_s\right) - j^{Li} = 0 \tag{6}$$

with boundary conditions

$$\sigma^{eff} \frac{\partial}{\partial x}\phi_s\bigg|_{x=\delta-} = \sigma^{eff} \frac{\partial}{\partial x}\phi_s\bigg|_{x=\delta+} = \frac{I}{A} \tag{7}$$

$$\frac{\partial}{\partial x}\phi_s\bigg|_{x=0} = \frac{\partial}{\partial x}\phi_s\bigg|_{x=L} = 0 \tag{8}$$

where δ^- is the thickness of the anode (cm) and δ^+ is the thickness of the cathode (cm).

Charge conservation in the electrolyte yields

$$\frac{\partial}{\partial x}\left(k^{eff} \frac{\partial}{\partial x}\phi_e\right) + \frac{\partial}{\partial x}\left(k_D^{eff} \frac{\partial}{\partial x}\ln c_e\right) + j^{Li} = 0 \tag{9}$$

with boundary conditions

$$\frac{\partial}{\partial x}\phi_e\bigg|_{x=0} = \frac{\partial}{\partial x}\phi_e\bigg|_{x=L} = 0 \tag{10}$$

Current density is obtained from the Butler-Volmer electrochemical kinetic equation

$$j^{Li} = a_s i_0 \left\{\exp\left[\frac{\alpha_a F}{RT}\eta\right] - \exp\left[\frac{\alpha_c F}{RT}\eta\right]\right\} \tag{11}$$

where η is the overpotential, defined as the difference between the solid and electrolyte potential minus the equilibrium potential

$$\eta = \phi_s - \phi_e - U \tag{12}$$

Figure 30 depicts the calculation scheme for a single cell model. Governing equations in the microcells are interconnected with a single cell.

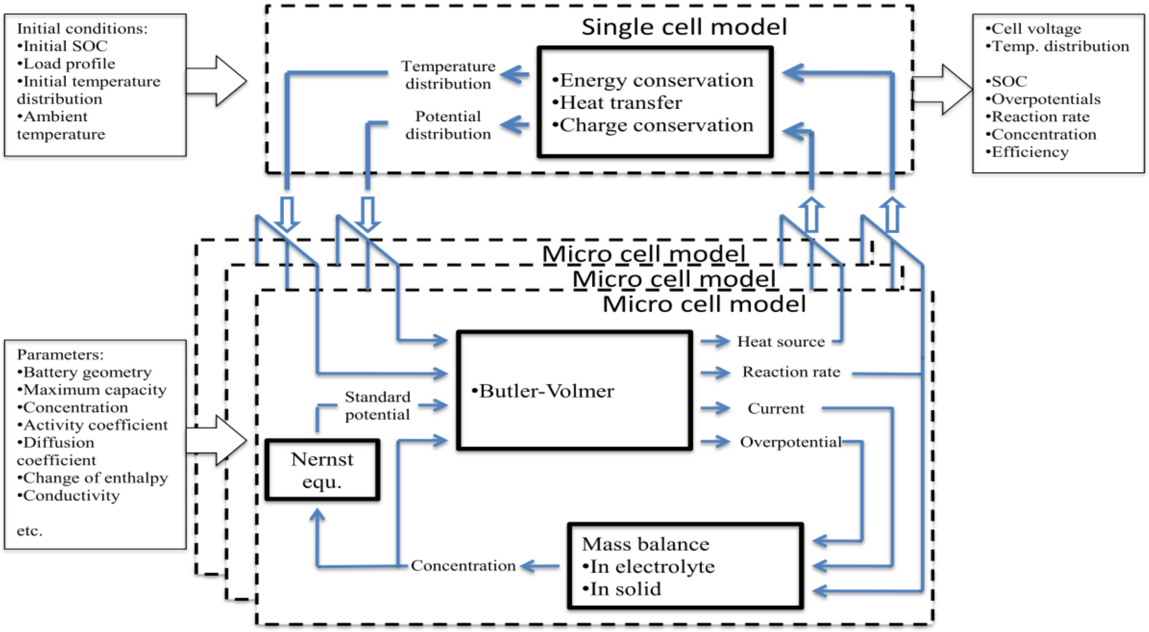

Figure 30: Electrochemical model calculation scheme [9]

All the PDEs are discretized by finite difference methods, implicit method in the time domain and Crank-Nicolson method in the space domain. The implicit method is unconditionally stable and first order accurate while the Crank-Nicolson method is stable although oscillatory and is second order accurate. Nonlinear terms are linearized by Taylor series expansion. The model is solved in discretized state space form. Model parameters may be found in Appendix 2.

6.5 Reduced Order Thermal Electrochemical Model (ROM)

The equations above are PDEs and functions of three variables: *x*, *r*, and *t* that represent the location of a particle along the thickness of an electrode, the radial coordinate within a particle, and time, respectively. PDEs can be solved numerically by discretization. When the domain is discretized with 100 nodes in the *x*-direction and 50 nodes in the *r*-direction, the total number of differential algebraic equations becomes 100×50.

According to the suggestion made by V. Subramanian et al. [20], ion concentration PDEs in the solid electrodes can be replaced with a polynomial under the assumption that ion concentrations inside the spherical particles are a function of the radius of the sphere

$$c_s(r,t) = a(t) + b(t)\cdot\left(\frac{r^2}{R_s^2}\right) + d(t)\cdot\left(\frac{r^4}{R_s^4}\right) \tag{13}$$

where the coefficients, *a*(t), *b*(t), and *d*(t) are a function of time.

The coefficients are solved using $c_{s,ave}$, volume-averaged concentration fluxes (q_{ave}), and surface concentrations ($c_{s,surf}$), given by

$$\begin{aligned} a(t) &= \frac{39}{4}c_{s,surf} - 3q_{ave}R_s - \frac{35}{4}c_{s,ave} \\ b(t) &= -35c_{s,surf} + 10q_{ave}R_s + 35c_{s,ave} \\ c(t) &= \frac{105}{4}c_{s,surf} - 7q_{ave}R_s - \frac{105}{4}c_{s,ave} \end{aligned} \tag{14}$$

where the volume-averaged concentration, volume-averaged concentration flux, and surface concentration are defined as

$$\begin{aligned} c_{s,ave} &= \int_0^{R_s} \frac{3r^2}{R_s^3} c_s(r,t)\,dr \\ q_{ave} &= \int_0^{R_s} \frac{3r^2}{R_s^3}\left(\frac{\partial}{\partial r}c_s(r,t)\right)dr \\ c_{s,surf}(r,t) &= a(t) + b(t)\cdot\left(\frac{r^2}{R_s^2}\right) + d(t)\cdot\left(\frac{r^4}{R_s^4}\right) \end{aligned} \tag{15}$$

By combination with Fick’s law and the boundary conditions, the three above equations become

$$\begin{aligned}
&\frac{d}{dt}c_{s,ave}+3\frac{j^{Li}}{R_s a_s F}=0\\
&\frac{d}{dt}q_{ave}+30\frac{D_s}{R_s^2}q_{ave}+\frac{45}{2}\frac{j^{Li}}{R_s^2 a_s F}=0 \qquad (16)\\
&35\frac{D_s}{R_s}(c_{s,surf}-c_{s,ave})-8D_s q_{ave}=-\frac{j^{Li}}{a_s F}
\end{aligned}$$

Thus, the ion concentration in equation (1) is completely replaced by equations (14), (15), and (16).

The equations above for the potentials are further simplified under following assumptions:

1. Reaction current is not influenced by the electrolyte concentration

$$\frac{\partial}{\partial x}\left(k_D^{eff}\frac{\partial}{\partial x}\ln c_e\right)=0 \qquad (17)$$

2. The Butler-Volmer equation may be linearized

$$j^{Li}=\frac{a_s i_0 F}{RT}(\phi_{se}-U) \qquad (18)$$

3. Ion conductivity (k^{eff}) is constant

$$\frac{\partial}{\partial x}\left(k^{eff}\frac{\partial}{\partial x}\phi_e\right)=k^{eff}\frac{\partial}{\partial x}\left(\frac{\partial}{\partial x}\phi_e\right) \qquad (19)$$

The phase potential difference, ϕ_{se}, is defined as

$$\phi_{se}=\phi_s-\phi_e \qquad (20)$$

So, the potential equations (6) and (9) can then be simplified in the following manner

$$\frac{\partial}{\partial x}\left(k^{eff}\frac{\partial}{\partial x}\phi_e\right)+\frac{\partial}{\partial x}\left(k_D^{eff}\frac{\partial}{\partial x}\ln c_e\right)+j^{Li}=0=\frac{\partial}{\partial x}\left(k^{eff}\frac{\partial}{\partial x}\phi_e\right)+j^{Li} \;\rightarrow\; -\frac{\partial}{\partial x}\left(\frac{\partial}{\partial x}\phi_e\right)-\frac{j^{Li}}{k^{eff}}=0$$

$$\frac{\partial}{\partial x}\left(\sigma^{eff}\frac{\partial}{\partial x}\phi_s\right)-j^{Li}=0 \;\rightarrow\; \frac{\partial}{\partial x}\left(\frac{\partial}{\partial x}\phi_s\right)-\frac{j^{Li}}{\sigma^{eff}}=0$$

$$\therefore \frac{\partial}{\partial x}\left(\frac{\partial}{\partial x}\phi_{se}\right) = j^{Li}\left(\frac{1}{\sigma^{eff}} + \frac{1}{k^{eff}}\right) \tag{21}$$

The capacity of a cell can be expressed as a function of lithium-ion concentration in the electrodes as

$$Q_{releasable} = \int_0^{\delta^-} \varepsilon_s F c_{s,ave} A dx - \varepsilon_s F c_{s,\max} \cdot S_0 A \delta^- \tag{22}$$

$$Q_{\max} = \varepsilon_s F c_{s,\max} \cdot (S_{100} - S_0) A \delta^- \tag{23}$$

where ε_s is the active material volume fraction. The first term in equation (22) can be understood as the average lithium-ion concentration integrated across the anode thickness. It has units of coulombs and only considers the active material. The second term in equation (22) accounts for the charges remaining in the cell at 0% SOC, which cannot be released. Equation (23) is similar only S_{100} is included rather than an integral to account for releasable charges at 100% SOC.

SOC can be expressed as a ratio of the average lithium concentration to the maximum lithium concentration in the negative electrode, calculated as

$$SOC = \frac{Q_{releasable}}{Q_{\max}} = \frac{\int_0^{\delta^-} \varepsilon_s F c_{s,ave} A dx - \varepsilon_s F c_{s,\max} \cdot S_0 A \delta^-}{\varepsilon_s F c_{s,\max} \cdot (S_{100} - S_0) A \delta^-} = \frac{\int_0^{\delta^-} c_{s,ave} dx - c_{s,\max} S_0 \delta^-}{c_{s,\max} (S_{100} - S_0) \delta^-}$$

$$= \frac{\int_0^{\delta^-} c_{s,ave} dx - \int_0^{\delta^-} c_{s,\max} S_0 dx}{c_{s,\max} (S_{100} - S_0) \delta^-} = \frac{\int_0^{\delta^-} \left(c_{s,ave} - c_{s,\max} S_0\right) dx}{c_{s,\max} (S_{100} - S_0) \delta^-}$$

$$SOC = \frac{1}{\delta^-} \int_0^{\delta^-} \frac{\left(c_{s,ave} - c_{s,\max} \cdot S_0\right)}{c_{s,\max} \cdot (S_{100} - S_0)} dx \tag{24}$$

The FOM and ROM PDEs are solved using the same mathematical techniques. Source code will not be presented in this thesis as it is proprietary to Dr. Choe's battery research group at Auburn University.

6.6 Thermal Component of ROM

Heat transfer is described by

$$\rho C_p \frac{\partial T}{\partial t} = \frac{\partial}{\partial x}\left(k_x \frac{\partial T}{\partial x} \right) + \frac{\partial}{\partial y}\left(k_y \frac{\partial T}{\partial y} \right) + \frac{\partial}{\partial z}\left(k_z \frac{\partial T}{\partial z} \right) + Q_{gen} - q$$

where ρ is density (kg·m^{-3}), C_p is specific heat capacity (J·kg^{-1}·K^{-1}), k is thermal conductivity (W·m^{-1}·K^{-1}), Q_{gen} is the heat generation rate per unit volume (W·m^{-3}), and q is the heat transfer rate between the cell and its surroundings (W·m^{-3}) defined by

$$q = \frac{h}{d}(T - T_{amb})$$

where h is the heat transfer coefficient (W·m^{-2}·K^{-1}) and d is the depth of the battery (m).

Q_{gen} includes both reversible and irreversible heat generation and is described by

$$Q_{gen} = I\left(OCV - V_T - T \cdot \frac{\partial OCV}{\partial T} \right)$$

Chapter 7: Existing Method Error Characterization

SOC estimates based on the OCV curve (SOC_{OCV}) are considered the “true” value. Coulomb counting, ECM, and ROM SOC estimation data will be compared to that of the OCV curve after a rest period of at least 30 minutes has passed. Inevitably, this means that real-time dynamic model validation is not possible. Given that the initial SOC is 100%, the final SOC can be inferred by measuring terminal voltage after rest, and the current during discharge is constant, a linear OCV line may be interpolated. The OCV lines at various discharge currents and ambient temperatures then become the basis for error characterization.

A battery is initially fully charged to its V_{max} and I_{cutoff}, which are for these batteries 4.15V and 800mA, respectively. It is then fully discharged to its V_{min} of 2.5V. During the discharge the current is integrated to calculate a unique Q_{max} for that specific battery at a specific T_{amb}. This is a standard procedure for all batteries since Q_{max} is essential to estimate SOC based on the equation

$$SOC(t) = SOC(0) - \frac{\int_0^t \eta \cdot i \cdot dt}{Q_{\max}} \times 100\%$$

The efficiency coefficient, η, is always 1.0 during charge but is a function of T_{amb} during discharge, as seen in Table 5, based on the equation

$$\eta = \frac{Q_{discharge}}{Q_{charge}}$$

At low temperatures reaction kinetics are slowed to a point in which ion migration from the anode to the cathode is decreased due to the reduction of active channels in the polymer separator.

Table 5: Efficiency coefficients

Temperature (°C)	0	25	40
η	0.975	1.0	1.0

These values are expected to change as a battery ages; however, due to the limited number of cycles each battery will experience these values are assumed to be constant.

As a test begins, a battery is fully charged again to 4.15V and 800mA corresponding to an initial SOC of 100%. Then the battery will be cycled a specified number of times while the current is integrated to determine SOC. Full charge is redefined as the condition whereby the charge (Q) is equal to the previously determined Q_{max}, $Q=Q_{max}$. Full discharge is redefined as $Q=0$. After cycling, the battery rests for 30 minutes. Finally, the battery terminal voltage is measured, which is assumed to be OCV at this point. The SOC based on the OCV curve (SOC_{OCV}) is compared to the SOC based on coulomb counting (SOC_{cc}). Recorded current data will be the input for the ECM and ROM models to create model-based SOC estimates (SOC_{model}) enabling comparisons to SOC_{OCV}.

Q_{max} is considered to be accurate even though it employs the coulomb counting technique since the measurement conditions are low current, constant rate, 25°C, and only 1 cycle. Also, Q_{max} is not expected to change by more than 1% during any single test. This was confirmed by conducting 5 cycles on a battery at 1C and 25°C while measuring Q_{max} during each cycle.

7.1 Experimental Test Matrix

Table 6 shows the variables that will be investigated. These have each been proven to affect SOC estimation results. The objective is to determine errors as a function of temperature, current, and time.

Table 6: Proposed investigation range

Current	1, 2, 5C
Mode	Constant, Hybrid Pulse Power Characterization (HPPC)
T_{amb}	0, 25, 40°C
Duration	full discharge, 1 cycle, 5 cycles

For clarification, 1C = 15.7A and the HPPC battery test profile was developed by the U.S. Department of Energy (DOE) at the Idaho National Laboratory [110]. Figure 31 charts the relative current profile.

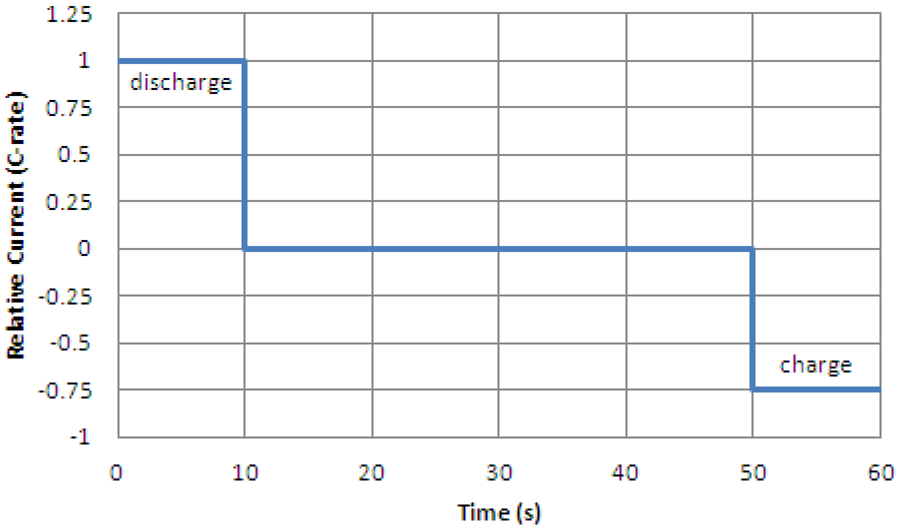

Figure 31: HPPC test profile

It was chosen because it is based on technical targets instituted for energy storage to meet DOE battery performance and life cycle standards. It is applied to a battery for 1 hour so as to not fully discharge a battery. Relative currents utilized are 1C, 2C, and 5C.

In the test matrix context, a “cycle” refers to a discharge followed by a charge in the SOC range 20-80%. These SOCs are calculated by coulomb counting as fractions of the measured Q_{max}. This corresponds to a typical HEV charge sustaining mode SOC range [44]. Appendix 3 contains the complete list of tests conducted. Three batteries were used in total with their roles being rotated for each group of tests so that they each experienced similar times at each T_{amb} so as to not cause uneven degradation.

7.2 Coulomb Counting

As can be seen in Figure 32, coulomb counting error is a linear function of time. These are plots at 1, 2, and 5C at 0, 25, and 40°C. All plots show a linear trend; linear because of constant error accumulation with constant current. Coulomb counting error (σ_{cc}) becomes more positive as T_{amb} increases, where

$$\sigma_{cc} = SOC_{cc} - SOC_{OCV},$$

attributed to the effect of temperature on maximum charge capacity.

Coulomb counting follows

$$SOC(t) = SOC(0) - \frac{\int_0^t \eta \cdot i \cdot dt}{Q_{\max}} \times 100\%$$

where Q_{max} is always measured at a standard 25°C. Q_{max} would be different if the T_{amb} were altered. High temperatures induce greater reaction kinetics, which leads to greater ion migration between V_{max} and V_{min}, and a greater maximum charge capacity. The opposite occurs at low temperatures. Temperature change may be a consequence of internal heat generation due to ion current, too, based on the Butler-Volmer equation. Since Q_{max} and the maximum charge capacity at operating temperature are different, coulomb counting estimates will diverge from OCV curve estimates. This is exemplified in the fact that the coulomb counting SOC estimates at 1C and 25°C had the least error.

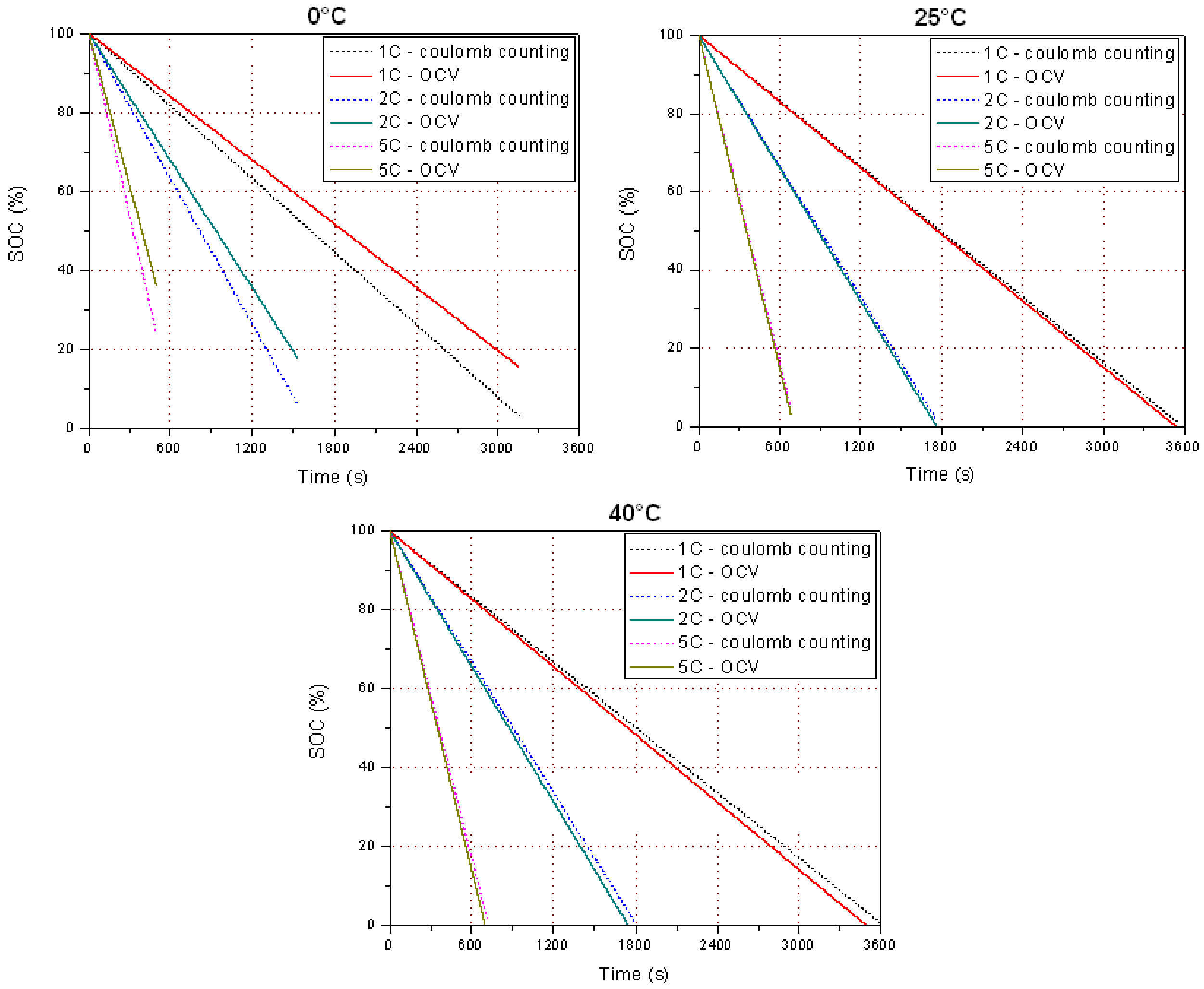

Figure 32: Coulomb counting error characterization

Figure 33 shows the SOC estimation error of coulomb counting when compared to the OCV line. All slopes are linear. The 1C, 25°C line has an error even though the OCV curve was generated by the CT with the same conditions because Q_{max} is slightly different from cell to cell depending on manufacturing tolerances and loading history. Maximum charge capacity is larger for the OCV curve due to its pulsed current profile whereby a battery is given time to rest between load pulses during which its terminal voltage rises. Upon initiation of the succeeding pulse, activation overpotential must be overcome once again to reach the same voltage it was at before which consumes amp-hours falsely included in the SOC calculation. A higher precision

CT would reveal the same flaw since divergence is a function of battery voltage swings relative to T_{amb}.

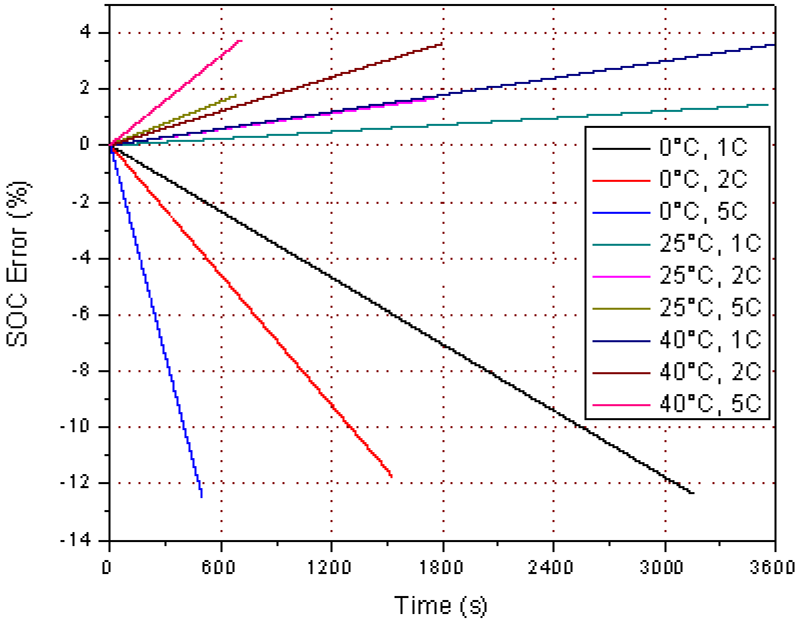

Figure 33: Coulomb counting SOC estimation error summary

7.3 ECM

As can be seen in Figure 34, ECM error (σ_{ECM}) is not a function of time, where

$$\sigma_{ECM} = SOC_{ECM} - SOC_{OCV}$$

where SOC_{ECM} is a function of the ECM-estimated OCV. These are plots at 1, 2, and 5C at 0, 25, and 40°C. Immense error is attributed to model parameters. σ_{ECM} increases significantly with current due to internal heat generation altering the model parameters, which are assumed to be constant. They are very sensitive to variations from cell to cell, age, and temperature. There is no observable trend between σ_{ECM} and T_{amb}.

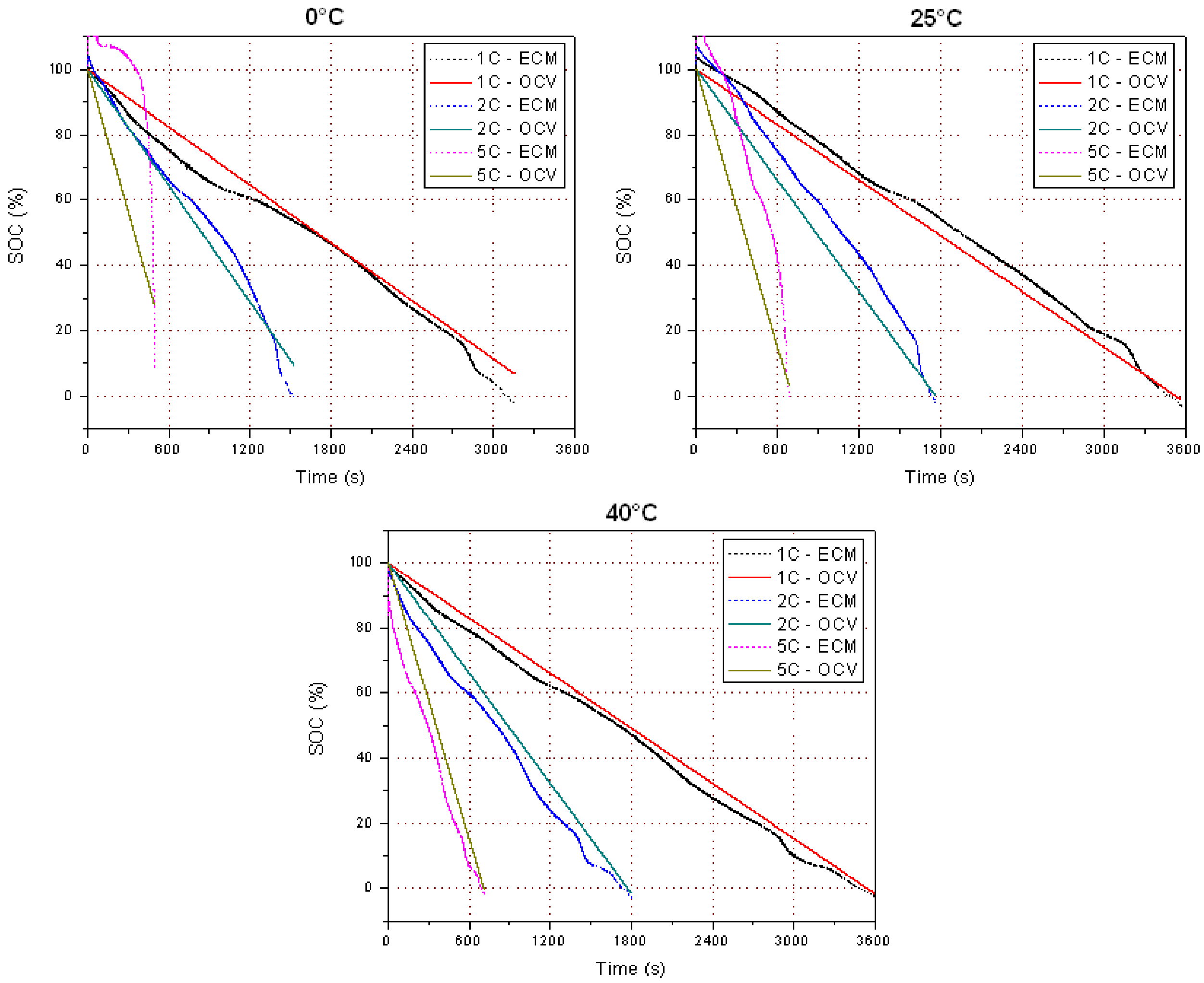

Figure 34: ECM error characterization

7.4 ROM

As can be seen in Figure 35, ROM error (σ_{ROM}) is a function of time, where

$$\sigma_{ROM} = SOC_{ROM} - SOC_{OCV}$$

These are plots at 1, 2, and 5C at 0, 25, and 40°C. σ_{ROM} becomes more positive as T_{amb} increases and is greatest at 0°C. These observations are analogous to those with coulomb counting only the error accumulation is less per time step. The ROM calculates SOC based on

$$SOC = \frac{1}{\delta^-}\int_0^{\delta^-}\frac{\left(c_{s,ave} - c_{s,\max}\cdot S_0\right)}{c_{s,\max}\cdot(S_{100} - S_0)}dx$$

which is based on a standard 25°C.

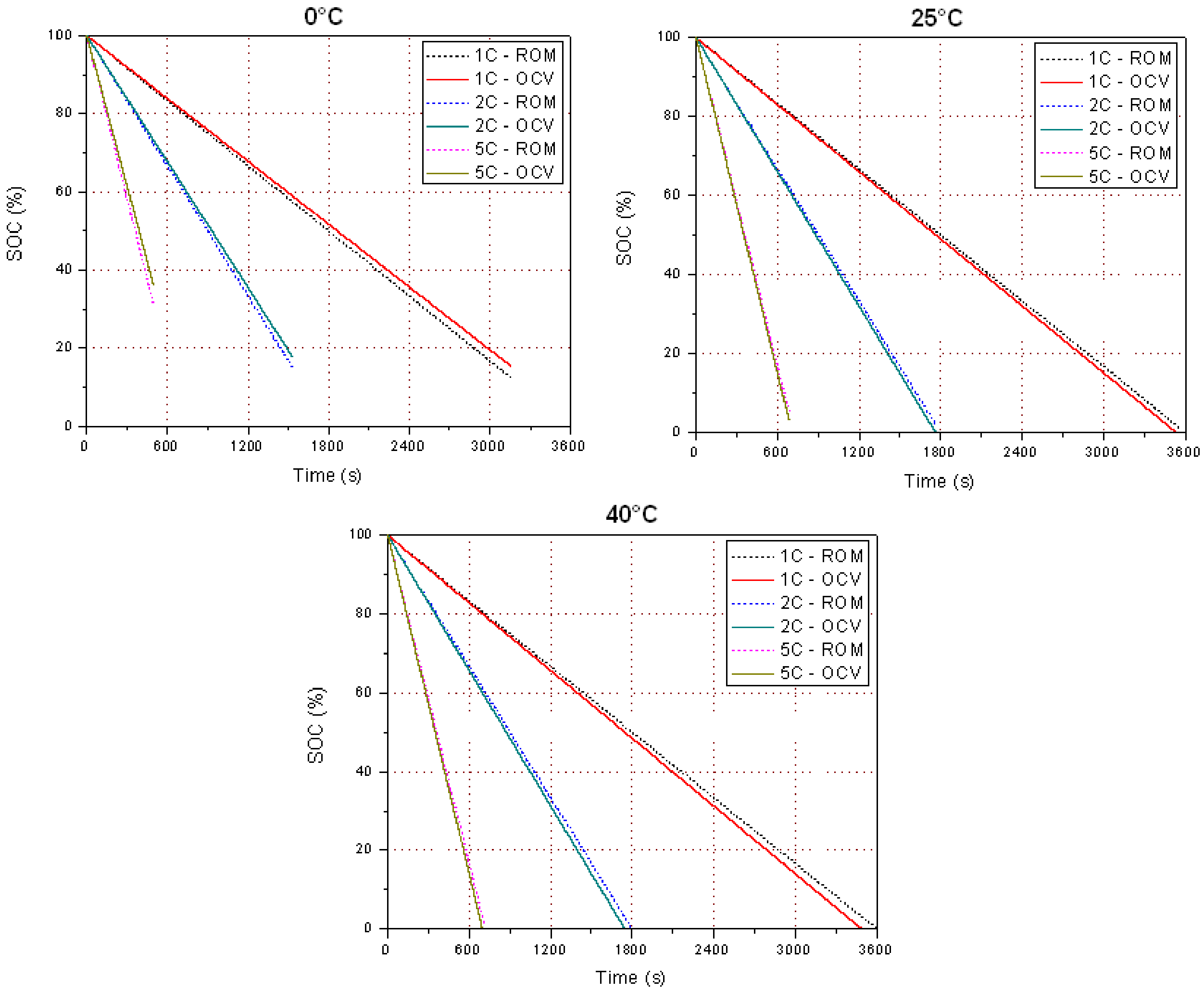

Figure 35: ROM error characterization

Figure 36 shows the SOC estimation error of the ROM when compared to the OCV line. Note that all slopes are linear. There is a small error accumulation with each time step since no model is able to perfectly represent a physical phenomenon. The average anode lithium concentration must be less at low temperatures and greater at high temperatures since it is the only non-constant in the SOC equation. This is typified in the negative slope at 0°C and the positive slopes at 25°C and 40°C. As expected, the discharge at 1C and 25°C had the least average error.

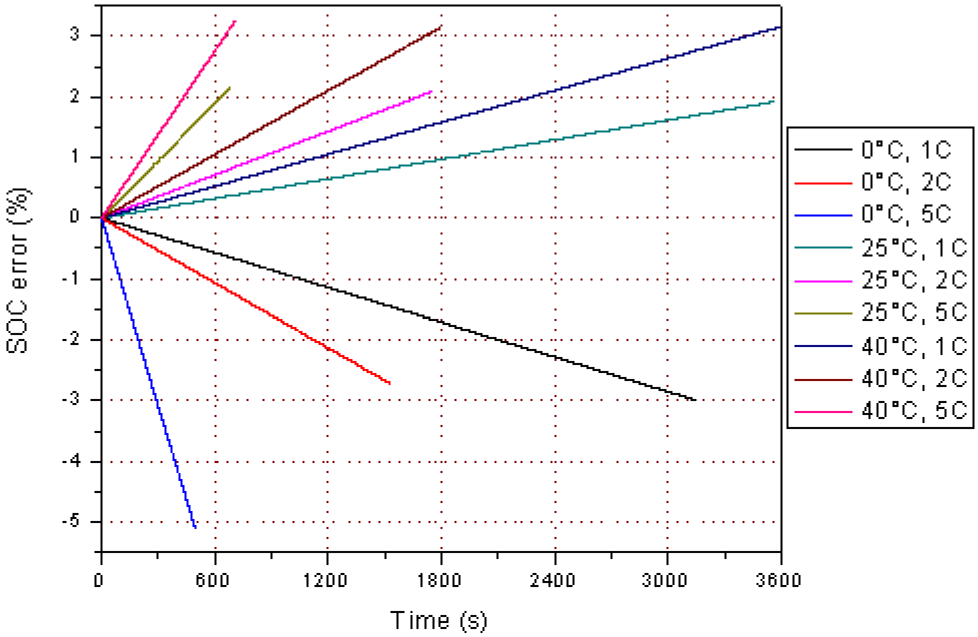

Figure 36: ROM SOC estimation error summary

7.5 Summary

The ROM exhibited less error than coulomb counting in all cases. Coulomb counting offers no connection between measured current and battery internal dynamics. It can provide Ah calculations but cannot relate those to the state of a battery since Q_{max} changes with T_{amb} and age. The ROM can relate current and temperature to SOC by accounting for their effects on lithium concentration in the anode. The model input current can be a setpoint, to eliminate CT measurement error, or simply a CT measurement. If taken as a setpoint, there may be a small initialization error not captured by the model as power equipment takes time to ramp up to a setpoint, however, this is on the scale of <0.1% SOC so it could be neglected. CT measurements were the input for all models in this thesis.

Regardless of the rated accuracy of a CT, there will always exist coulomb counting measurement error that will accumulate with time. From gathered data, it appears that the ROM error also accumulates with time since no model is perfect. Small imperfections accumulate with each time step. Also, the ROM may rely on the CT for current input, adding to the linear error accumulation. External disturbance, such as a strong random magnetic field pulse, may lead to false readings. A higher precision CT may improve SOC estimation but still would be susceptible to the drawbacks previously mentioned.

The ROM also exhibited less error than the ECM in all cases. This is due to the inability of the ECM to describe physical cell limitations, such as maximum/minimum lithium-ion concentration and maximum lithium-ion surface concentration or diffusion rates in the anode, or heat generation rate. Also, its current input is based on an imperfect CT current measurement. Model parameters are highly sensitive to temperature and current. This implies that the parameters would have to be periodically updated and may vary from cell to cell based on age or manufacturing variations. The ROM continuously updates for temperature and current and is capable of including lithium-ion diffusion depletion and saturation limitations.

Even though the ECM calculation time may be 10+ times faster, increasing SOC estimation speed is secondary in this thesis. SOC estimation accuracy augmentation is the primary goal. The ROM calculation time is approximately a factor of 10 less than that for the FOM with no evident difference in SOC estimates. Therefore, only the ROM will be further evaluated for inclusion in a new method.

Chapter 8: SOC Estimation Error Compensation of ROM Using an Empirical Method

A new SOC estimation algorithm is proposed that corrects the error associated with ROM estimates. Theoretically, the linear error accumulation previously documented may be removed by subtracting a constant correction rate term dependent on I and T_{amb}. An algorithm loop has been conceptualized containing a 2D interpolator and an error correction path, as shown in Figure 37, designed to minimize SOC estimation error. The current input is a desired value or setpoint, not a measured value so as to eliminate CT measurement offset error. Terminal voltage input from the battery is used only to set initial SOC.

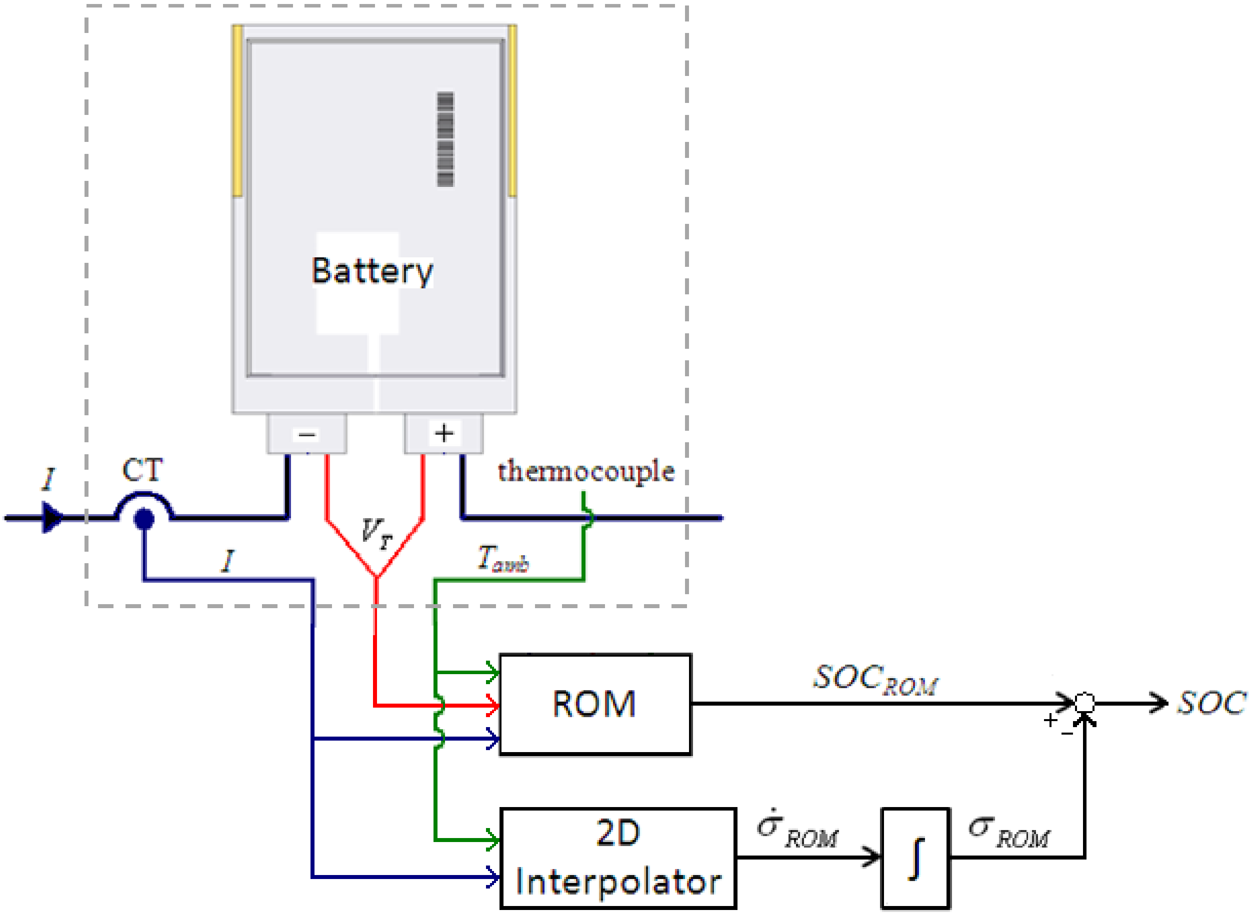

Figure 37: Empirical method schematic block diagram

Combined method concepts using coulomb counting with a model such as a weighted average scheme, a piecewise method with smoothing, and a Kalman filter approach have been evaluated. The mathematically-simplest approach, error characterization and removal, proved to perform well due to the linear nature of the ROM error.

The OCV method remains valid if a battery has been at rest for a specified amount of time. It may only be used to estimate initial and final SOCs if the rest condition has been satisfied.

8.1 ROM Error Rate

ROM error (σ_{ROM}) accumulates linearly with time. It is calculated as

$$\sigma_{ROM} = (SOC_{ROM} - SOC_{OCV})$$

where the SOCs used in the equation are single point values at the end of a full discharge, as shown in Table 7. ROM final SOC error increases with C-rate but not always with T_{amb}.

Table 7: ROM single discharge final SOC errors

Current (C-rate)	**T_{amb} (°C)**	**Final SOC Error (%)**
1	0	-3.00
	25	1.92
	40	3.17
2	0	-2.72
	25	2.10
	40	3.15
5	0	-5.14
	25	2.15
	40	3.27

Since error is a linear function of time due to model imperfections accruing with each time step, a constant discharge error rate ($\dot{\sigma}_{ROM}$) may be calculated as

$$\dot{\sigma}_{ROM} = \frac{\sigma_{ROM}}{t_{total}} = \frac{(SOC_{ROM} - SOC_{OCV})}{t_{total}}$$

where t_{total} is the total discharge time (s) at a specific C-rate and T_{amb}.

Table 8 shows the experimental results for $\dot{\sigma}_{ROM}$. The ROM discharge error rate increases with C-rate. At similar C-rates, the error rate tends to have a maximum value at 0°C and a minimum at 25°C.

Table 8: ROM discharge error rates

Current (C-rate)	**T_{amb} (°C)**	**Error Rate ($\times 10^{-4}$) (%/s)**
1	0	-9.5
	25	5.4
	40	8.8
2	0	-17.8
	25	11.9
	40	17.5
5	0	-103.2
	25	31.4
	40	45.9

Charge error rates were calculated the same way. They differ significantly from discharge error rates. Unfortunately, it is not possible to compare coulomb counting or ROM SOC estimates to the OCV curve during a full charge since it consists of CC and CV modes. SOC does not linearly increase but rather tapers off in CV mode as the applied current decreases. Charge error rate is assumed to be constant during CC and CV modes. Example charge data at 1C and 0°C is shown in Figure 38. Time (*t*) used in error rate calculated is reset to zero whenever current is interrupted or polarity switched.

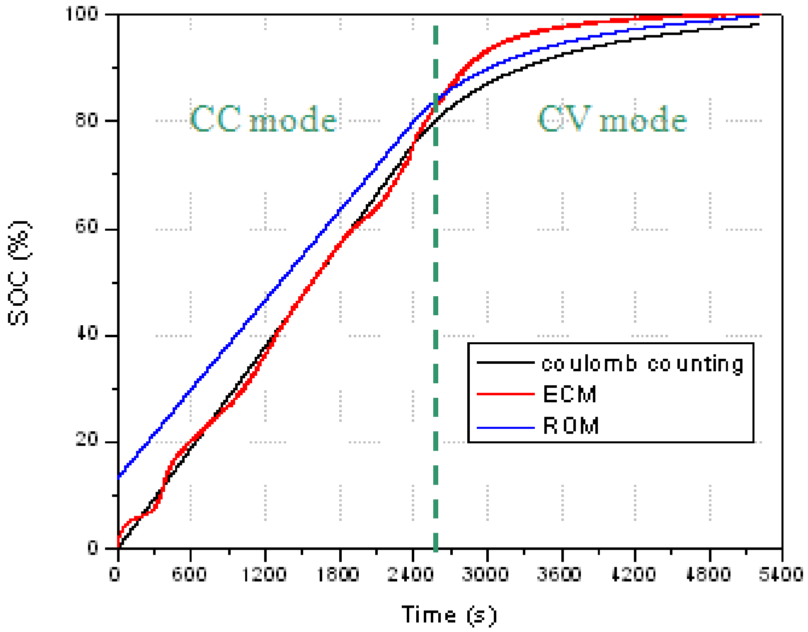

Figure 38: Single charge data at 1C, 0°C

It is also not possible to back-interpolate an OCV SOC estimate from the beginning and end of charge since there is not rest period between discharging and charging phases. Charge error rate results are shown in Table 9. These values were tuned so as to minimize final SOC error after a full charge.

Table 9: ROM charge error rates

Current (C-rate)	T_{amb} **(°C)**	**Error Rate (×10^{-4}) (%/s)**
1	0	5.0
	25	-4.2
	40	-7.7
2	0	7.1
	25	-7.2
	40	-13.0
5	0	79.2
	25	-9.7
	40	-2.3

8.2 2D Interpolation

Rarely will real world operating conditions exactly match a C-rate and T_{amb} evaluated. Interpolation is required to calculate ROM error rates in the C-rate range of 1-5C and the temperature range of 0-40°C.

First, $\dot{\sigma}_{ROM}$ is interpolated as a function of T_{amb}. A 2nd order polynomial method was chosen due to the nonlinear nature of the relationship. $\dot{\sigma}_{ROM}$ as a function of C-rate is nearly linear. Each equation for discharge, which is shown in Figure 39 with dotted lines representing an interpolation curve, has an associated coefficient of determination (R^2) = 1.

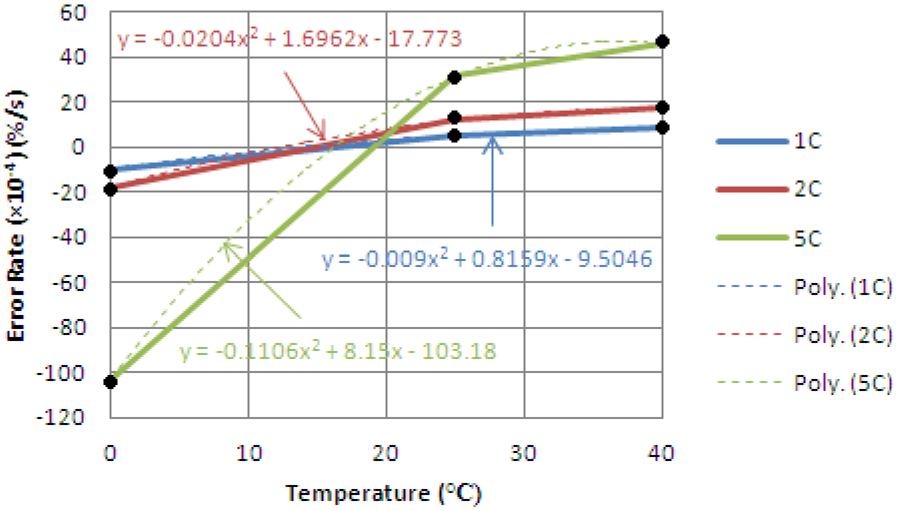

Figure 39: ROM discharge error rate as a function of T_{amb}

The calculated value is then linearly interpolated with respect to C-rate. This process is also applicable to charge error rates. An example calculation for a battery being discharged at 3C and 30°C is provided below:

$$@2C:\dot{\sigma}_{ROM}(T) = -0.0204T^2 + 1.6962T - 17.773 \rightarrow \dot{\sigma}_{ROM}(30) = 14.753\times10^{-4}$$
$$@5C:\dot{\sigma}_{ROM}(T) = -0.1106T^2 + 8.15T - 103.18 \rightarrow \dot{\sigma}_{ROM}(30) = 41.780\times10^{-4}$$

$$\dot{\sigma}_{ROM} = \frac{(3-2)}{(5-2)}\cdot(41.780\times10^{-4} - 14.753\times10^{-4}) + 14.753\times10^{-4} = 23.762\times10^{-4}\ {}^{\%}\!/_{s}$$

8.3 Single Discharge

Error correction is applied to the single discharge data previously shown for the ROM, as portrayed in Figure 40. There is a significant improvement in SOC estimation accuracy in all cases, so much so that any differences between the model with error correction and the OCV line are indiscernible in a plot. The maximum SOC error is < 0.003% under all investigated operating conditions.

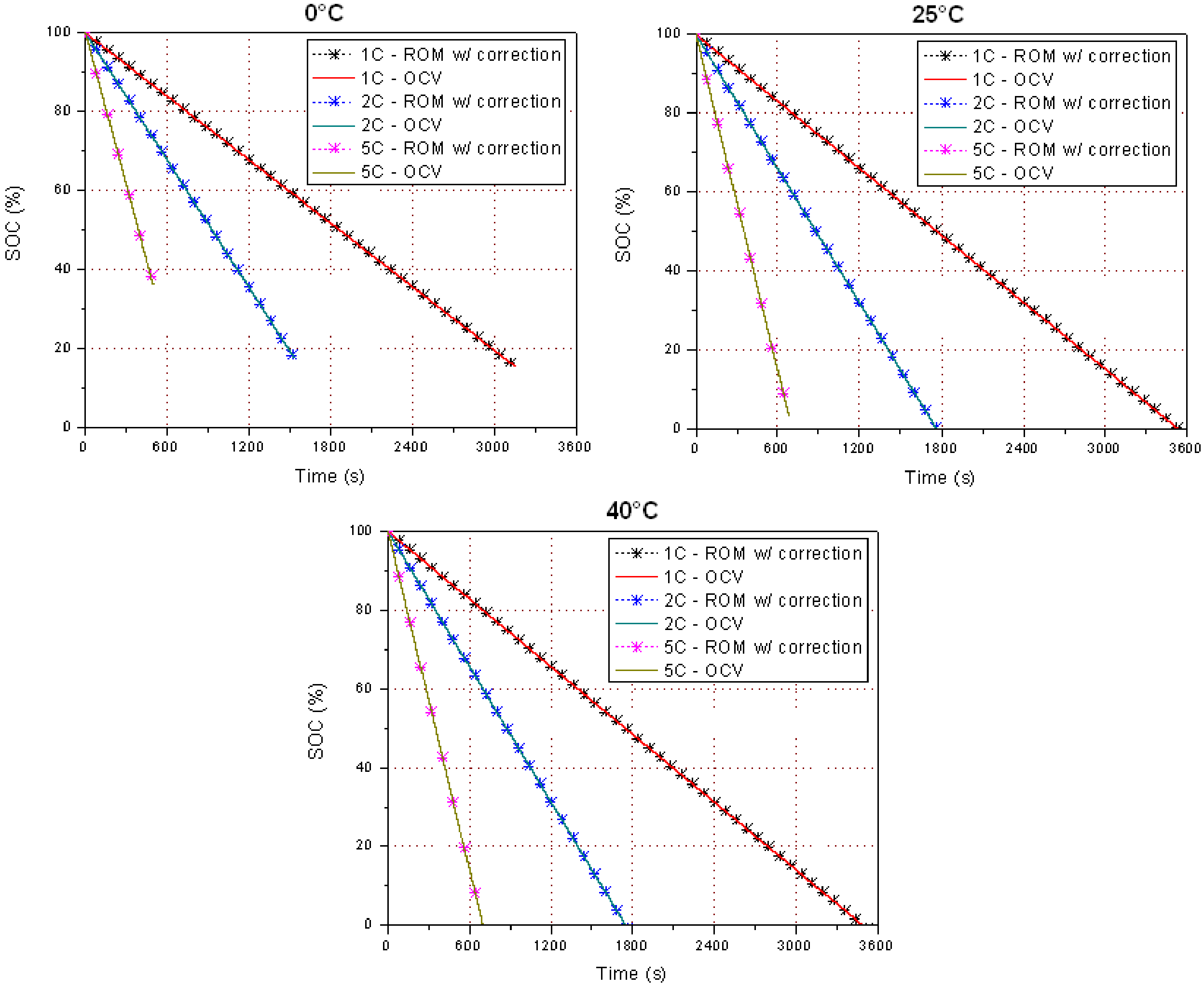

Figure 40: Constant discharge - empirical

Variances (σ^2_i) at each time step are calculated using the equation

$$\sigma_i^2 = (SOC_i - SOC_{OCV})^2$$

where i may represent coulomb counting, the ECM, or the ROM. Variances eliminate any negative values and are able to better show error distribution, compared to taking the absolute value of the differences, when integrated.

Average variances ($\sigma^2_{i,ave}$) are then calculated by

$$\sigma_{i,ave}^2 = \frac{1}{t_{total}} \int_0^{t_{total}} (SOC_i - SOC_{OCV})^2 dt$$

where t_{total} is the total time (s) of a full discharge at a specified current and T_{amb}, as shown in Table 10. Total discharge time increases with temperature and decreases with C-rate.

Table 10: Total discharge times

Current (C-rate)	**T_{amb} (°C)**	**t_{total} (s)**
1	0	3157.4
	25	3569.0
	40	3617.4
2	0	1532.1
	25	1762.3
	40	1801.2
5	0	498.5
	25	683.9
	40	713.5

Average errors ($\sigma_{i,ave}$) are then calculated by

$$\sigma_{i,ave} = \sqrt{\sigma_{i,ave}^2} = \sqrt{\frac{1}{t_{total}} \int_0^{t_{total}} (SOC_i - SOC_{OCV})^2 dt}$$

This process is similar to taking the 2-norm of σ_i. Appendix 4 shows the results for each method. The ROM with error correction based on empirical data has negligible error in every case for a single discharge.

8.4 Single Cycle

The proposed SOC estimation algorithm is applied during a single full cycle, 100% to 0% to 100% SOC, in order to evaluate its accuracy during discharging and charging. Example cycle data at 1C and 0°C is shown in Figure 41.

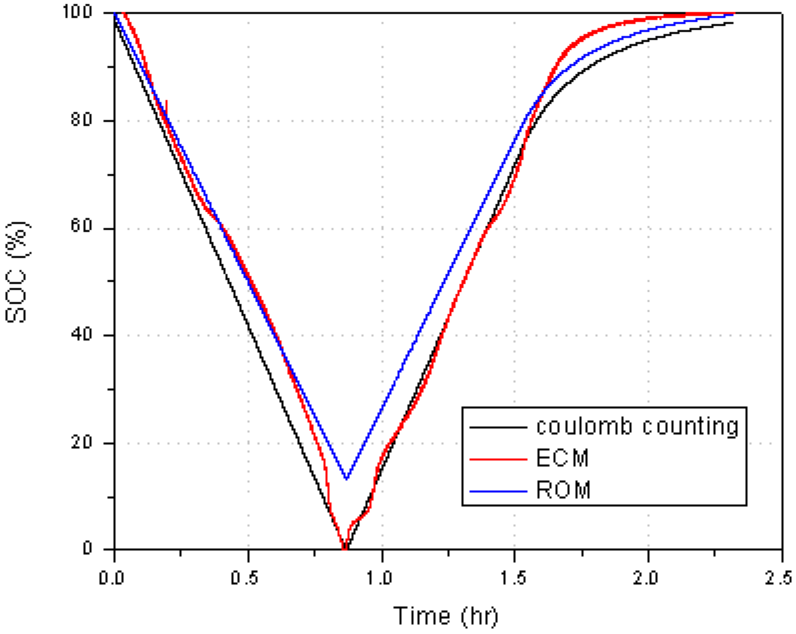

Figure 41: Single cycle data at 1C, 0°C

The table in Appendix 5 shows the final SOC errors when compared to the final OCV for coulomb counting, the ROM, and the ROM with error correction. The ROM with empirical error correction presents considerably more desirable results than the other methods since it was tuned to minimize final SOC error.

8.5 HPPC Test

The HPPC test profile is applied for 1 hour to determine accuracy under pulse load conditions. Example cycle data at 1C and 0°C is shown in Figure 42. The ECM is omitted due to poor performance.

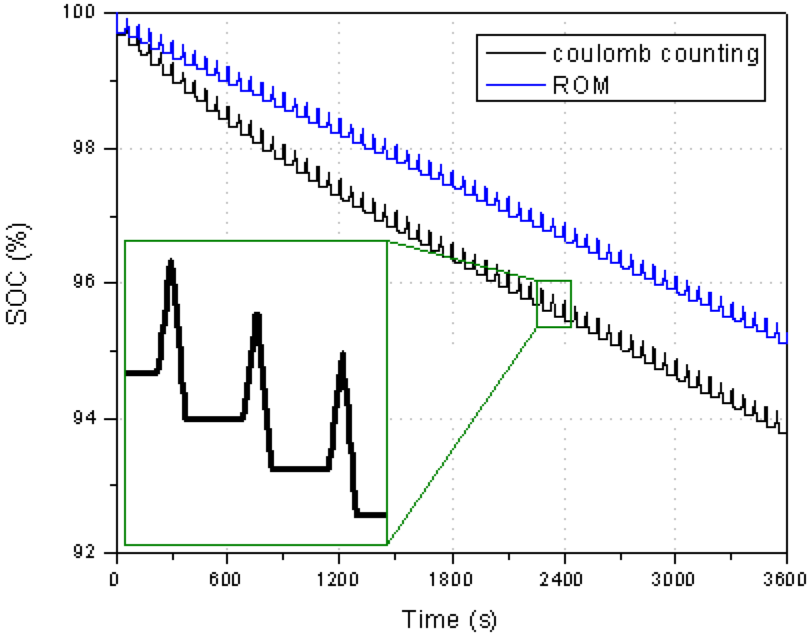

Figure 42: HPPC cycle data at 1C, 0°C

Using the same average error calculation described beforehand, Appendix 6 shows average errors for each method during HPPC tests. The ROM with empirical correction proved to be more accurate at 25°C and 40°C but less accurate at 0°C. This is due to greater changes in temperature at low ambient temperatures with similar internal heat generation rates. These temperature changes affect model parameters. The error rate calculations were based on constant current so they do not aptly capture pulse behavior.

8.6 5 Cycles

Long-term tests are conducted to prove that the ROM error correction is effective. Similar to a single cycle, only final SOC estimates of the ROM and OCV curve may be compared. Example cycle data at 1C and 0°C is shown in Figure 43. The ECM has spikes in SOC after current polarity changes due to time being so great that the exponential terms from its

OCV equation become nearly zero. Basically, concentration and activation overpotentials are ignored.

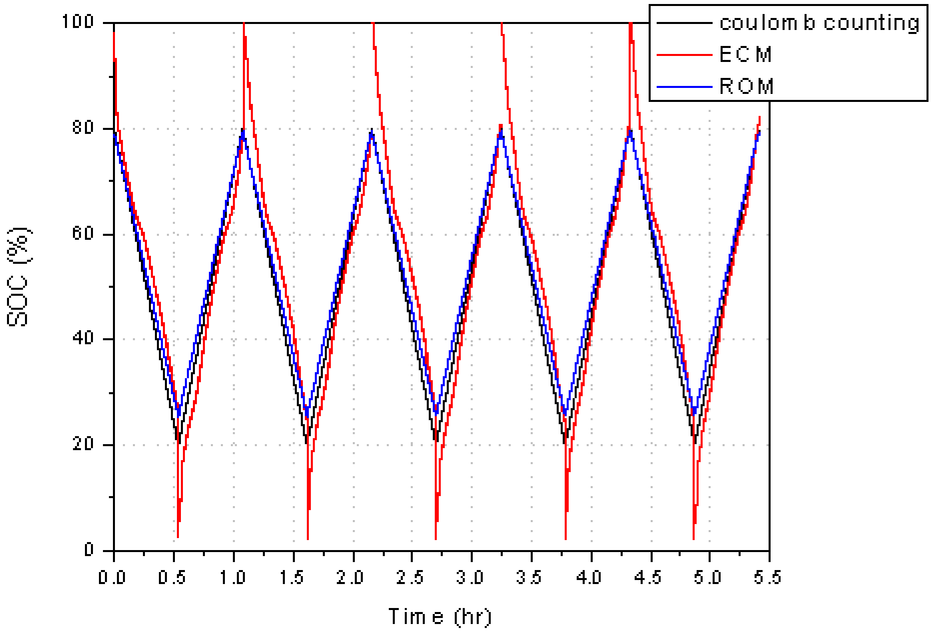

Figure 43: 5 cycle data at 1C, 0°C

Appendix 7 illustrates the final SOC error after 5 cycles at various ambient temperatures and C-rates. The ROM with empirical correction proved far less accurate than the original ROM in every case. Obviously, the charge error rates are not appropriate for cycling conditions since they were calculated based on CC/CV charging modes rather than just CC mode as is the circumstance for the 5 cycle tests.

Chapter 9: SOC Estimation Error Compensation of ROM Using a Feedback Method

The empirical method proves to have immaculate accuracy during a single discharge and single cycle loading, but pulse and long-term accuracy is questionable. The error rates are not adjustable so if the dynamics of a battery differ much from those used for error rate calculations then error will grow radically. To counter this, a second SOC estimation algorithm is proposed that corrects the error associated with ROM estimates using a feedback loop. Figure 44 shows the schematic block diagram. Theoretically, this approach should eliminate accumulating CT and ROM errors by comparison to battery terminal voltage measurements.

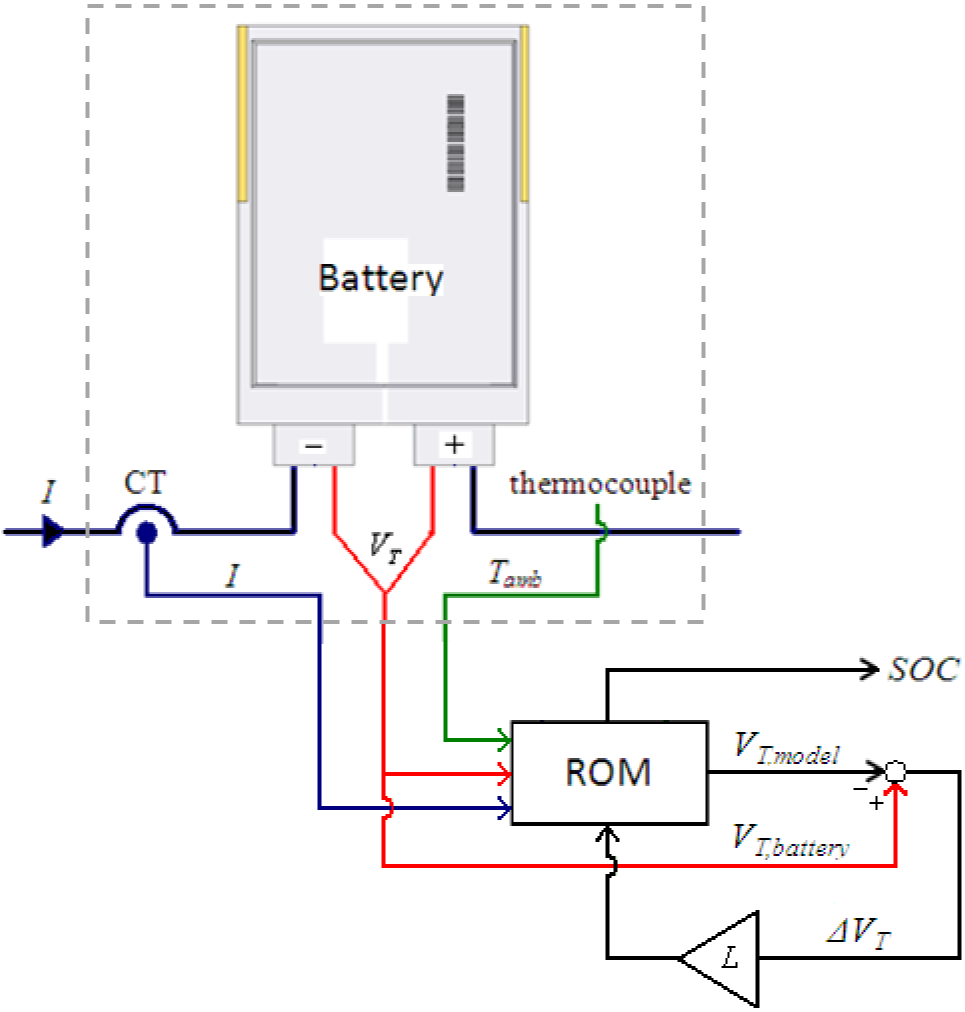

Figure 44: Feedback method schematic block diagram

9.1 Feedback Design

A typical state space observer model takes the form of

$$x^{k+1} = Ax^k + Bu + L \cdot error$$
$$y^{k+1} = Cx^{k+1} + Du$$

where L is an observer gain.

With the proposed method, the difference in terminal voltage (ΔV_T) between the ROM and the battery is treated as the error term, so the state space model is of the form

$$S^{k+1} = A \cdot S^{k} + Bu + L \cdot \Delta V_T$$
$$V_T^{k+1} = C \cdot S^{k+1} + Du$$

where S is the stoichiometry number, which is related to $c_{s,ave}$ and subsequently SOC, to be discussed later. This representation demonstrates that L must be a vector. First, an appropriate correction term insertion point must be determined. The model function containing $c_{s,ave}$ is

$$\frac{d}{dt} c_{s,ave} + 3 \frac{j^{Li}}{R_s a_s F} = 0$$

After discretization the equation becomes

$$\frac{c_{s,ave}^{k+1} - c_{s,ave}^{k}}{\Delta t} = -3 \frac{j^{Li}}{R_s a_s F}$$

Then k and $k+1$ terms are separated as shown

$$c_{s,ave}^{k+1} = c_{s,ave}^{k} - 3 \frac{j^{Li}}{R_s a_s F} \cdot \Delta t$$

in order to solve all $k+1$ terms simultaneously with the accompaniment of all the other unaffected equations in the model.

Since $c_{s,ave}$ is nonlinear through the thickness of an electrode, an average value of all particles across the electrode thickness is used to calculate SOC using S in the equation

$$SOC = \frac{S - S_0}{S_{100} - S_0}$$

where

$$S = \frac{\overline{c_{s,ave}}}{c_{s,\max}}$$

Also, j^{Li} can be averaged as

$$\frac{\sum j^{Li} \cdot \Delta\delta}{\delta} = \frac{I}{A \cdot \delta}$$

If the previous equation for $c_{s,ave}$ is altered by substituting in the average values of $c_{s,ave}$ and j^{Li} then dividing through by $c_{s,max}$ the equation for the anode, with inclusion of error correction, becomes

$$S^{k+1} = A \cdot S^k + Bu + L \cdot \Delta V_T \rightarrow S^{k+1} = S^k - \frac{1}{c_{s,\max}} \frac{3 \cdot I}{R_s a_s FA\delta} \cdot \Delta t + L \cdot \Delta V_T \cdot \Delta t$$

where new coefficients for the A and B matrices are shown.

The state space output is derived after linearization of S as follows

$$V_T = OCV - \eta = f(S) - \eta \approx C \cdot S - \eta$$

So the C and D matrix coefficients remain unchanged in

$$V_T^{k+1} = OCV - \eta \rightarrow V_T^{k+1} = C \cdot S^{k+1} + Du$$

9.2 Gain Optimization

The observer gain vector (L) consists of 3 sections to account for the anode, cathode, and separator. In accordance with charge conservation laws, whatever value is subtracted from the anode must be added to the cathode typified in the equation

$$[\ell \cdot \delta \cdot \varepsilon_s]_{anode} = -[\ell \cdot \delta \cdot \varepsilon_s]_{cathode}$$

where A and F were on both sides but cancelled out and L in the separator region is 0. When the model parameters are plugged in the equation becomes

$$\ell_{anode} \cdot 50 \times 10^{-4} \cdot 0.58 = -\ell_{cathode} \cdot 36.4 \times 10^{-4} \cdot 0.5$$

Then separate unknown variables from the given numbers and multiply numerator and denominator by a common multiplier (ℓ) to attain

$$\ell_{anode} = -\ell \cdot 36.4 \times 10^{-4} \cdot 0.5 \text{ and } \ell_{cathode} = \ell \cdot 50 \times 10^{-4} \cdot 0.58$$

So L takes the form of

$$L = \begin{bmatrix} \left.\begin{matrix} -36.4\times10^{-4}\cdot 0.5 \\ \vdots \\ -36.4\times10^{-4}\cdot 0.5 \end{matrix}\right\} anode \\ \left.\begin{matrix} 0 \\ \vdots \\ 0 \end{matrix}\right\} separator \\ \left.\begin{matrix} 50\times10^{-4}\cdot 0.58 \\ \vdots \\ 50\times10^{-4}\cdot 0.58 \end{matrix}\right\} cathode \end{bmatrix} \cdot \ell$$

where ℓ is optimized by pole placement using the MATLAB function “place()”. Desired poles are optimized based on state space matrices A and C to provide a constant optimized gain. The desired pole must be negative for system stability. Performance of pole placement was determined based a trial and error method considering many different poles by analyzing the resultant SOC estimation error. The resulting desired pole was -0.5 with an associated gain of ℓ = 0.0442.

9.3 Single Discharge

The algorithm with feedback is applied to the single discharge data previously shown for the ROM, as portrayed in Figure 45. There is a significant improvement in SOC estimation accuracy in all cases. The maximum SOC error is > 10% near the end of a 5C, 0°C discharge suggesting improper low temperature model parameters, such as *k* or *h*. Errors are greatest in the SOC range 0-20% due to a rapid measured terminal voltage drop-off relative to model estimates. ROM overpotential estimates are erroneous near the end of discharge. In HEV/EV application this is of little concern since a battery pack will never experience < 20% SOC. Errors at the beginning of discharge are associated with improper initial SOC estimation. Since the gain is fairly small, the model requires time to adjust to large initial ΔV_T’s.

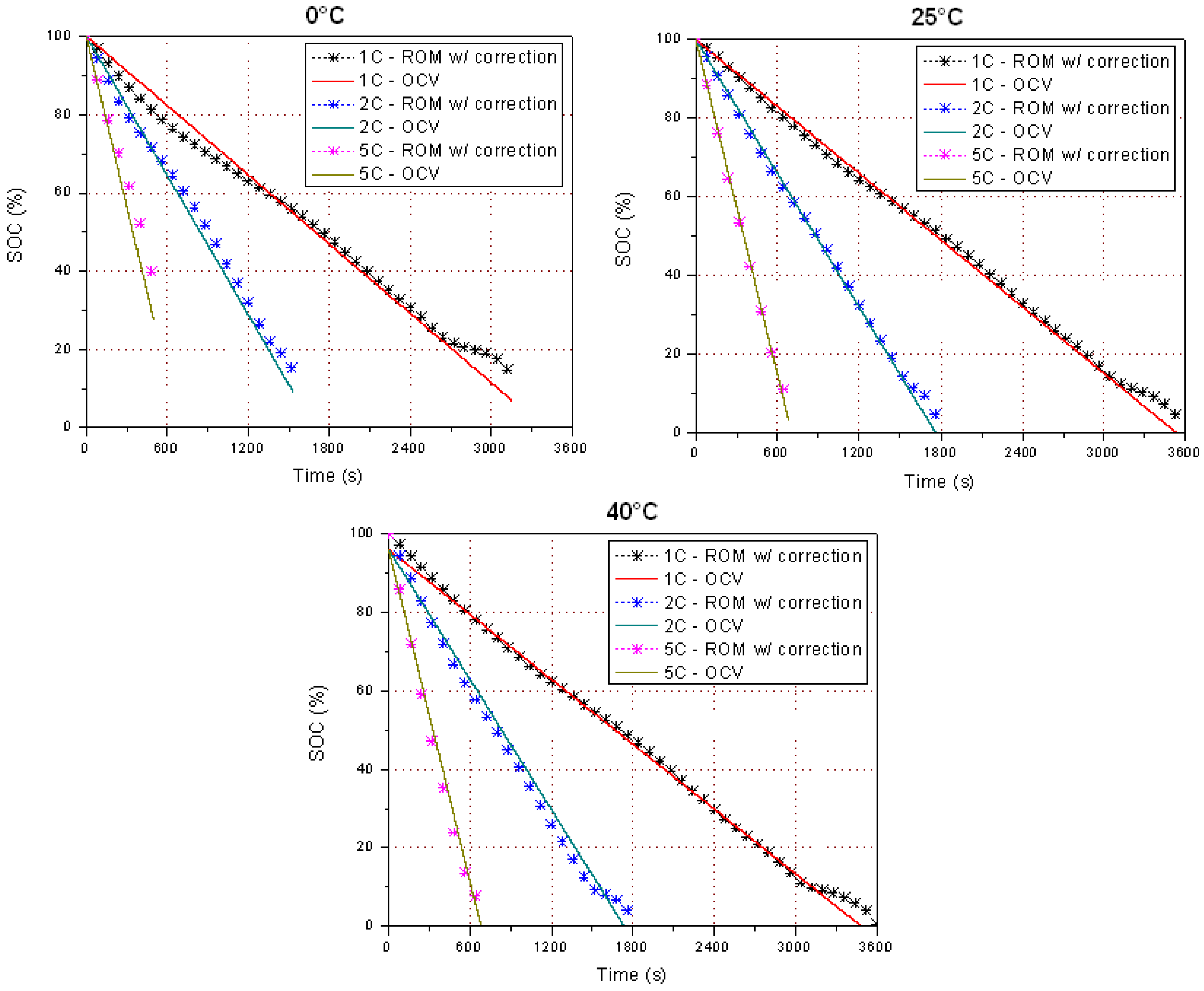

Figure 45: Constant discharge - feedback

Average errors ($\sigma_{i,ave}$) are calculated the same way as before. Results are included in Appendix 4. At low temperature the ROM with feedback proves advantageous over the regular ROM, but the opposite is true at high temperature with the difference being less than 1% SOC. Its average error was < 5% SOC in every case.

9.3.1 Effect of Feedback

The ROM with feedback error compensation will be compared to the ROM without error compensation and coulomb counting to determine how the SOC estimate is corrected during each type of test. All plots are considering data recorded during experiments at 1C and 25°C. All other C-rates and ambient temperatures demonstrated similar trends. Figure 46 shows results during a single constant current full discharge. The deviation is almost identical to that from the OCV line with the maximum being 2.9% SOC.

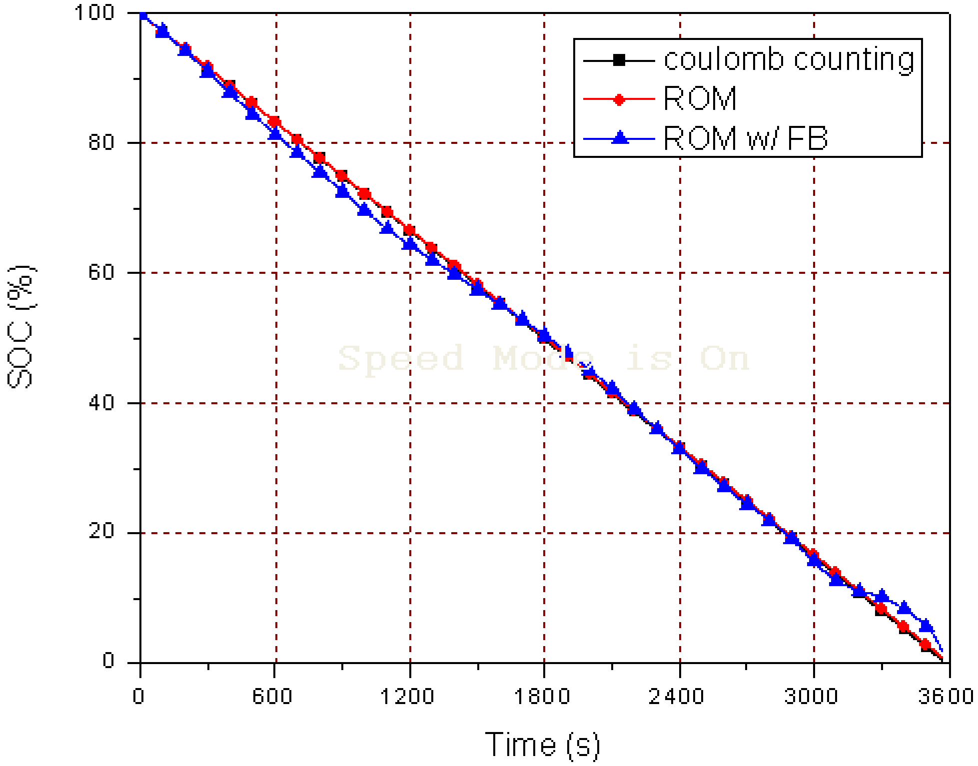

Figure 46: Effect of feedback - single discharge

9.4 Single Cycle

The proposed SOC estimation algorithm is applied during a single full cycle, 100% to 0% to 100% SOC, in order to evaluate its accuracy during discharging and charging. Final SOC error results are included in Appendix 5. The ROM with feedback revealed < 2% SOC error in every case.

9.4.1 Effect of Feedback

Figure 47 shows results during a single cycle. During discharge, the feedback correction shows little change from the original ROM. During charge, SOC is greater due to correction from terminal voltage measurements leading to a more accurate final SOC value. SOC does not reach 0% with the ROM since reaching the V_{min} of 2.5V at 1C does not indicate full depletion of lithium-ions, referring to S_0, in the anode. Residual charge could be extracted if a lower current was applied.

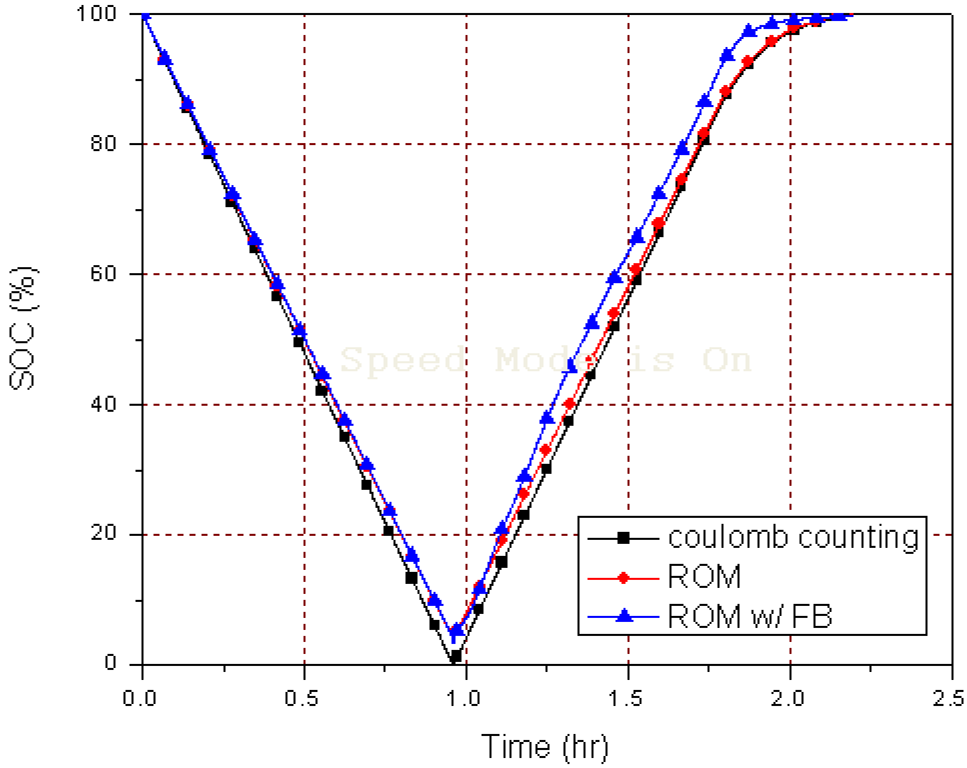

Figure 47: Effect of feedback - single cycle

9.5 HPPC Test

The HPPC test profile is applied for 1 hour to determine accuracy under pulse load conditions. Average SOC errors of the ROM with feedback for various operating conditions are included in Appendix 6. Average error is < 5% SOC in every test.

9.5.1 Effect of Feedback

Figure 48 shows results during one hour of HPPC testing. The ROM with feedback error compensation has a slightly greater SOC estimate in the range of 100-98.5% and slightly lower SOC estimate in the range 96-95% which leads to less average error overall.

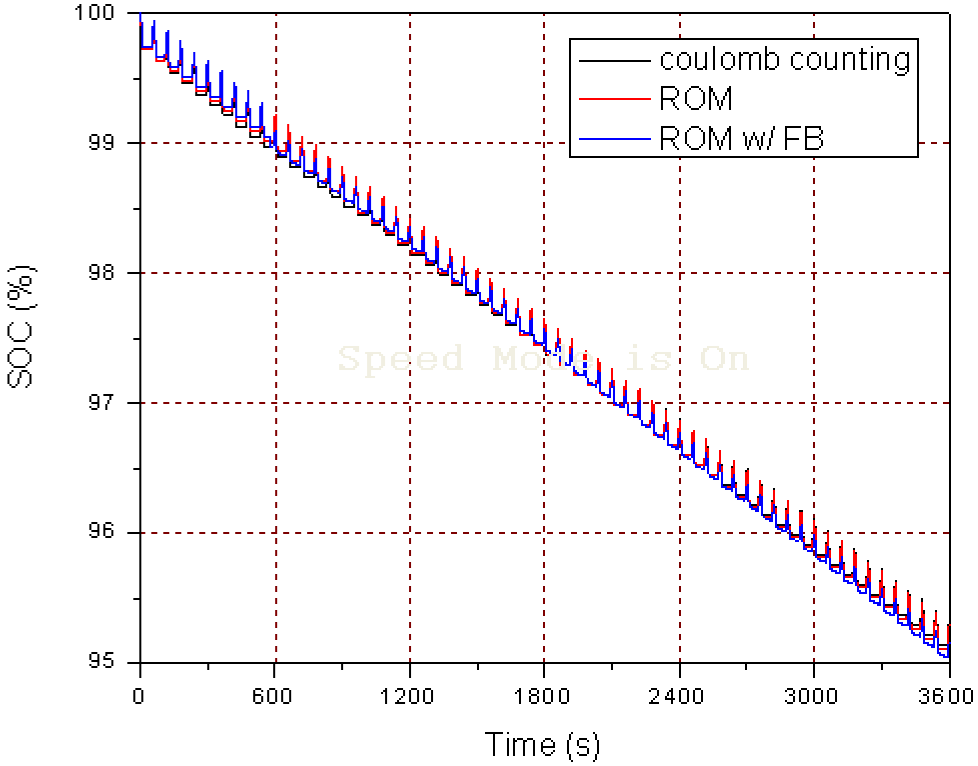

Figure 48: Effect of feedback - HPPC

9.6 5 Cycles

Long-term tests are conducted to prove that the ROM error correction is effective. Similar to a single cycle, only final SOC estimates of the ROM and OCV curve may be compared. Results are included in Appendix 7. The ROM with feedback revealed < 3.5% SOC error in every case.

9.6.1 Effect of Feedback

Figure 49 shows results during 5 cycles. The SOC estimates from the ROM with feedback error compensation never reach 20% or 80% due to terminal voltage measurements greater than or less than, respectively, the ROM terminal voltage estimates.

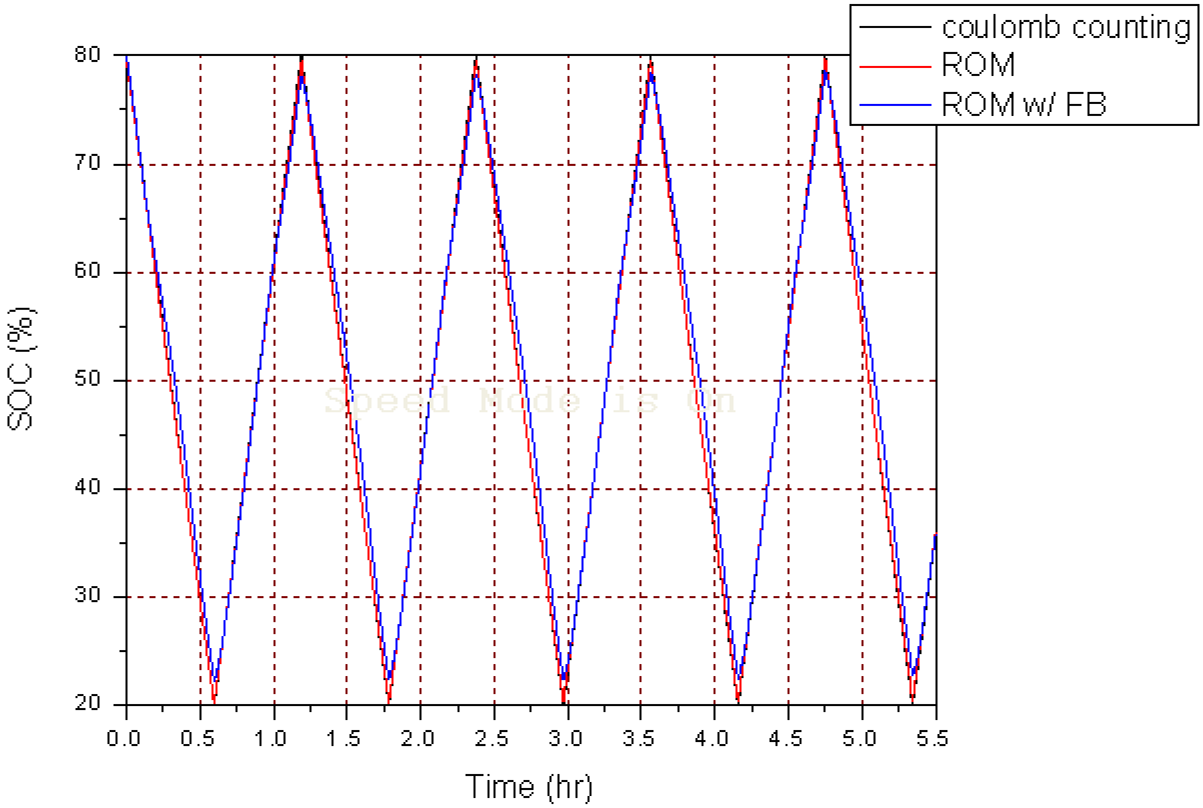

Figure 49: Effect of feedback - 5 cycles

SOC estimates of the proposed methods are compared to classical methods during various charge modes. An error analysis determines which method performs best under which operating conditions.

10.1 Charge-Depleting Mode

Single discharge and HPPC test SOC estimation method errors are analyzed in this section. Figures 50-52 show the data in Tables 11 and 13 graphically. The black dashed line represents the typical OEM SOC error estimate maximum of 5%. ECM estimates were removed so as not to skew the plot scales since its error was notably more for each instance. Some errors are too small to see in the plots.

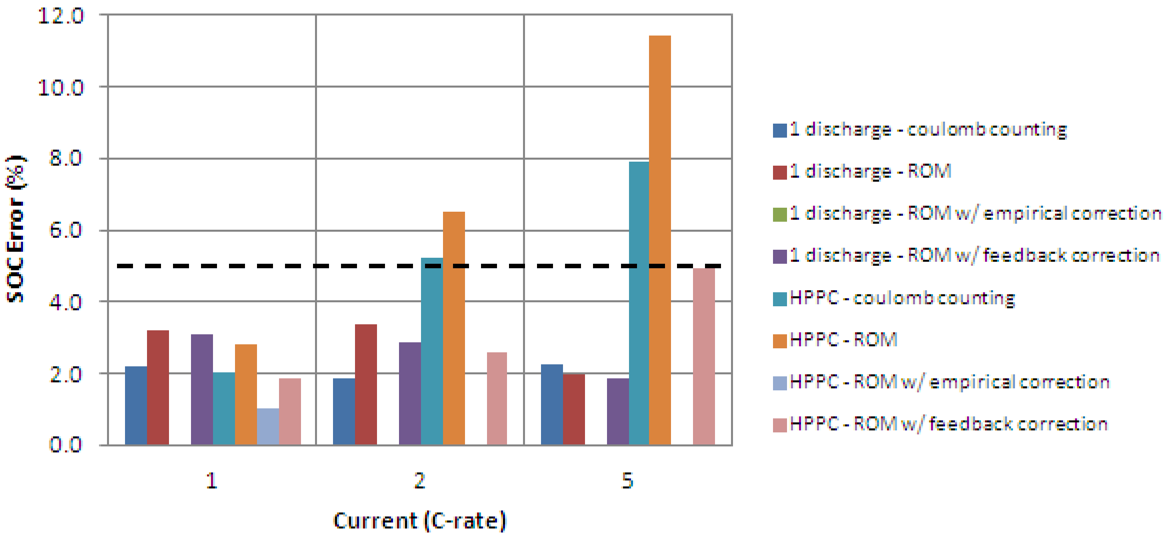

Figure 50: Charge-depleting cycle analysis at 0°C

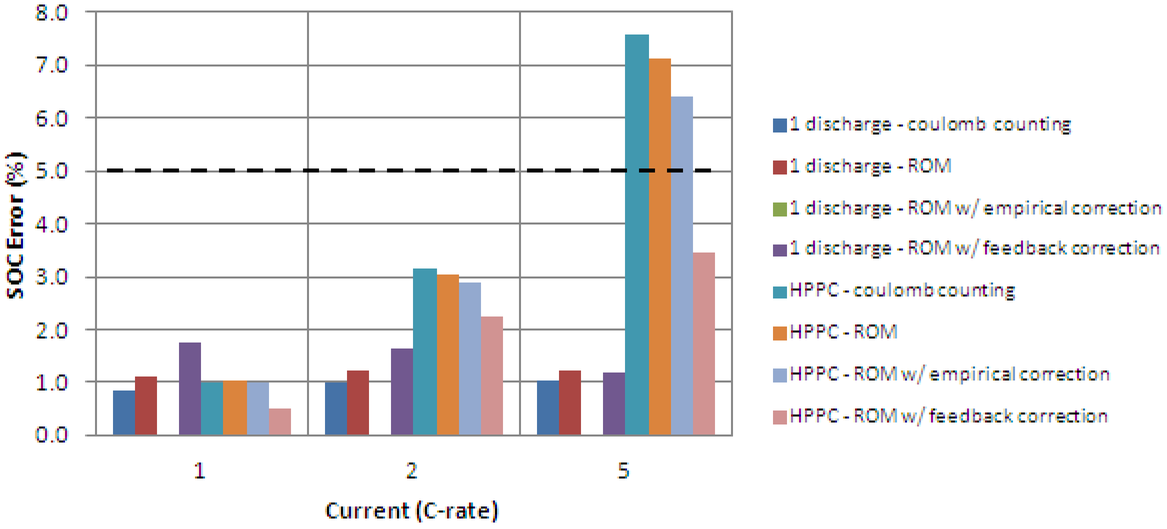

Figure 51: Charge-depleting cycle analysis at 25°C

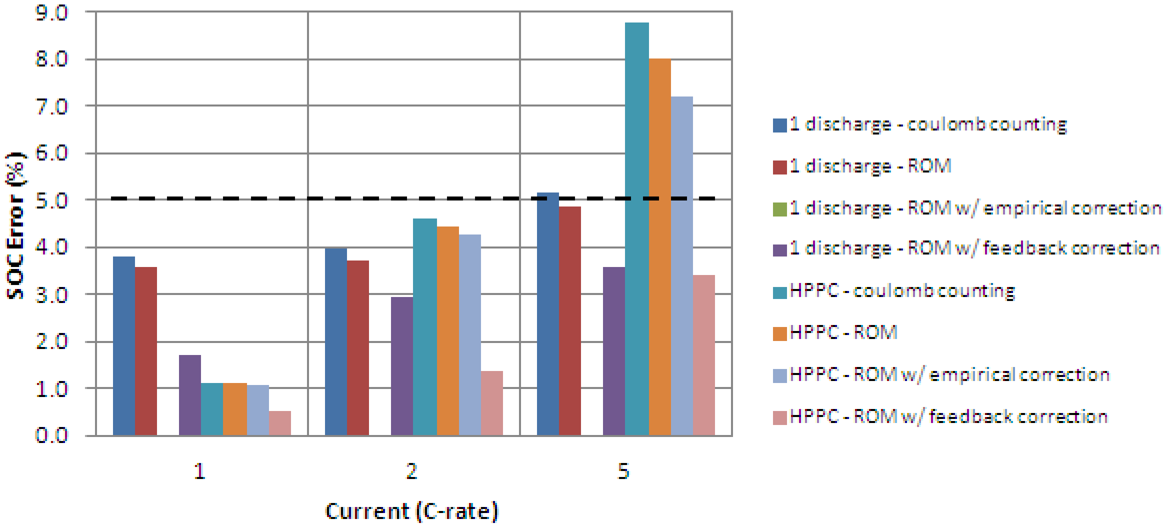

Figure 52: Charge-depleting cycle analysis at 40°C

The ROM with feedback correction is the only method that achieves the SOC accuracy target of > 95% in all situations. Average errors were the least at 25°C since the OCV curve standard temperature is 25°C, increased with C-rate due to increases in heat generation rate that are not perfectly accounted for in the thermal component of the model, and were greater during HPPC testing since it constitutes a pulsed current profile. The charge error rates are based on

CC/CV charging yet the HPPC testing is only CC charging. The proposed feedback method proves to be the best option for the range of investigated currents and ambient temperatures.

10.2 Charge-Sustaining Mode

Single full cycle and 5 partial cycles SOC estimation methods errors are analyzed in this section. This charge mode has the disadvantage that results may not be dynamically compared to the OCV curve since the data is not monotonically decreasing or increasing with rest periods before and after. Figures 53-55 show SOC error data for all methods after a single 100-0-100% cycle and after 5 80-20-80% cycles. Note that the *y*-axes are absolute values of the final SOC errors. Same as before, some errors are too small to see in the plots.

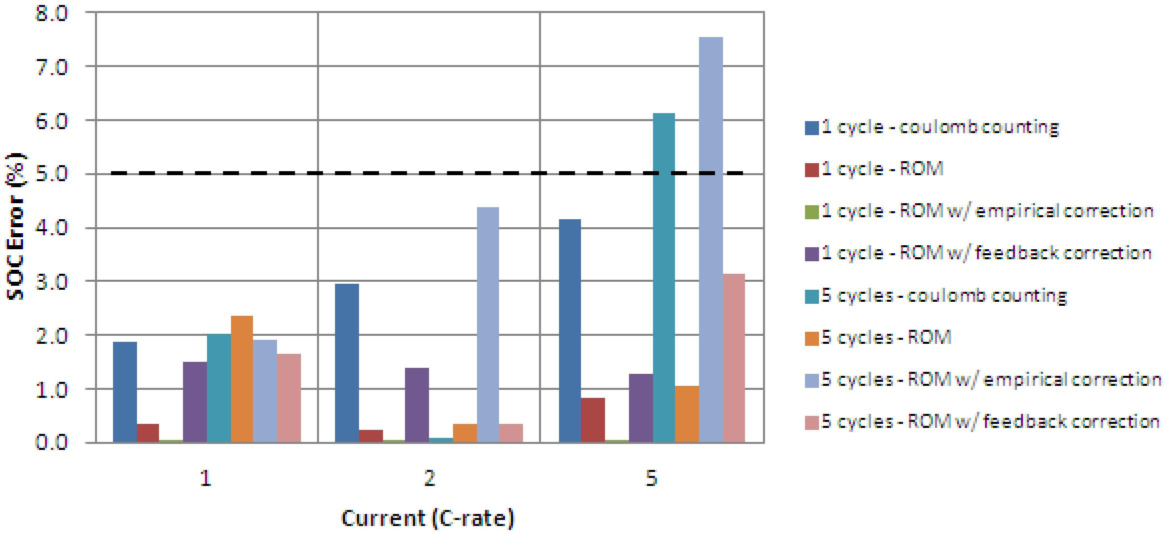

Figure 53: Charge-sustaining cycle analysis at 0°C

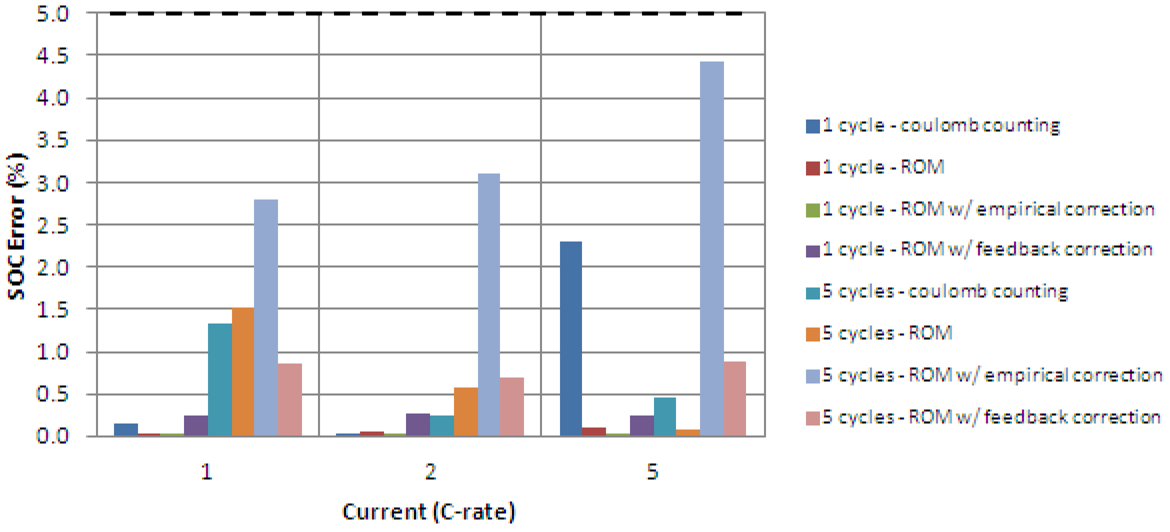

Figure 54: Charge-sustaining cycle analysis at 25°C

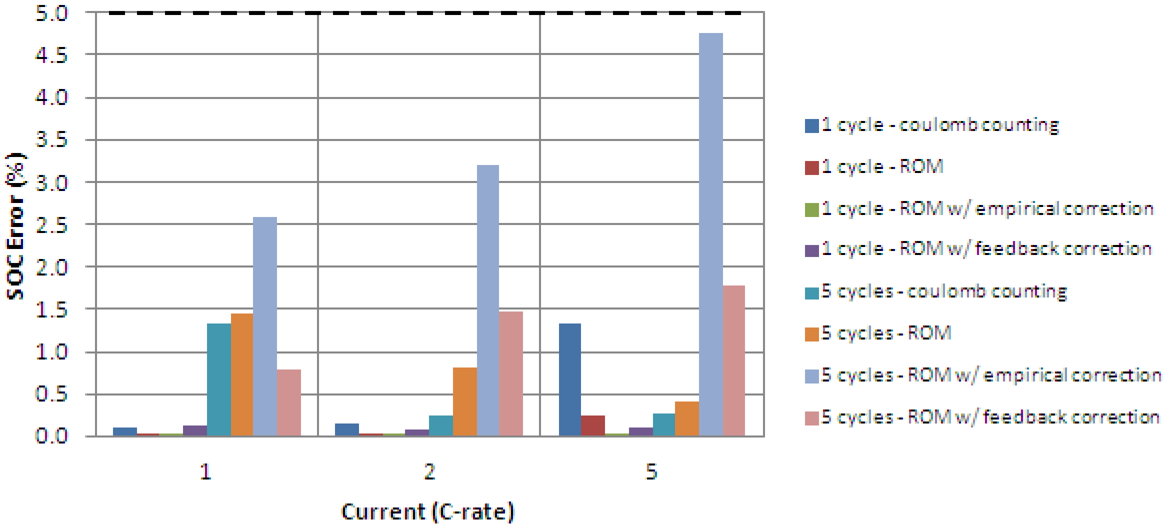

Figure 55: Charge-sustaining cycle analysis at 40°C

The ROM with error correction performs best and achieves the target of less than 5% final SOC error for all investigated operating conditions, as do most other methods. The results from the ROM with empirical correction have significant error suggesting that the charge error rates chosen are not appropriate. In general, greatest accuracy is attained at 25°C with low current for the same reasons mentioned in the previous section.

Chapter 11: Conclusions and Future Work

Battery state of charge estimation methods were evaluated to determine which has the greatest accuracy under various loading conditions. The ROM proved superior to coulomb counting and the ECM in each test when the results were compared to an OCV curve. Improvements were made to the ROM and two novel SOC estimation techniques were evaluated.

The first method uses empirical data to tune SOC estimates. ROM error during a single discharge was found to be linear due to small flaws in model parameters that accumulate with each time step. Due to this linearity, error rates were calculated and applied to the ROM estimates, drastically reducing error. Of the 36 examined cases, 3 did not meet the aforementioned target of > 95% accuracy; however, during a single discharge or single cycle the accuracy is impeccable. Unfortunately, a HEV or EV charge demand profile will realistically never be constant.

The second method attempts to counteract the inherent drawbacks of assuming constant error rates by including the ROM in a closed-loop feedback system whereby model SOC estimates are updated continuously by comparing the model terminal voltage estimate to battery terminal voltage measurements. A variable gain is implemented to maintain the state space poles in the desired location. Of the 36 examined cases, all met the aforementioned target of > 95% accuracy, making this algorithm ideal for potential use in all HEVs and EVs.

Theoretically, the proposed SOC estimation method would perform well with other advanced battery types as long as the model parameters were updated to reflect changes in battery chemistry. All of the physics-based equations used in the ROM remain applicable. A future improvement might be to update the thermal component of model so as to better capture internal heat generation at high C-rates.

Other equivalent circuit models may be considered such as a Randle of order greater than 3 or a modified Thevenin, even though it has been stated that a 2nd order Randle model provides the greatest efficiency [4]. Also, other electrochemical models could be assessed such as full order single particle or porous electrode models. These offer marginal accuracy gains at the price of excessive computational power required for calculation. Studying how each ROM model parameter varies with temperature and age is a worthwhile venture.

Future work should include the investigation of the accuracy of this SOC estimation algorithm outside the range of 0-40°C and 1-5C. There is little documentation on sub-zero temperature as well as high C-rate effects on Li-polymer batteries. Also, longer cycling times would increase confidence in the proposed method. Being a relatively new technology, there is much to explore.

State of health estimation is the next evolutionary phase. Tracking changes in maximum lithium concentration would enable SOC to always maintain the range of 0-100% in electrochemical models. The ROM with feedback correction would be ideal if it could be updated periodically to account for cell degradation and maintain accuracy in all realistic operating conditions.

References

[1] D. Andre, M. Meiler, K. Steiner, C. Wimmer, T. Soczka-Guth, and D. U. Sauer, “Characterization of high-power lithium-ion batteries by electrochemical impedance spectroscopy. I. Experimental investigation,” *Journal of Power Sources*, vol. 196, pp. 5334-5341, 2011.

[2] H. Chaoui and P. Sicard, “Accurate State of Charge (SOC) Estimation for Batteries using a Reduced-order Observer,” *IEEE*, pp. 39-43, 2011.

[3] H. He, R. Xiong, X. Zhang, F. Sun, and J. Fan, “State-of-Charge Estimation of the Lithium-Ion Battery Using an Adaptive Extended Kalman Filter Based on an Improved Thevenin Model,” *IEEE Transactions on Vehicular Technology*, vol. 60, no. 4, pp. 1461-1469, 2011.

[4] T. Hu, B. Zanchi, and J. Zhao, “Determining battery parameters by simple algebraic method,” *2011 American Control Conference*, San Francisco, CA, June 29-July 1, pp. 3090-3095, 2011.

[5] X. Hu, F. Sun, Y. Zuo, and H. Peng, “Online Estimation of an Electric Vehicle Lithium-Ion Battery Using Recursive Least Squares with Forgetting,” *2011 American Control Conference*, San Francisco, CA, June 29-July 1, pp. 935-940, 2011.

[6] J. Kim, J. Shin, C. Jeon, and B. Cho, “High Accuracy State-of-Charge Estimation of Li-Ion Battery Pack based on Screening Process,” *IEEE*, pp. 1984-1991, 2011.

[7] J.-H. Lee and W. Choi, “Novel State-of-Charge Estimation Method for Lithium Polymer Batteries Using Electrochemical Impedance Spectroscopy,” *Journal of Power Electronics*, vol. 11, no. 2, pp. 237-243, 2011.

[8] X. Li, M. Xiao, K. Malinowski, and S.-Y. Choe, “State-of-charge (SOC) estimation based on reduced order of electrochemical model for a pouch type high power Li-polymer battery,” *IEEE Vehicle Power and Propulsion Conference*, Chicago, IL, September 6-9, 2011.

[9] X. Li, M. Xiao, and S.-Y. Choe, “Reduced order of electrochemical model for a pouch type high power Li-polymer battery,” *International Conference on Clean Electrical Power*, Ischia, Italy, June 14-16, 2011.

[10] Y. Li, R. D. Anderson, J. Song, A. M. Phillips, and X. Wang, “A Nonlinear Adaptive Observer Approach for State of Charge Estimation of Lithium-Ion Batteries,” *2011 American Control Conference*, San Francisco, CA, June 29-July 1, pp. 370-375, 2011.

[11] Y. Shi, G. Prasad, Z. Sheng, and C. D. Rahn, “Discretization Methods for Battery Systems Modeling,” *2011 American Control Conference*, San Francisco, CA, June 29-July 1, pp. 356-361, 2011.

[12] F. Sun, X. Hu, Y. Zou, and S. Li, “Adaptive unscented Kalman filtering for state of charge estimation of a lithium-ion battery for electric vehicles,” *Energy*, vol. 36, no. 5, pp. 3531-3540, 2011.

[13] X. Tang, X. Mao, J. Lin, and B. Koch, “Li-ion Battery Parameter Estimation for State of Charge,” *2011 American Control Conference*, San Francisco, CA, June 29-July 1, pp. 941-946, 2011.

[14] M. Charkhgard and M. Farrokhi, “State-of-Charge Estimation for Lithium-Ion Batteries Using Neural Networks and EKF,” *IEEE Transactions on Industrial Electronics*, vol. 57, no. 12, pp. 4178-4187, 2010.

[15] N. A. Chaturvedi, R. Klein, J. Christensen, J. Ahmed, and A. Kojic, “Modeling, estimation, and control challenges for lithium-ion batteries,” *2010 American Control Conference*, Baltimore, Maryland, USA, June 30-July 2, 2010.

[16] Y. Hu and S. Yurkovich, “Battery State of Charge Estimation in Automotive Applications using LPV Techniques,” *2010 American Control Conference*, Baltimore, MD, USA, June 30-July 2, 2010.

[17] X. Hu, F. Sun, and Y. Zou, “Estimation of State of Charge of a Lithium-Ion Battery Pack for Electric Vehicles Using and Adaptive Luenberger Observer,” *Energies*, vol. 3, pp. 1586-1603, 2010.

[18] R. Klein, N. A. Chaturvedi, J. Christensen, J. Ahmed, R. Findeisen, and A. Kojic, “State estimation of a reduced electrochemical model of a lithium-ion battery,” *2010 American Control Conference*, Baltimore, Maryland, USA, June 30-July 2, 2010.

[19] M. Knauff, C. Dafis, and D. Niebar, “A New Battery Model For Use With An Extended Kalman Filter State Of Charge Estimator,” *2010 American Control Conference*, Baltimore, Maryland, USA, June 30-July 2, 2010.

[20] V. Ramadesigan, V. Boovaragavan, J. C. Pirkle, Jr., and V. R. Subramanian, “Efficient Reformulation of Solid-Phase Diffusion in Physics-Based Lithium-Ion Battery Models,” *Journal of The Electrochemical Society*, vol. 157, no. 7, pp. A854-A860, 2010.

[21] S. Santhanagopalan and R. E. White, “State of charge estimation using an unscented filter for high power lithium-ion cells,” *International Journal of Energy Research*, vol. 34, pp. 152-163, 2010.

[22] J. B. Siegel, X. Lin, A. G. Stefanopoulou, and D. Gorsich, “Neutron Imaging of Lithium Concentration for Validation of Li-Ion Battery State of Charge Estimation,” Unclassified: U.S. Army, 2010.

[23] K. A. Smith, C. D. Rahn, and C.-Y. Wang, “Model-Based Electrochemical Estimation and Constraint Management for Pulse Operation of Lithium-ion Batteries,” *IEEE Transactions on Controls Systems Technology*, vol. 18, no. 3, pp. 654-663, 2010.

[24] M. Xiao, S.-Y. Choe, and F. Rahman, “Static and dynamic analysis of Li-polymer battery using thermal electrochemical model,” *2010 IEEE Conference on Innovative Technologies for an Efficient and Reliable Electricity Supply*, Waltham, MA, USA, September 27-29, 2010.

[25] A. Zenati, P. Desprez, and H. Razik, “Estimation of the SOC and the SOH of Li-ion Batteries, by combining Impedance Measurements with the Fuzzy Logic Inference,” *IEEE*, pp. 1767-1772, 2010.

[26] F. Codecà, S. M. Savaresi, and V. Manzoni, “The mix estimation algorithm for battery State-of-Charge estimator – Analysis of the sensitivity to measurement errors,” *Joint 48th IEEE Conference on Decision and Control and 28th Chinese Control Conference*, Shanghai, P. R. China, December 16-18, 2009.

[27] A. Cuadras and O. Kanoun, “SOC Li-ion Battery Monitoring With Impedance Spectroscopy,” *6th International Multi-Conference on Systems, Signals, and Devices*, 2009.

[28] H. Dai and X. Wei, “A New SOH Prediction Concept for the Power Lithium-ion Battery Used on HEVs,” *IEEE*, pp. 1649-1653, 2009.

[29] C. R. Gould, C. M. Bingham, D. A. Stone, and P. Bentley, “New Battery Model and State-of-Health Determination Through Subspace Parameter Estimation and State-Observer Techniques,” *IEEE Transactions on Vehicular Technology*, vol. 58, no. 8, pp.

3905-3916, 2009.

[30] K. S. Ng, C. Moo, Y. Chen, and Y. Hsieh, "Enhanced coulomb counting method for estimating state-of-charge and state-of-health of lithium-ion batteries," *Applied Energy*, vol. 86, pp. 1506–1511, 2009.

[31] V. Pop, H.J. Bergveld, P.H.L. Notten, J.H.G. Op het Veld, and P.P.L. Regtien, "Accuracy analysis of the State-of-Charge and remaining run-time determination for lithium-ion batteries," *Measurement*, vol. 42, pp. 1131–1138, 2009.

[32] C. Speltino, D. Di Domenico, G. Fiengo, and A. Stefanopoulou, "Comparison of Reduced Order Lithium-Ion Battery Models for Control Applications," *Joint 48th IEEE Conference on Decision and Control and 28th Chinese Control Conference*, Shanghai, P. R. China, December 16-18, 2009.

[33] C. Speltino, D. Di Domenico, G. Fiengo, and A. Stefanopoulou, "Experimental Identification and Validation of a Lithium-Ion Battery State of Charge Estimation with an Extended Kalman Filter," unpublished, 2009.

[34] F. Codecà, S. M. Savaresi, and G. Rizzoni, "On battery State of Charge estimation: a new mixed algorithm," *17th IEEE International Conference on Control Applications Part of 2008 IEEE Multi-conference on Systems and Control*, San Antonio, Texas, USA, September 3-5, 2008.

[35] M. Coleman, W. G. Hurley, and C. K. Lee, "An Improved Battery Characterization Method Using a Two-Pulse Load Test," *IEEE Transactions on Energy Conversion*, vol. 23, no. 2, pp. 708-713, 2008.

[36] D. Di Domenico, G. Fiengo, and A. Stefanopoulou, "Lithium-Ion battery State of Charge estimation with a Kalman Filter based on a electrochemical model," *17th IEEE International Conference on Control Applications Part of 2008 IEEE Multi-conference on Systems and Control*, San Antonio, Texas, USA, September 3-5, 2008.

[37] I.-S. Kim, "Nonlinear State of Charge Estimator for Hybrid Electric Vehicle Battery," *IEEE Transactions on Power Electronics*, vol. 23, no. 4, pp. 2027-2034, 2008.

[38] S. Lee, J. Kim, J. Lee, and B. H. Cho, "State-of-charge and capacity estimation of lithium-ion battery using a new open-circuit voltage versus state-of-charge," *Journal of Power Sources*, vol. 185, pp. 1367-1373, 2008.

[39] S. Santhanagopalan and R. E. White, "State of Charge Estimation for Electrical Vehicle Batteries," *17th IEEE International Conference on Control Applications Part of 2008 IEEE Multi-conference on Systems and Control*, San Antonio, Texas, USA, September 3-5, 2008.

[40] K. A. Smith, C. D. Rahn, and C.-Y. Wang, "Model-Based Electrochemical Estimation of Lithium-Ion Batteries," *17th IEEE International Conference on Control Applications Part of 2008 IEEE Multi-conference on Systems and Control*, San Antonio, Texas, USA, September 3-5, 2008.

[41] C. Speltino, D. Di Domenico, G. Fiengo, and A. Stefanopoulou, "Experimental identification and validation of an electrochemical model of a Lithium-Ion Battery," unpublished, 2008.

[42] M. Coleman, C.K. Lee, C. Zhu, and W.G. Hurley, "State-of-Charge Determination From EMF Voltage Estimation: Using Impedance, Terminal Voltage, and Current for Lead-Acid and Lithium-Ion Batteries," *IEEE Transaction on Industrial Electronics*, vol. 54, no. 5, pp. 2550-2557, 2007.

[43] J. Lee, O. Nam, and B.H. Cho, "Li-ion battery SOC estimation method based on the

reduced order extended Kalman filtering," *Journal of Power Sources,* vol. 174, pp. 9–15, 2007.

[44] A. A. Pesaran, T. Markel, H. S. Tataria, and D. Howell, "Battery Requirements for Plug-In Hybrid Electric Vehicles – Analysis and Rationale," *23rd International Electric Vehicle Symposium*, Anaheim, California, USA, December 2-5, 2007.

[45] V. Pop, H. J. Bergveld, D. Danilov, P. P. H. Notten, and P. P. L. Regtien, "Adaptive State-of-Charge Indication System for Li-ion Battery-Powered Devices," *The World Electric Vehicle Association Journal,* vol. 1, pp. 38-45, 2007.

[46] V. Pop, H. J. Bergveld, P. P. L. Regtien, J. H. G. Op het Veld, D. Danilov, and P. H. L. Notten, "Battery Aging and Its Influence on the Electromotive Force," *Journal of The Electrochemical Society,* vol. 154, no. 8, pp. A774-A750, 2007.

[47] K. A. Smith, C. D. Rahn, and C.-Y. Wang, "Control oriented 1D electrochemical model of lithium-ion battery," *Energy Conversion and Management*, vol. 48, pp. 2565-2578, 2007.

[48] A. Vasebi, M. Partovibakhsh, S. M. T. Bathaee, "A novel combined battery model for state-of-charge estimation in lead-acid batteries based on extended Kalman filter for hybrid electric vehicle applications," *Journal of Power Sources*, vol. 174, pp.30-40, 2007.

[49] O. Barbarisi, F. Vasca, and L. Glielmo, "State of charge Kalman filter estimator for automotive batteries," *Control Engineering Practice*, vol. 14, pp. 267-275, 2006.

[50] H. Dai, Z. Sun, and X. Wei, "Online SOC Estimation of High-power Lithium-ion Batteries Used on HEVs," *IEEE International Conference on Vehicular Electronics and Safety,* pp. 342-347, December 13-15, 2006.

[51] I.-S. Kim, "The novel state of charge estimation method for lithium battery using sliding mode observer," *Journal of Power Sources,* vol. 163, pp. 584–590, 2006.

[52] G. L. Plett, "Sigma-point Kalman filtering for battery management systems of LiPB-based HEV battery packs. Part 1: Introduction and state estimation," *Journal of Power Sources*, vol. 161, pp. 1356-1368, 2006.

[53] G. L. Plett, "Sigma-point Kalman filtering for battery management systems of LiPB-based HEV battery packs. Part 2: Simultaneous state and parameter estimation," *Journal of Power Sources*, vol. 161, pp. 1369-1384, 2006.

[54] V. Pop, H. J. Bergveld, J. H. G. Op het Veld, P. P. L. Regtein, D. Danilov, and P. H. L. Notten, "Modeling Battery Behavior for Accurate State-of-Charge Indication," *Journal of The Electrochemical Society,* vol. 153, no. 11, pp. A2013-A2022, 2006.

[55] P. Rong and M. Pedram, "An Analytical Model for Predicting the Remaining Battery Capacity of Lithium-Ion Batteries," *IEEE Transaction on Very Large Scale Integration (VLSI) Systems*, vol. 14, no. 5, pp. 441-451, 2006.

[56] S. Santhanagopalan, Q. Z. Guo, P. Ramadass, and R. E. White, "Review of models for predicting the cycling performance of lithium-ion batteries," *Journal of Power Sources*, vol. 156, pp. 620-628, 2006.

[57] S. Santhanagopalan and R. E. White, "Online estimation of the state of charge of a lithium-ion cell," *Journal of Power Sources*, vol. 161, pp. 1346-1355, 2006.

[58] K. A. Smith, "Electrochemical Modeling, Estimation and Control of Lithium-ion Batteries," The Pennsylvania State University, Thesis, 2006.

[59] V. Pop, H.J. Bergveld, P.H.L. Notten, and P.P.L. Regtien, "State-of-the-art of battery state-of-charge determination," *Measurement Science and Technology*, vol. 16, no. 12,

pp. R93-R110, 2005.

[60] J. Vetter, P. Novak, M. R. Wagner, C. Veit, K.-C. Moller, J. O. Besenhard, M. Winter, M. Wohlfahrt-Mehrens, C. Vogler, and A. Hammouche, “Ageing mechanisms in lithium-ion batteries,” *Journal of Power Sources*, vol. 147, pp. 269-281, 2005.

[61] Y. Barsukov, “Challenges and Solutions in Battery Fuel Gauging,” Consultant to Texas Instruments, Inc., 2004.

[62] G. L. Plett, “Extended Kalman filtering for battery management systems of LiPB-based HEV battery packs. Part 1. Background,” *Journal of Power Sources*, vol. 134, pp. 252-261, 2004.

[63] G. L. Plett, “Extended Kalman filtering for battery management systems of LiPB-based HEV battery packs. Part 2. Modeling and identification,” *Journal of Power Sources*, vol. 134, pp. 262-276, 2004.

[64] G. L. Plett, “Extended Kalman filtering for battery management systems of LiPB-based HEV battery packs. Part 3. State and parameter estimation,” *Journal of Power Sources*, vol. 134, pp. 277-292, 2004.

[65] H. Nakamura, D. Yumoto, and Y. Ochi, “The application of adaptive digital filter for the internal state estimation of batteries,” *SICE Annual Conference*, Fukui, Japan, pp. 2239-2244, 2003.

[66] G. L. Plett, “Advances in EKF SOC Estimation for LiPB HEV Battery Packs,” Consultant to Compact Power, Inc., 2003.

[67] B. Vairamohan, “State of Charge Estimation for Batteries,” The University of Tennessee, Thesis, 2002.

[68] S. Piller, M. Perrin, and A. Jossen, “Methods for state-of-charge determination and their applications,” *Journal of Power Sources*, vol. 96, pp. 113–120, 2001.

[69] S. Rodrigues, N. Munichandraiah, and A. K. Shukla, "A review of state-of-charge indication of batteries by means of a.c. impedance measurements," *Journal of Power Sources*, vol. 87, pp. 12-20, 2000.

[70] A. J. Salkind, C. Fennie, P. Singh, T. Atwater, and D. E. Reisner, "Determination of state-of-charge and state-of-health of batteries by fuzzy logic methodology," *Journal of Power Sources*, vol. 80, pp. 293–300, 1999.

[71] “Battery State of Charge Determination,” *Electropaedia*, http://www.mpoweruk.com/soc.htm, 2005.

[72] “Kalman filter,” *Wikipedia*, http://en.wikipedia.org/wiki/Kalman_filter, 2011.

[73] “Artificial neural network,” *Wikipedia*, http://en.wikipedia.org/wiki/Artificial_neural_network, 2011.

[74] H. J. Bergveld, V. Pop, and P. H. L. Notten, “Method and Apparatus for Determination of the State-of-Charge of a Rechargeable Battery,” *U.S. Patent Application 2010/0045240*, Koninklijke Philips Electronics N.V., February 25, 2010.

[75] K. Inoue, Y. Ohnuma, and Y. Fujita, “Battery Capacity Controller,” *U.S. Patent Application 2010/0052618*, Honda Motor Co., Ltd., March 4, 2010.

[76] U. Kamishima and S. Nakazawa, “Battery Remaining Capacity Detecting Apparatus and Battery Remaining Capacity Detecting Method,” *U.S. Patent 7688032*, Nissan Motor Co., Ltd., March 30, 2010.

[77] D. Y. Kim and D. Y. Jung, “Method of Estimating State of Charge of Battery,” *U.S. Patent 7679327*, LG Chem, Ltd., March 16, 2010.

[78] J. Lin, X. Tang, B. J. Koch, D. R. Frisch, and M. J. Gielniak, “Dynamically Adaptive

Method for Determining the State of Charge of a Battery," *U.S. Patent 7768233*, GM Global Technology Operations, Inc., August 3, 2010.

[79] W. Liu, M. J. Gielniak, J. Lin, B. J. Koch, D. R. Frisch, and J. M. Lograsso, "Method and System for Determining a State of Charge of a Battery," *U.S. Patent Application 2010/0076704*, GM Global Technology Operations, Inc., March 25, 2010.

[80] G. P. Meisner, J. F. Herbst, and M. W. Verbrugge, "System and Method to Determine the State of Charge of a Battery using Magnetostriction to Detect Magnetic Response of Battery Material," *U.S. Patent Application 2010/0079145*, GM Global Technology Operations, Inc., April 1, 2010.

[81] R. Mingant, S. Martinet, and C. Lefrou, "Method for Determining the State of Charge of a Battery in Charging or Discharging Phase at Constant Current," *U.S. Patent Application 2010/0007309*, Commissariat a L'Energie Atomique, January 14, 2010.

[82] Y. Nishi, T. Takemoto, N. Haga, and T. Fuchimoto, "Device Estimating a State of a Secondary Battery," *U.S. Patent Application 2010/0085057*, April 8, 2010.

[83] R. Oki, "Electric-Powered Vehicle, Method for Estimating State of Charge, and Computer-Readable Storage Medium Having Program Stored Therein for Causing Computer to Execute Method for Estimating State of Charge," *U.S. Patent Application 2010/0045239*, Toyota Jidosha Kabushiki Kaisha, February 25, 2010.

[84] A. Paryani, S. I. Kohn, B. Boggs, A. D. Baglino, and C. B. Carison, "Battery Capacity Estimating Method and Apparatus," *U.S. Patent Application 2010/0138178*, Tesla Motors, Inc., June 3, 2010.

[85] G. L. Plett, "System and Method for Estimating a State Vector Associated with a Battery," *U.S. Patent 7800275*, LG Chem, Ltd., September 21, 2010.

[86] S. K. Sahu and A. Firouzi, "Method and Apparatus for Determining State of Charge of a Battery," *U.S. Patent Application 2010/0090651*, Deeya Energy Technologies, Inc., April 15, 2010.

[87] N. Sato, "Apparatus for Estimating State of Charge of Secondary Battery," *U.S. Patent 7804277*, Panasonic EV Energy Co., Ltd., September 28, 2010.

[88] S.-W. Seo, S.-S. Choi, Y.-J. Lee, Y.-J. Tae, H.-S. Yun, G.-J. Lim, and B.-G. Kim, "Battery Management System and Driving Method Thereof," *U.S. Patent 7684941*, Samsung SDI Co., Ltd., March 23, 2010.

[89] T. Hirata, T. Yamanaka, and Y. Nakada, "Battery State of Charge Detection," *U.S. Patent 7586290*, Nissan Motor Co., Ltd., September 8, 2009.

[90] B. J. Koch, R. S. Conell, M. W. Verbrugge, and G. P. Meisner, "Method and System for Determining a State of Charge of a Battery," *U.S. Patent Application 2009/0140742*, GM Global Technology Operations, Inc., June 4, 2009.

[91] R. J. Melichar, "Battery State of Charge Voltage Hysteresis Estimator," *U.S. Patent 7570024*, Cobasys, LLC, August 4, 2009.

[92] Y. Murakami and M. Yamabe, "Method and Apparatus for Estimating the Charge/Discharge Electricity Amount of Secondary Batteries," *U.S. Patent Application 2009/0261836*, Panasonic EV Energy Co., Ltd., October 22, 2009.

[93] K. Nukui, "Method for Detecting of Battery Condition," *U.S. Patent Application 2009/0256524*, The Furukawa Electric Co., Ltd., October 15, 2009.

[94] H. Ashizawa, H. Nakamura, and H. Asai, "State-of-Charge Estimating Device of Secondary Battery," *U.S. Patent 7352156*, Nissan Motor Co., Ltd., April 1, 2008.

[95] R. J. Melichar, "State of Charge Tracking System for Battery Systems Based on

Relaxation Voltage," *U.S. Patent 7453238*, Cobasys, LLC, November 18, 2008.

[96] Y. Murakami, N. Yamabe, K. Minamiura, and T. Kimura, "Method and Apparatus for Estimating State of Charge of Secondary Battery," *U.S. Patent 7355411*, Panasonic EV Energy Co., Ltd., April 8, 2008.

[97] J. Patino, "Method and System for Battery State of Charge Estimation," *U.S. Patent Application 2006/0022677*, Motorola, Inc., February 2, 2006.

[98] E. Schoch, "Methods for Determining the Charge State and/or the Power Capacity of Charge Store," *U.S. Patent 6876175*, Robert Bosch GmBH, April 5, 2005.

[99] P. D. Zimmerman, D. E. Zimmerman, and G. L. Claypoole, "Apparatus and method for testing remaining capacity of a battery," *U.S. Patent 6823274*, ZTS, Inc., November 23, 2004.

[100] G. L. Plett, "Method and Apparatus for a Battery State of Charge Estimator," *U.S. Patent 6534954*, Compact Power, Inc., March 18, 2003.

[101] E. D. Tate, Jr., M. W. Verbrugge, and S. D. Sarbacker, "State of Charge Prediction Method and Apparatus for a Battery," *U.S. Patent 6441586*, General Motors Corporation, August 27, 2002.

[102] M. W. Verbrugge, E. D. Tate, Jr., S. D. Sarbacker, and B. J. Koch, "Quasi-Adaptive Method for Determining a Battery's State of Charge," *U.S. Patent 6359419*, General Motors Corporation, March 19, 2002.

[103] A. Blessing and H.-P. Schoner, "Process for Monitoring the Residual Charge and Capacity of a Battery," *U.S. Patent 6329823*, DaimlerChrysler AG, December 11, 2001.

[104] W. Y. Kwok, "Method of Calculating Dynamic State-of-Charge Within a Battery," *U.S. Patent 6300763*, Delphi Technologies, Inc., October 9, 2001.

[105] N. Watanabe, Y. Kuroda, and Y. Kikuchi, "Means for Estimating Charged State of Battery and Method for Estimating Degraded State of Battery," *U.S. Patent 6300763*, Toyota Jidosha Kabushiki Kaisha, September 4, 2001.

[106] D. J. Bardsley, Jr. and J. Song, "Battery State of Charge Sensing System," *U.S. Patent 6329823*, Ford Global Technologies, Inc., June 2, 1998.

[107] T. Kawai, M. Uchida, and D. Makino, "Method for Detecting Remaining Battery Capacity by Continuously Monitoring Current, Voltage, and Temperature," *U.S. Patent 5650712*, Nippon Soken, Inc., July 22, 1997.

[108] K. Matsuda, "Battery Capacity Estimating System and Method," *U.S. Patent 5404106*, Fuji Jukogyo Kabushiki Kaishi, April 4, 1995.

[109] J. C. Lambert, "Battery State of Charge Indicator," *U.S. Patent 5119011*, General Electric Company, June 2, 1992.

[110] U.S. Department of Energy Vehicle Technologies Program, "Battery Test Manual for Plug-In Hybrid Electric Vehicles," Idaho National Laboratory, Revision 1, September 2010.

Appendix 1: Tree Diagram of SOC Estimation Methods and Principle Authors

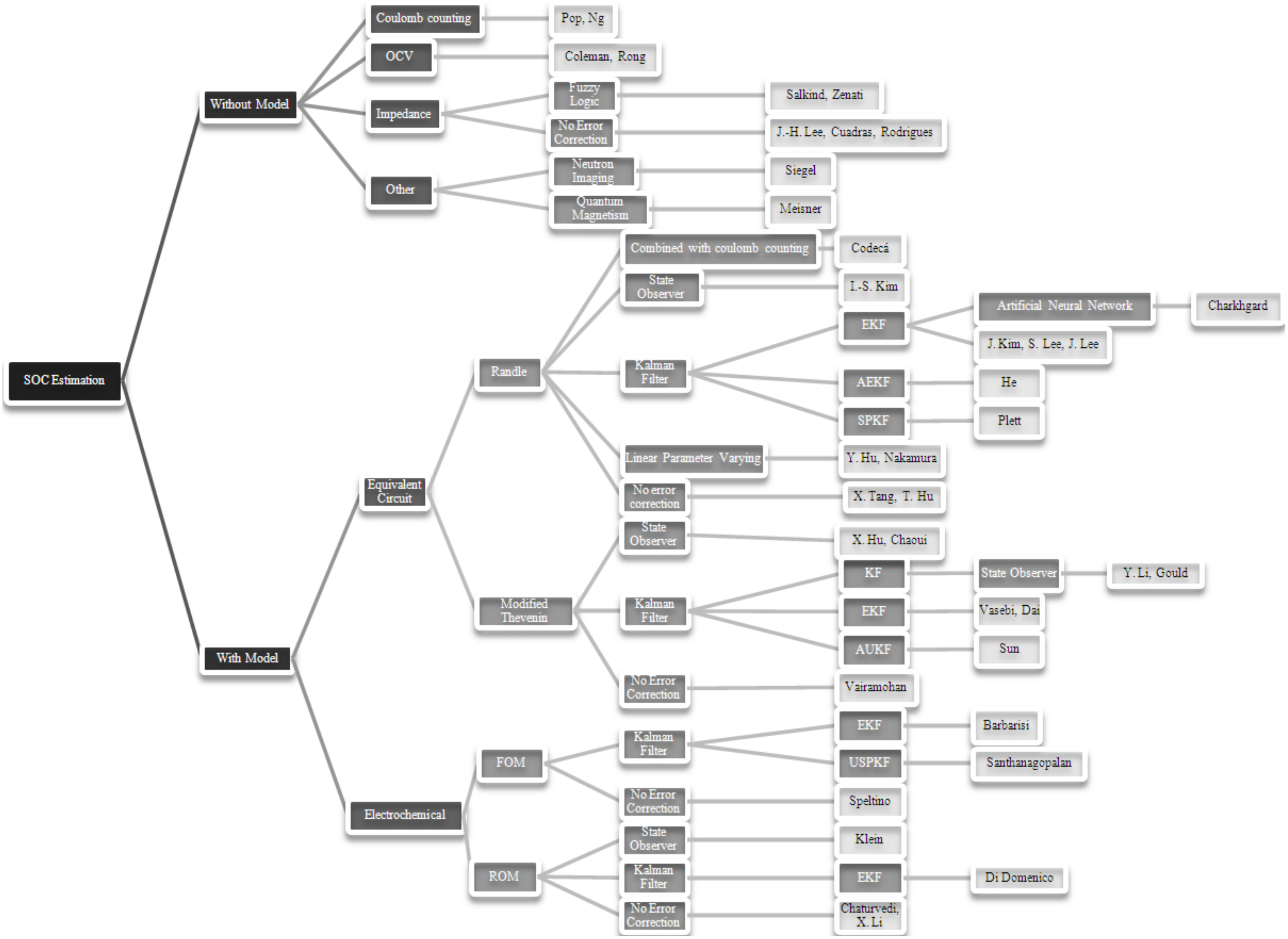

Appendix 2: Electrochemical Model Parameters

	Parameter	**Negative electrode**	**Separator**	**Positive electrode**	**unit**
Design specifications (geometry and volume fractions)	Thickness, δ	$50*10^{-4}$	$25.4*10^{-4}$	$36.4*10^{-4}$	cm
	Particle radius, R_s	$1*10^{-4}$		$1*10^{-4}$	cm
	Active material volume fraction, ε_s	0.58		0.5	
	Polymer phase volume fraction, ε_p	0.048	0.5	0.11	
	Conductive filler volume fraction, ε_f	0.04		0.06	
	Porosity, ε_e	0.332	0.5	0.33	
Solid and electrolyte phase Li^+ concentration	Maximum solid phase concentration, $c_{s,\ max}$	$35.4*10^{-3}$		$52.6*10^{-3}$	$mol{\cdot}cm^{-3}$
	Stoichiometry at 0% SOC: x_0%, y_0%	0.1279		0.9878	
	Stoichiometry at 100% SOC: x_{100}%, y_{100}%	0.7512		0.3181	
	Average electrolyte concentration, c_e	$1.2*10^{-3}$	$1.2*10^{-3}$	$1.2*10^{-3}$	$mol{\cdot}cm^{-3}$
Kinetic and transport properties	Exchange current density coefficient, k_{i0}	12.9		6.28	$A{\cdot}cm^{-2}$
	Charge-transfer coefficient, α_a, α_c	0.5, 0.5		0.5, 0.5	
	Solid phase Li diffusion coefficient, D_s	$2.0*10^{-12}$		$3.7*10^{-12}$	$cm^2{\cdot}s^{-1}$
	Solid phase conductivity, σ	1		0.1	$S{\cdot}cm^{-1}$
	Electrolyte phase Li+ diffusion coefficient, D_e	$2.6*10^{-6}$	$2.6*10^{-6}$	$2.6*10^{-6}$	$cm^2{\cdot}s^{-1}$
	Bruggeman's porosity exponent, p	1.5	1.5	1.5	
	Electrolyte phase ionic conductivity, κ	$15.8c_e \exp(-13472c_e^{1.4})$		$15.8c_e \exp(-13472c_e^{1.4})$	$S{\cdot}cm^{-1}$
	Li+ transference number, t_+^0	0.363	0.363	0.363	

Appendix 3: Experimental Test Matrix

Test Number	Temperature (°C)	Current (C-rate)	Mode	Duration
1	0	1	constant	1 discharge
		2		
		5		
2	25	1		
		2		
		5		
3	40	1		
		2		
		5		
4	0	1	constant	1 full cycle
		2		
		5		
5	25	1		
		2		
		5		
6	40	1		
		2		
		5		
7	0	1	HPPC	1 hour
		2		
		5		
8	25	1		
		2		
		5		
9	40	1		
		2		
		5		
10	0	1	constant	5 partial cycles
		2		
		5		
11	25	1		
		2		
		5		
12	40	1		
		2		
		5		

Appendix 4: Single Discharge Average SOC Error

Current (C-rate)	***T_{amb}* (°C)**	**Coulomb counting (%)**	**ECM (%)**	**ROM (%)**	**ROM with empirical correction (%)**	**ROM with feedback correction (%)**
1	0	2.22	4.63	3.19	< 0.01	3.09
	25	0.85	4.02	1.11	< 0.01	1.74
	40	3.82	1.37	3.59	< 0.01	1.72
2	0	1.87	4.79	3.35	< 0.01	2.89
	25	0.98	9.29	1.21	< 0.01	1.63
	40	3.98	3.85	3.73	< 0.01	2.96
5	0	2.26	37.97	1.95	< 0.01	1.84
	25	1.04	24.24	1.24	< 0.01	1.20
	40	5.15	6.95	4.86	< 0.01	3.58

Appendix 5: Single Cycle Final SOC Error

Current (C-rate)	T_{amb} **(°C)**	**Coulomb counting (%)**	**ECM (%)**	**ROM (%)**	**ROM with empirical correction (%)**	**ROM with feedback correction (%)**
1	0	-1.86	0.08	-0.34	0.02	-1.51
	25	-0.14	0.54	0.01	0.02	-0.24
	40	-0.10	0.87	0.04	-0.01	-0.13
2	0	-2.97	0.25	0.23	-0.02	-1.40
	25	-0.03	0.53	0.05	0.01	-0.26
	40	-0.16	0.77	0.04	-0.01	-0.09
5	0	-4.15	0.57	0.82	0.02	-1.28
	25	-2.31	0.66	0.11	-0.01	-0.24
	40	-1.33	0.93	-0.24	-0.03	-0.10

Appendix 6: HPPC Test Average SOC Error

Current (C-rate)	**T_{amb} (°C)**	**Coulomb counting (%)**	**ECM (%)**	**ROM (%)**	**ROM with empirical correction (%)**	**ROM with feedback correction (%)**
1	0	2.03	6.36	2.83	2.96	1.84
	25	1.01	4.42	1.03	1.00	0.52
	40	1.11	1.74	1.11	1.08	0.52
2	0	5.20	14.10	6.52	6.84	2.61
	25	3.16	10.28	3.03	2.88	2.23
	40	4.62	3.10	4.42	4.27	1.37
5	0	7.93	31.79	11.41	12.35	4.95
	25	7.57	22.41	7.12	6.39	3.47
	40	8.76	9.25	8.02	7.19	3.42

Appendix 7: 5 Cycle Final SOC Error

Current (C-rate)	T_{amb} **(°C)**	**Coulomb counting (%)**	**ECM (%)**	**ROM (%)**	**ROM with empirical correction (%)**	**ROM with feedback correction (%)**
1	0	-2.01	0.28	-2.36	1.91	-1.65
	25	-1.32	-6.71	-1.53	-2.79	-0.85
	40	-1.32	3.49	-1.45	-2.59	0.79
2	0	-0.10	-2.05	-0.35	4.38	0.33
	25	-0.25	-13.71	-0.58	-3.10	-0.70
	40	-0.24	5.91	-0.80	-3.21	1.48
5	0	-6.11	-5.07	-1.07	-7.55	-3.15
	25	0.45	-14.36	-0.09	-4.42	-0.89
	40	0.27	5.76	-0.40	-4.77	1.79